Thermo-structural analysis of a reactor pressure vessel lower head during core-melt severe accidents

Zur Erlangung des akademischen Grades
Doktor der Ingenieurwissenschaften
(Dr.-Ing.)

der Fakultät für Maschinenbau
Karlsruher Institut für Technologie (KIT)

genehmigte
Dissertation
von

M. Eng. Hiroshi Madokoro

Vorwort

Die vorliegende Dissertation entstand während meiner Tätigkeit am Institut für Kern- und Energietechnik (IKET) unter Leitung von Herrn Prof. Dr.-Ing. Thomas Schulenberg des Karlsruher Instituts für Technologie (KIT). Die Arbeit wurde von Herrn Prof. Dr.-Ing. Thomas Schulenberg betreut. Bei der Ausfertigung dieser Arbeit möchte ich von vielen Personen unterstützt, denen ich an dieser Stelle danken möchte.

Herrn Prof. Dr.-Ing. Thomas Schulenberg möchte ich besonders für die Betreuung der Promotion sowie die Übernahme des Hauptreferates danken. Bei Herrn Prof. Dr.-Ing. Xu Cheng, Leiter des Institutes für Fusionstechnologie und Reaktortechnik (IFRT) am KIT, möchte ich mich für die Übernahme des Korreferates bedanken.

Außerdem gilt mein Dank Herrn Dr.-Ing. Alexei Miassoedov, ehemaliger Leiter der Gruppe Unfallanalyse (UNA), für die organisatorische sowie wissenschaftliche Unterstützung.

Allen Kollegen des IKET, besonders Herrn Frank Kretzschmar, Herrn Martin Raquet, Herrn Viktor Klüber und Herrn Dr.-Ing. Thomas Arlt, sowie allen Beteiligten meiner Arbeit bin ich sehr dankbar für die gute und zahlreiche Unterstutzung sowie die konstruktive und angenehme Zusammenarbeit.

Besonders möchte ich an dieser Stelle auch meiner Familie, besonders meiner Frau Yuna, für die Unterstützung und die Geduld danken.

Karlsruhe, im November 2018 *Hiroshi Madokoro*

Abstract

Thermo-structural analysis of a reactor pressure vessel lower head during core-melt severe accidents

Severe accidents in nuclear power plants are very unlikely in the light of the accident measures implemented. However, they are still possible as recently happened at Fukushima Daiichi Nuclear Power Plants in 2011, which had severe consequences on the environment due to release of radioactive material from the damaged reactor pressure vessel (RPV). Through a perspective of confining radioactive material inside the RPV, in-vessel melt retention (IVR) through external reactor vessel cooling (ERVC) is regarded as a promising severe accident mitigation strategy. According to the list of severe accident research priority (SARP), the most important phenomena during in-vessel accident progression concerning the lower head are: (a) corium behavior in lower head, (b) integrity of RPV due to external vessel cooling, and (c) RPV failure mode. A deeper understanding of these severe accident phenomena and accident progression is still important. Since the costs of experiments are prohibitively high and large-scale experiments cannot be conducted iteratively, numerical tools must be developed at the same time to simulate real-scale severe accidents and to improve further severe accident management (SAM) measures.

The objective of this work is assessment and improvement of the lower head analysis models. RELAP/SCDAPSIM is a reactor analysis code widely used for severe accident analysis, which includes the COUPLE module that simulates a lower head molten pool heat transfer as well as vessel damage by creep strain. Traditionally, the most important use of the COUPLE module was to calculate the heat-up of the vessel wall so that the time at which the vessel may rupture or melt can be predicted. Recently, however, the applicability of the existing reactor analysis code to the ERVC became of high interest. Few evaluation works have been conducted so far using the molten pool experiments, despite of increase of interest. It is necessary to evaluate the code by using the data obtained in the latest experiments. In this work, the modification enabled the code to be applied to any external cooling condition and the evaluation was performed using LIVE test series conducted at Karlsruhe Institute of Technology (KIT).

The COUPLE module has limitations, as it assumes a homogeneous pool and effects of a stratified pool cannot be simulated and that only a simple damage progression model by creep strain is considered. The phase-change effective convectivity model (PECM) is one of the specified models for more detailed lower head molten pool heat transfer analysis, developed based on CFD-investigations. This model uses empirical correlations to calculate the convective heat transfer to solve the energy equation. The heat transfer of a two-layer stratified

pool is also possible. The model was implemented into OpenFOAM and further extended to include a structure analysis model, considering thermal expansion, plasticity, creep and material damage. The validation of the extended solver (PECM/S) was conducted using LIVE and FOREVER test series conducted at KIT and Royal Institute of Technology (KTH), respectively.

A limitation of the PECM/S is that it cannot calculate a complete accidental scenario by itself. Therefore, in order to utilize the strength of both RELAP/SCDAPSIM and PECM/S, coupling of these codes is performed through OpenMPI, a message passing interface. The coupled system was validated against the LIVE test series with different heating and cooling conditions. The results were compared also with the RELAP/SCDAPSIM stand-alone analysis and showed more detailed and better agreement with the experimental data. An application of the coupled system to the simulation of a severe accident scenario showed the capability of the coupling and its potential to be used in a RPV lower head analysis in core-melt severe accidents.

Kurzfassung

Thermomechanische Analyse des unteren Plenums des Reaktordruckbehälters bei schweren Störfällen mit Kernschmelze

Schwere Störfälle in Kernkraftwerke haben in Anbetracht der implementierten Sicherheitsmaßnahmen sehr geringe Eintrittswahrscheinlichkeit. Sie sind jedoch möglich, wie im Jahr 2011 am Kernkraftwerk Fukushima Daiichi eingetreten. Die Freilassung radioaktiver Stoffe vom versagten Reaktordruckbehälter (RDB) hatte dort massiv Konsequenzen auf die Umgebung. Um radioaktives Material im RDB einzuschließen, wird eine Ruckhaltung der Kernschmelze im Behalter (IVR: in-vessel melt retention) durch externe Reaktorbehälterkühlung (ERVC: external reactor vessel cooling) betrachtet als eine vielversprechende Sicherheitsmaßnahme um schwere Störfälle zu begrenzen. Gemäß der derzeitigen Forschungsprioritäten für schwere Störfälle werden folgende Phänomene im unteren Plenum des RDB als wichtig betrachtet, um den Unfallablauf zu erklären: (a) Schmelzeverhalten in unteren Plenum, (b) Integrität des RDBs durch externe Behälterkühlung, und (c) RDB Versagensmodus. Es wird weiterhin ein tieferes Verständnis dieser Phänomene und des Unfallverlaufs gefordert. Die Kosten großer Experimente sind sehr hoch. Sie sind daher nicht wiederholbar. Daher sollen numerische Analysemodelle weiterentwickelt werden, um schwere Unfälle zu analysieren und um Gegenmaßnahmen schwerer Störfälle zu verbessern.

Das Ziel dieser Arbeit ist die Bewertung und Verbesserung des Analysemodells für das untere Plenum. RELAP/SCDAPSIM ist ein Reaktorberechnungsprogramm, das weiterhin für Analysen schwerer Unfälle verwendet wird. Es beinhaltet das COUPLE-Modul, das den Wärmeübergang des Schmelzpools im unteren Plenum sowie die Kriechschädigung simuliert. Bisher war die wichtigste Anwendung dieses Moduls die Analyse der Aufheizung des Druckbehälters, so dass Versagens- sowie Schmelzzeit abgeschätzt werden können. In letzter Zeit gewinnt jedoch die Anwendbarkeit des vorliegenden Reaktorberechnungsprogramms auf die Reaktorbehälterkühlung immer größeres Interesse. Dennoch wurden bis jetzt nur wenige Evaluierungen mit Schmelzpoolexperimenten durchgeführt. Die Modifikation des Programms in dieser Arbeit auf die Anwendung auf externe Kühlung ermöglichte die Evaluierung des Codes anhand der LIVE-Experimente des KIT.

Das COUPLE-Modul ist dadurch eingeschränkt, dass ein homogener Schmelzepool angenommen wird und dass der Einfluss eines geschichteten Pools nicht erfasst werden kann. Ferner wird nur Kriechschädigung betrachtet und detaillierte mechanische Analysen sind nicht möglich. Das Phase-Change Effective Convectivity Model (PECM) ist ein Spezialmodell für detaillierten Wärmetransport im Schmelzpool, das basierend auf CFD-Untersuchungen entwickelt wurde.

Dieses Model verwendet empirische Korrelationen um den konvektiven Wärmetransport in der Energieerhaltungsgleichung abzuschätzen. Eine Simulation des Wärmetransports in einem geschichteten Pool ist ebenfalls möglich. Das Model wurde in OpenFOAM integriert und um mechanische Analysemodelle erweitert, um Wärmeausdehnung, Plastizität, Kriechen sowie Materialschädigung berücksichtigen zu können. Der erweiterte Löser (PECM/S) wurde mit LIVE und FOREVER Experimenten validiert.

Mit PECM/S ist es jedoch nicht möglich ein ganzes Unfallszenario aufzulösen. Daher wurden RELAP/SCDAPSIM und PECM/S mit OpenMPI gekoppelt, ein Message Passing Interface, um die Vorteile beider Codes zu nutzen. Das gekoppelte System wurde mit LIVE-Experimenten, die je nach Versuch verschiedenen Heiz- und Kühlungsbedingungen hatten, validiert. Die Ergebnisse wurden ferner mit RELAP/SCDAPSIM Einzelanalysen verglichen und zeigte eine detailliertere und bessere Übereinstimmung mit den Experimenten. Die Anwendung des gekoppelten Systems auf die Simulation eines schweren Störfalls zeigte die Stärken der Kopplung und lässt erwarten, dass die Kopplungsmethode bei Analysen des unteren Plenums des RDBs für schwere Störfällen mit Kernschmelze verwendet werden kann.

概要

炉心溶融過酷事故時における原子炉圧力容器下部ヘッドの熱および構造解析

原子力発電所においては、様々な事故が想定され対策が講じられているため、過酷事故に至る確率は非常に低い。しかしながら、福島第一原子力発電所において 2011 年に発生した原子炉過酷事故に見られるように、過酷事故に至る可能性は少なからず存在する。福島第一原子力発電所事故では、損傷した原子炉圧力容器（RPV: reactor pressure vessel）から放射性物質が放出されたことにより、周辺環境に甚大な被害を与えた。近年、放射性物質を RPV 内に閉じ込めておくという観点から、原子炉容器外部冷却（ERVC: external reactor vessel cooling）による溶融デブリの炉内保持（IVR: in-vessel melt retention）が過酷事故緩和方策の一つとして有効であると考えられている。過酷事故研究優先事象（SARP: severe accident research priority）によると、原子炉容器内事象における最重要項目は、（a）下部ヘッドにおける溶融コリウム挙動、（b）原子炉容器外部冷却による RPV の健全性、および（c）RPV の破壊モードである。今日においても、これらの過酷事故事象及び事故進展のさらなる理解は不可欠である。しかし、大規模な実験にかかる費用は多大であることから繰り返し行うことが難しく、また、実機を想定した過酷事故解析及び事故対策の向上のためにも、数値解析手法の開発が重要である。

本研究の目的は、下部ヘッド解析モデルの検証及び改善である。原子炉解析コード RELAP/SCDAPSIM は過酷事故解析に広く用いられており、下部ヘッド溶融プール伝熱解析・原子炉容器クリープ解析モジュール COUPLE が実装されている。従来、COUPLE は主に原子炉容器の温度上昇を計算し、原子炉容器の破損及び溶融タイミング評価に用いられてきた。近年、IVR に対する関心が高まる中、既存の原子炉解析コードの外部冷却への応用可能性の評価の重要性が増してきているが、最新の溶融プール実験を用いた COUPLE の再評価はほとんど行われていない。本研究では、様々な外部冷却条件で用いられるよう COUPLE の改良を行なった。さらに、カールスルーエ工科大学（KIT）で行われた LIVE 試験を用いて COUPLE の再評価を行なった。

COUPLE は均一溶融プールを仮定しており、溶融プールの層化の影響を解析には用いることができない。また、構造解析においてはクリープひずみによる単純な材料損傷モデルのみが考慮されている。本研究では、より詳細な溶融プール伝熱モデルとして、数値流体力学（CFD）を元に開発された PECM（phase-change effective convectivity model）を導入する。本モデルは実験式を元に対流熱伝達を計算し、エネルギー保存式を解く。層化した溶融プールの熱伝達も解析が可能である。本モデルを OpenFOAM に実装し、熱膨張、塑性、クリープ及び材料損傷を考慮した構造解析モデルを追加した。KIT の LIVE 試験および王立工科大学(KTH)における FOREVER 試験を用いて拡張したソルバー(PECM/S)の検証を行なった。

PECM/S は下部ヘッドに特化したモデルであり、単一ソルバーでは全事故進展を解析できないという制約がある。そこで、RELAP/SCDAPSIM および PECM/S の利点を最大限に生かすため、メッセージパッシングインターフェース OpenMPI を用いて連成解析を可能とした。LIVE 試験を用いて連成解析システムの検証を行なった。連成解析システムによる解析結果を RELAP/SCDAPSIM 単一解析の結果とも比較し、より詳細で正確な解析が可能であることを示した。過酷事故事象の解析を行い、炉心溶融過酷事故時における RPV 下部ヘッドの解析への応用可能性を示した。

Publication

This thesis is in part based on the following publications by the author:

1. H. Madokoro, F. Kretzschmar, A. Miassoedov, "Modelling of RPV lower head under core melt severe accident condition using OpenFOAM," in *2017 International Congress on Advances in Nuclear Power Plants (ICAPP 2017) – A New Paradigm in Nuclear Power Safety*, Fukui-Kyoto, Japan, 2017, pp. 507–513.

2. H. Madokoro, A. Miassoedov, "Assessment of the lower head molten pool analysis model in RELAP/SCDAPSIM using LIVE experiments," in *23rd International QUENCH Workshop*, Karlsruhe, Germany, 2017. [Online]. Available: https://doi.org/10.5445/IR/1000076201

3. H. Madokoro, A. Miassoedov, T. Schulenberg, "A thermal structural analysis tool for RPV lower head behavior during severe accidents with core melt," *Mechanical Engineering Letters*, vol. 4, pp. 18-00038, 2018. [Online]. Available: https://doi.org/10.1299/mel.18-00038

4. H. Madokoro, A. Miassoedov, T. Schulenberg, "Assessment of a lower head molten pool analysis module using LIVE experiment," *Nuclear Engineering and Design*, vol. 330, pp. 51–58, 2018. [Online]. Available: https://doi.org/10.1016/j.nucengdes.2018.01.036

5. H. Madokoro, A. Miassoedov, T. Schulenberg, "Coupling of a reactor analysis code and a lower head thermal analysis solver," *ASME Journal of Nuclear Engineering and Radiation Science* (accepted)

Contents

Nomenclature

Symbols

C_p	Specific heat capacity	[J/(kg·K)]
D	Damage parameter	[–]
e	Emissivity	[–]
g	Gravitational constant ($= 9.8$)	[m/s^2]
H	Height of molten pool	[m]
h	Distance from pool surface	[m]
h_c	Heat transfer coefficient	[W/(m^2·K)]
k	Thermal conductivity	[W/(m·K)]
n	Coordinate in direction normal to surface	[m]
Nu_{down}	Downward Nusselt number	[–]
$Nu_{down}(\theta)$	Local downward Nusselt number	[–]
Nu_{side}	Sideward Nusselt number	[–]
Nu_{up}	Upward Nusselt number	[–]
Pr	Prandtl number	[–]
q	Heat flux	[W/(m^2)]
Q_v	Volumetric heat generation rate	[W/m^3]
r, R	Radius	[m]
R_ν	Triaxiality factor	[–]
R_{eff}	Effective radius of molten region $\left(= \left(\frac{1.5V_{pool}}{\pi}\right)^{0.333}\right)$	[m]
Ra_e	External Rayleigh number $\left(= \frac{g\beta\Delta T H^3}{\alpha\nu}\right)$	[–]
Ra_i	Internal Rayleigh number $\left(= \frac{g\beta Q_v H^5}{\alpha\nu_{vis}k}\right)$	[–]
Ra_{local}	Local Rayleigh number $\left(= \frac{g\beta\Delta T h^3}{\alpha\nu_{vis}}\right)$	[–]
$Ra_{m,local}$	Local Rayleigh number in metal layer $\left(= \frac{g\beta\Delta T_{side} h^3}{\alpha\nu}\right)$	[–]
S_c	Source term	[W/m^3]
T	Temperature	[K]
t	Time	[s]
U	Characteristic velocity	[m/s]
V	Volume of molten pool	[m]
W	Width	[m]
z	Elevation	[m]
α	Thermal diffusivity	[m^2/s]
β	Thermal expansion coefficient	[1/K]

ε	Strain	[–]
λ	Lamé's first parameter	[Pa]
μ	Lamé's second parameter, Shear modulus	[Pa]
ν_p	Poisson's ratio	[–]
ν_{vis}	Kinematic viscosity	[m^2/s]
ρ	Density	[kg/m^3]
σ	Stress	[Pa]
σ_{sb}	Stefan-Boltzmann constant ($=5.67\times10^{-8}$)	[W/(m$^2\cdot$K^4)]
θ	Polar angle	[°]

Indices

amb	ambient
cr	creep
$down$	downward
eff	effective
eqv	equivalent
$frac$	fracture
h	hydrostatic
$local$	local
m	metal layer
pl	plastic
$pool$	pool
rad	radiation
$side$	sideward
up	upward
x, y, z	coordinate axis directions

Abbreviations

CEA	Commissariat à l'Énergie atomique et aux Énergies alternatives
INL	Idaho National Laboratory
KIT	Karlsruhe Institute of Technology
KTH	Royal Institute of Technology
OECD	Organisation for Economic Co-operation and Development
SNL	Sandia National Laboratories
UCLA	University of California, Los Angeles
UCSB	University of California, Santa Barbara
BWR	Boiling Water Reactor
CDF	Core Damage Frequency
CFD	Computer Fluid Dynamics
CFP	Conditional Failure Probability
CHF	Critical Heat Flux

CHRS   Containment Heat Removal System
ECCM   Effective Convectivity Conductivity Model
EPR   European Pressurized Water Reactor
ERVC   External Reactor Vessel Cooling
EVR   Ex-vessel Melt Retention
FCI   Fuel-Coolant Interaction
FOREVER   Failure Of Reactor Vessel Retention
HPI   High Pressure Injection
IRWST   In-containment Refuelling Water Storage Tank
IVR   In-vessel Melt Retention
LHF   Lower Head Failure
LIVE   Late In-Vessel Phase Experiments
LOCA   Loss Of Coolant Accident
LPI   Low Pressure Injection
MCCI   Molten Core-Concrete Interaction
MPI   Message Passing Interface
OLHF   OECD Lower Head Failure
PECM   Phase-change Effective Convectivity Model
PRA   Probabilistic Risk Assessment
PSA   Probabilistic Safety Assessment
PWR   Pressurized Water Reactor
RCS   Reactor Cooling System
RPV   Reactor Pressure Vessel
SAM   Severe Accident Management
SAMG   Severe Accident Management Guideline
SBLOCA   Small Break Loss Of Coolant Accident
SBO   Station Blackout
SDTP   SCDAP Development and Training Program
SG   Steam Generator
SLB   Surge Line Break
USNRC   US Nuclear Regulatory Commission

1 Introduction

1.1 Nuclear safety and severe accidents

The main objective of nuclear safety is to protect individuals, society and the environment by establishing safety systems and maintaining them in nuclear power plants for an effective defence against radio logical hazard [1]. The safety functions are implemented to achieve this fundamental objective. All safety activities, whether organizational, behavioral or equipment related, are subject to layers of overlapping provisions, so that if a failure were to occur, it would be compensated for or corrected without causing harm to individuals or the public at large. This idea of multiple levels of protection is know as defence-in-depth concept and is centered in the nuclear safety strategy. The defence-in-depth is twofold: first, accident prevention (Levels 1 – 3) and second, accident mitigation (Levels 4 and 5). It is generally structured in five levels and they are:

- Level 1: Prevention of abnormal operation and failures

- Level 2: Control of abnormal operation and detection of failures

- Level 3: Control of accidents within the design basis

- Level 4: Control of severe plant conditions, including prevention of accident progression and mitigation of the consequences of severe accidents

- Level 5: Mitigation of radiological consequences of significant releases of radioactive materials

The principle of defence-in-depth is implemented primarily by means of a series of physical barriers which would in principle never be jeopardized, and which would have to be violated in turn before harm can occur to people or the environment. The use of five successive physical barriers prevents the release of radioactive material from the facility to the environment: fuel pellet matrix, fuel cladding, boundary of primary coolant system, and containment. Within the design basis of a nuclear power plant, a number of initiating events are considered, including operating errors and equipment failures. According to the probability of its occurrence and potential consequences, an event may be classified as an anticipated operational occurrence (also called a transient) or a design basis accident (DBA). An accident occurring outside of the nuclear power plant design basis is called a beyond design basis accident (BDBA). Such an accident may or may not involve degradation of the reactor core (leading to significant core damage). An accident involving core degradation (typically with core melting) is also called a severe accident [2]. Severe accidents at nuclear power plants are very unlikely in the light of the accident management measures implemented in reactors. However, they are still possible

as happened at TMI-2 (1979), Chernobyl (1986) and Fukushima-Daiichi (2011). The latter two accidents still have significant effects on the environment for decades. Therefore, severe accidents have to be taken into account in the design and operational phase of a nuclear power plant.

Depending on the level of defence-in-depth breached, the main objectives of accident management are [3]:

- Prevention of the accident from leading to core damage

- Termination of core damage and maintaining the integrity of the reactor pressure vessel (RPV)

- Maintaining the integrity of the containment for as long as possible

- Minimizing on-site and off-site releases and their adverse consequences

Severe accident management guidelines (SAMGs) have been developed and implemented for each nuclear power plant. Although the approach of SAMGs varies in different countries, some basic guidelines are common for most of the plants. The basic severe accident management (SAM) actions include: cooling a degraded core; management of combustible gases; management of containment temperature, pressure, and integrity; and management of radioactive releases [4].

The first priority of nuclear safety is to prevent accidents in plants. However, it must be recognized that, although it is unlikely, those preventive actions may fail. In case of an accident sequence with sustained loss of core cooling, the following in-vessel phenomena might occur [3]:

1. Overheating of fuel and cladding

2. Onset of exothermic oxidation of the cladding, accompanied by production of hydrogen

3. Damage to and melting of the fuel cladding

4. Rapid increase in hydrogen production, with a possible challenge to containment integrity due to deflagration/detonation

5. Melting of the cladding, fuel and core materials and downward relocation of the corium (the mixture of fuel and core structural material)

6. Interaction of the molten corium with the residual water inside of the RPV

7. Potential steam explosions caused by a molten corium

8. Heating of the RPV by the molten corium

At the last stage, the possibility of RPV failure must be seriously considered. If attempts to arrest the accident progression at this point are not successful, vessel melt-through will occur and the ex-vessel phase of the accident will commence. In the ex-vessel phase of the accident, the integrity of the containment may be jeopardized, which leads to the release of radioactive material to the environment. In any condition, release of radioactive materials to the environment should be minimized. In order to achieve the objective, the integrity of the containment must be maintained. Under the extreme conditions of a severe accident with core melting, however, the integrity of the containment can be challenged in various ways. Specific consideration needs to be given to events and situations that can lead to early containment failure. Short-term containment failure can be caused by [4], [5], [6]:

- *Direct containment heating*
  This class of events and the associated risks can be avoided by reliable primary cooling circuit depressurization valves that are qualified for severe accident conditions. This is also prevented through unintended depressurization due to the failure of the surge line caused by the natural circulation flow of very hot steam from the core to the steam generator.

- *Hydrogen detonation*
  This risk class can be mitigated by hydrogen recombiners and/or igniters, potentially combined with design features to enhance atmospheric mixing, hydrogen dilution and inertization (e.g. by steam or nitrogen).

- *Steam explosions*
  The steam explosion risk can be prevented by avoiding the uncontrolled discharge of large amounts of melt into water.

Even if short-term containment failure could be avoided, the integrity of the containment is still under the risk of long-term containment failure:

- *Containment long term over-pressurization*
  The corium resulting from the core melt and the melting of internal structures will pour onto the reactor pit basemat. Contact between corium and concrete leads to what is called molten core-concrete interaction (MCCI). This interaction involves gradual erosion of the concrete basemat and the walls of the reactor pit, which could lead to basemat penetration, and consequent release of radioactive substances outside the containment building into the ground. Gases (H_2, CO, CO_2) resulting from reactions between corium and concrete contribute to increasing the pressure inside the containment building [7].

- *Containment bypass and leakage*
  All the beneficial effects of the containment would be negated by containment bypass. In the bypass scenario, a path is found for the fission product source term to escape from the containment without its failure. Possible paths in PWRs are: (1) the path from the containment to the auxiliary building caused by an interfacing LOCA and (2) the steam generator tube rupture providing a path to the environment through the dump valves on the secondary side of the damaged steam generator.

For the Generation III PWR designs, the above mentioned items are taken care mainly through design, construction, operation and accident management, in order to reduce their risks as low as reasonable possible. Two different strategies are considered in Generation III reactors in order to stabilize the core melt and to terminate a severe accident: ex-vessel melt retention (EVR) or in-vessel melt retention (IVR). In one of EVR strategies, melt arrest and stabilization is achieved by ex-vessel debris bed coolability, provided by a deep water pool placed under the RPV. Another EVR strategy is to collect and to cool the corium ejected from the RPV in a core catcher placed in the containment. On the other hand, a typical IVR arrests and confines the corium inside the lower head of the RPV by flooding the reactor pit (cavity). A deep water pool for melt quenching was implemented in the Swedish BWRs in 1980s [8]. More recently, a core catcher is installed in the containment of European Pressurized Water Reactor (EPR) of AREVA [9], [10] and Russian VVER plants [11]. On the other hand, an IVR system is utilized in AP1000 of Westinghouse [12] and Chinese designs of advanced PWRs.

In the following section, details of two different strategies and their challenges are discussed.

1.2 Corium retention and cooling strategy

1.2.1 Ex-vessel melt retention (EVR) strategy

Melt quenching in a deep water pool

The strategy of melt quenching in a deep water pool was implemented in the Swedish BWRs in 1980s, based on a corresponding Swedish Government decision to minimize the radiological consequences of a severe accident for Swedish Nuclear Power Plants [8]. Further safety improvements were performed extensively.

Severe accident mitigation strategy in Swedish and some Nordic BWRs includes comprehensive measures for corium melt ex-vessel retention, isolation and passive cooling [6]. It foresees gravity driven flooding of lower drywell with water from the pressure suppression pool. An illustration of a containment at the late phase of severe accident is shown in Fig. 1.1. A 7–12 m deep water pool is placed under the RPV, so that the core melt, after its release from the RPV, is expected to fragment, quench and transform into a coolable particulate debris bed. One of the advantages of the concept is that it requires only minimum additional hardware, namely adequate means and water sources for the flooding of the cavity. Flooding must be completed prior to RPV failure to a final water level below that of the RPV bottom.

The main remaining open issues are:

- *the possibility of steam explosions during melt quenching*
  Remaining uncertainties are the probability and magnitude of the energetic interaction, the mechanical loads and the strength of the containment. The steam explosion phenomenon is strongly linked with the in-vessel melt progression, the model of vessel failure and the melt release scenario.

- *the formation of a non-coolable debris bed at the bottom of the cavity*
  The debris coolability is affected by the mechanisms of jet fragmentation in water, particle quenching, settling and spreading. In addition, it is influenced by all the phenomena that affect the shape, composition, and properties of the individual particles. The size distribution and porosity of the debris bed are also important parameters.

The risk of steam explosion and debris re-melting issues are both experimentally and numarically investigated [13], [14]. The high uncertainties in the melt release and melt-water interaction characteristics can potentially reduced by dedicated measures, which enhance the fragmentation of the melt, improve the coolability of the debris bed, reduce the risk and energy of steam explosions, and mitigate their consequences. Some of the measures, however, can cause an adverse effect such that a better fragmentation may cause more favorable condition for steam explosion.
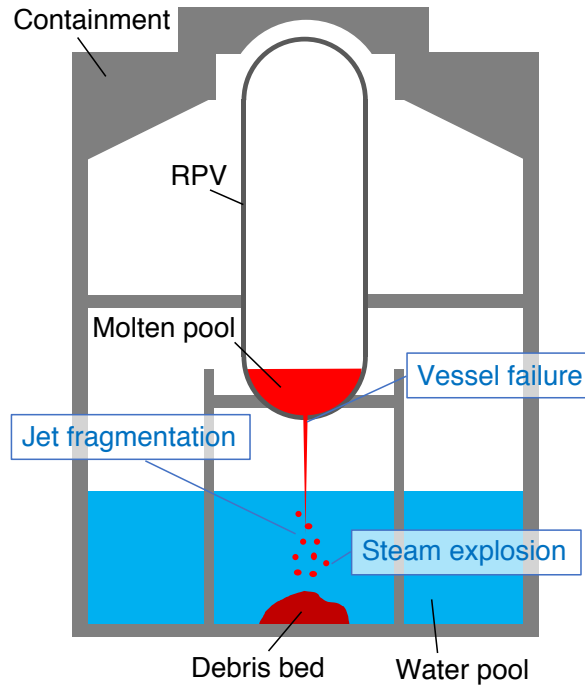
Figure 1.1: Section of a BWR containment at the late phase of severe accident (after [6] and [14])

Crucible-type core catcher

The Russian VVER-1000 and VVER-1200 locate a core catcher below the RPV, while in the EPR the core stabilization is achieved by placing a core catcher in a dedicated lateral sprea-ding compartment. In the following part, the main strategy taken in the EPR design is explained.

The "Technical Guidelines for Future Pressurized Water Reactors" released in 2000 [15] demands significant improvements at the design stage, in particular, a better consideration of the problems related to severe accidents. In order to fulfil the requirements, the EPR design introduces, beyond the evolutionary improvements, an additional fourth level of defence, namely the mitigation of consequences of severe core damage by introducing measures and layout features for severe accident mitigation and by strengthening the confinement function [16], [17].

The EPR core catcher concept is based on spreading the corium over a large surface area, with the corium reflooded and cooled by water from the in-containment refuelling water storage tank (IRWST) located in the containment building. The EVR strategy has been favored against the IVR strategy in the EPR. The following reasons were mentioned by Bittermann et al. [17]:

- the too low margins of IVR at the high power rating of the EPR, and

- the risk of a highly energetic steam explosion in case of IVR failure.

The latter results in an increase in the probability of early containment failure with related negative radiological consequences that compare unfavorably with the achievable gain from the
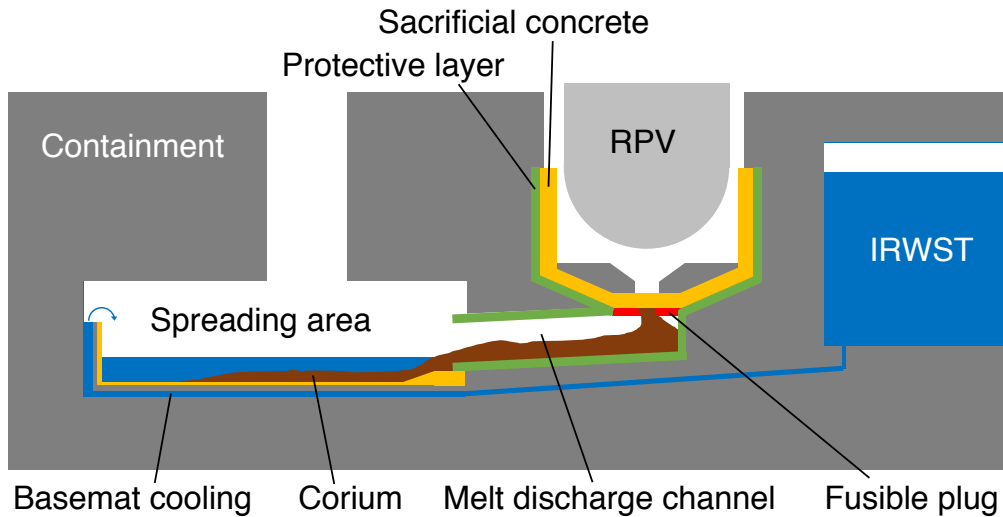
Figure 1.2: A cross-section view of the main components of the EPR core catcher (after [7])

avoidance of late basemat melt-through.

A schematic view of the main components of the EPR core catcher is shown in Fig. 1.2. To promote corium spreading, the core catcher temporarily retains the corium in the reactor pit before spreading. The corium erodes a sacrificial concrete layer, which is approximately 50 cm thick, before flowing into the melt discharge channel that connects the reactor pit to the spreading compartment. The slow destruction of the sacrificial concrete layer further provide an effective way to accumulate the melt before spreading. The connection between reactor pit and the spreading compartment is normally locked and will only be opened by the melt in case of a severe accident. This separation protects not only the core catcher from loads related to RPV failure but also the safety of the plant in case of an unintended flooding of the core catcher during operation. As the spreading compartment is a dead-end room isolated from the rest of the containment, melt spreading will take place under dry conditions. Melt arrival in the spreading compartment initiates opening the flooding valves, allowing gravity-driven overflow of water from IRWST. The containment heat removal system (CHRS) is utilized in the EPR to achieve a long-term heat removal from the containment. The CHRS takes suction from the IRWST and re-injects the cooled water into the containment: either spraying into the containment atmosphere or feeding directly to the core catcher.

Since the EPR core melt stabilization concept has successfully passed the licensing procedures in several countries, further R&D is not required for validating the concept itself. The current design basis, however, still contains significant conservatism due to less available data. If better corresponding data are available, these conservatisms can be removed and leaner solutions be adopted [6].

1.2.2 In-vessel melt retention (IVR) strategy

IVR of VVER-440 and AP600

The IVR through external reactor vessel cooling (ERVC) is based on the idea of flooding the PWR vessel cavity or the BWR dry-well with water either to submerge the vessel completely or at least to submerge the lower head [4]. An advantage of the IVR is that an additional complex and expensive core catcher is not necessary and that the construction cost can be reduced. The coolant flow through the external path removes the decay heat of the molten pool and keeps the vessel wall cool enough to prevent it from creep deformation and failure. The flow is normally designed to be driven by natural circulation. The angular local heat flux imposed by the melt pool to the vessel wall should not exceed the limit of the external cooling capacity, that is, the critical heat flux (CHF) of boiling at all points around the lower head. An illustration of IVR is shown in Fig. 1.3. In case the cooling fails, the integrity of the vessel will be lost, due to a boiling crisis and subsequent escalation of the vessel wall temperature. Since there exists the risk of steam explosion once the vessel fails and the molten core material has a direct contact with the ex-vessel cooling water, the vessel integrity and failure mode must be rigidly investigated.

The concept of IVR was firstly proposed as a backfit for the VVER-440 reactors of the Loviisa Nuclear Power Plant in Finland and was approved by the local regulatory authority [18]. The efficacy of the strategy was assessed for an AP600 design. For a uniform corium pool of the AP600 reactor, there was sufficient margin between the CHF on the water side and the incident heat flux from the corium pool. This margin of safety, however, may be reduced substantially in case there is a metal layer present on top of oxidic corium pool (Fig. 1.3). The metal layer results from the steel present in the lower heads that is melted by the corium pool. Since the steel is lighter than the corium, it rises to the top of the corium pool. The metal layer receives heat from the corium pool and performs Rayleigh-Bénard convection transferring heat transversely to the vessel wall, which is then subjected to a highly elevated heat flux. It was found out that the heat flux varied with angle, peaking near the equator of the lower head. The CHF of the external cooling also reached its highest value (1.5 MW/m^2) near the equator. In most considered cases, the ratio of the imposed heat flux to the CHF was below 0.6, and thus the major conclusion was that thermally-induced failure of an externally-cooled AP600 vessel was physically unreasonable [5], [19]. The final design of AP600 was approved in 1998 and the design certification was issued by the US Nuclear Regulatory Commission (USNRC) in 1999.

IVR of AP1000

The reactor concept was updated and the Westinghouse AP1000 nuclear power plants has been developed. Due to the higher power generation, further work was performed on the technology and methodology of IVR, particularly for the enhancement of the CHF on the outer surface of the vessel, to obtain a sufficient safety margin to cover the uncertainties. Through the ULPU experiments [20], which scaled the external cooling flow path of AP1000, it was found that
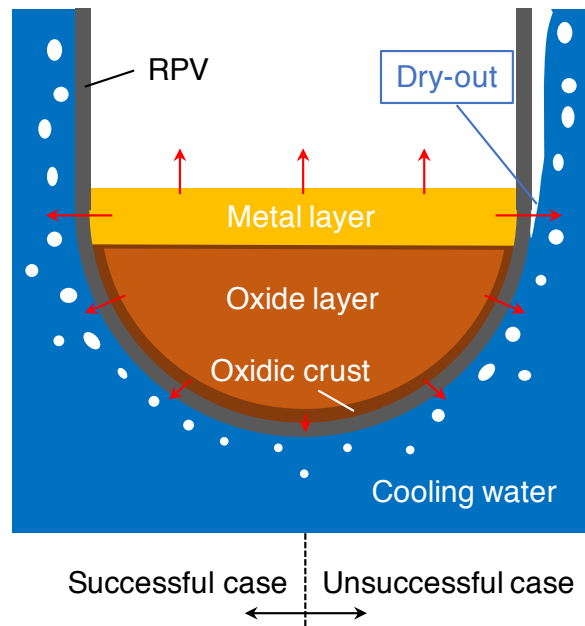
Figure 1.3: Schematic illustration of a two-layer molten pool

the CHF near the equator of the lower head could reach 2 MW/m^2, which was larger than the maximum thermal load for AP1000 estimated as 1.3 MW/m^2 [4]. One of the major observation by both Rempe et al. [21] and Theofanous et al. [22] was the focusing effect of the molten light metallic layer that could result in a large heat flux possibly exceeding CHF at the locations of the thin metallic layers. For a thin metal layer on top of the oxide pool, a portion of the decay heat in the lower oxide pool needs to be dissipated though a small surface area bounded by the metal layer. Therefore, the factors that could potentially compromise the vessel integrity in the metal layer are the amount of steel and the decay power in the lower oxide layer. Since the metal layer in AP1000 includes the entire support plate and core shroud metal mass, it is thick and does not focus the heat flux to the side wall of the reactor vessel. It was concluded that there is significant margin to failure. In the RASPLAV and MASCA projects [23], [24], different layer configurations depending on material interactions were investigated. It is postulated that mixing of molten oxide and metal may result in chemical reaction that can create a heavy bottom layer, a thinner top metal layer, and alter the heat fluxes in the oxide layer. The results showed that the reactor vessel does not fail in this debris configuration.

According to the AP1000 PRA [25], the core damage frequency (CDF) for at-power internal events (excluding seismic, fire, and flooding events) is 2.4×10^{-7} per reactor-year. It is conservatively estimated that a total of approximately 60% of the severe accident scenarios are depressurized and flooded inside and outside the reactor vessel (or 1.5×10^{-7} per reactor-year), in which all or part of the degraded core materials will be cooled and remained above the core support plate, and the focusing effect can be eliminated [26]. The frequency of accident sequences that are depressurized and cooled by water only on the outside of the reactor vessel surface is estimated to be approximately 7.5×10^{-8} per reactor-year (or 31% of the CDF). The

remaining CDF of 1.5×10^{-8} per reactor year is comprised of high pressure sequences and sequences initiated by steam generator tube rupture and anticipated transient without scram, where IVR strategy is not directly applicable.

Even if the reactor vessel were assumed to fail in an earlier phase, the AP1000 containment is able to accept relocation of molten debris to the reactor cavity without causing an early containment failure. The AP1000 PRA concluded that the overall release frequency for AP1000 is 1.95×10^{-8} per reactor-year, which is approximately 8% of the CDF. This is far below the the safety goal of 1.0×10^{-6} per reactor-year. The USNRC granted final design approval in 2004. In 2008, China has also started to build four AP1000 reactors at two sites.

In an assessment work of AP1000 [27], uncertainties associated with the initial conditions including the decay power, fraction of Zr oxidation, mass of UO_2 relocated to the lower plenum, and the amount of steel in the lower plenum debris were investigated. It was assumed that the mass of steel layer is correlated with the mass of UO_2 in the lower plenum. Remarkably, smaller amount of UO_2 (up to 60 t) can relocate to the lower plenum without submerging the lower core plate. Under this condition, the amount of steel in the upper metallic layer is very limited with a mass of 3 t and the formation of a metal layer which might be thin enough to cause significant focusing effect. At the bottom of the vessel, the heat flux was predicted to be the lowest and the ratio of the imposed heat flux to the CHF was around 0.2. Although, at the top of the molten oxide layer, the heat flux ration increased significantly, it remained below 1, which implies the conditional failure probability (CFP) was zero. In the metal layer, however, the CFP was 0.15 in the base case analysis due to the focusing effect. Significant melting of the vessel wall was predicted both in the top metallic layer region and near the top of the oxide layer. The sensitivity analysis showed that the estimated likelihood of lower head failure ranges between 4% and 30% given a low-pressure core-melt accident. The CFP in the oxide layer remained zero in the sensitivity study and varied only in the metallic layer. An assessment has been conducted on the dynamic loads resulting from the ex-vessel fuel coolant interaction (FCI), or energetic interaction of the molten core material and cavity water. It was concluded that the potential for large impulse loads on the cavity and the RPV structures, and subsequently the containment penetrations, cannot be excluded in AP1000.

IVR of higher-power reactors and open issues

For higher-power reactors, the efficiency of an in-vessel retention strategy is less robust since the power density to be removed from the vessel is higher. Although the IVR strategy was adopted by the Korean design of the 1400 MWe Advanced Power Reactor (APR1400), the severe accident management strategy is not definitively set and may undergo changes [5]. The IVR is also preferred in Chinese Generation III PWRs: CAP1400, which has the same design philosophy and features as AP1000, and HPR1000. Regarding IVR application in Chinese reactors, extensive

research efforts have been performed [28], [29]. The qualification of an IVR measure directly depends on two parameters:

- the heat flux incident from melt pool on the vessel wall, and

- the heat removal capacity of the external cooling of the vessel, or the CHF issue.

Therefore, one of recent research focuses is CHF enhancements by designing an optimal insulation structure surrounding the vessel, streamlining the flow path, and increasing the driving head. The other uncertainty relates to the molten pool formation, which depends on in-vessel accident progression and boundary conditions. A number of experiments have been conducted to understand complex physics in the core melt.

Not only experimental investigations to further understand the phenomena, but also development of numerical analysis tools, based on the knowledge obtained by the experiments, is important. Since severe accidents in a full-scale nuclear power plant cannot be performed due to the enormous cost and the risk regarding radioactive materials, a numerical analysis tool is necessary, in order to predict an entire severe accident progression. The vessel behavior in the IVR condition needs to be more in detail investigated to determine its risk and its upper limit. It was pointed out that the following factors were still poorly understood [5]:

- the coupling analysis of the melt pool convection, vessel wall heat conduction, and external boiling heat transfer,

- the vessel wall creep under high temperature and its interaction with the melt pool, and

- thermo-chemical erosion.

2 State of the Art

2.1 Previous studies

The main issue on IVR is that the heat flux from the molten pool to the external coolant must not exceed the limit of heat removal capacity, that is, the CHF of boiling all along the vessel wall. The difficulty of the IVR is to determine precisely the CHF and the heat flux of the molten pool convection that is highly affected by the accident scenario and molten pool natural circulation condition. Therefore, most of the experimental programs associated with IVR phenomenon in the past decades focused on the research of melt thermal hydraulics, although our knowledge-base regarding the IVR issue can be divided into six categories: decay heat and fission products, melt thermal hydraulics, heat flux removal, melt composition and chemistry, vessel failure modes, and corresponding transient processes [30]. To investigate the thermal hydraulic phenomena in corium pools accumulated in the lower head after melt relocation, a considerable number of experiments and analyses have been carried out in facilities with different geometries, such as fluid layer and rectangular cavities, elliptical and semicircular slice pools, and hemispherical pools. The results of these experiments have been applied to develop and validate models that can be implemented into severe accident analysis codes.

Another issue concerning the phenomena during late in-vessel accident progression is the RPV vessel failure mode and the following corium release from the failed vessel. The lower head of the RPV can be subject to significant thermal and pressure loads in an IVR scenario. The vessel integrity will be threatened not only by heat flux from the molten pool exceeding the CHF of the cooling water but also from reduction of vessel wall thickness due to the thermal and mechanical loads. The mechanical behavior of the reactor vessel lower head is of importance both in the assessment of severe accident progressions and the assessment of accident mitigation strategies. According to Humphries et al. [31], for severe accident assessment, the failure of the lower head defines the initial conditions for all ex-vessel events, and in accident mitigation the knowledge of mechanical behavior of the reactor vessel defines the possible operational envelope. Klein-Heßling et al. [32] has reported that, through a number of experiments on vessel deformation and failure in high temperature, the information on the break location is regarded as sufficient for PWR but not for BWRs with a large number of bottom head penetrations. In none of the past experiments, the interactions of gradually re-melting debris, containing high and low melting temperature materials, with vessel penetrations were considered. Thus, the priority of this research area remains in a high priority. There is a need to investigate the issue of RPV penetration failure in order to provide necessary data for resolving ex-vessel severe accident progression phenomena and issues.

2.1.1 Experimental investigation

In the following part, detailed information of some important experimental programs will be summarized and compared in Table 2.1, where Ra_i is internal Rayleigh number and Pr is Prandtl number.

COPO I

The COPO I experimental facility is a two-dimensional 1:2 scaled elliptical slice, geometrically similar in shape to the lower head of the Loviisa power plant (VVER-440 reactor). The tests were carried out by Kymäläinen et al. [33] at Fortum Nuclear Services in Finland and CEA/DRN (Grenoble) in France. The simulant material of H_2O–$ZnSO_4$ solution is heated uniformly by volumetric Joule heating, i.e. the electrical resistance of the fluid causes its heat up when a current flows through it, which is convenient for achieving large characteristic length scales and thus large Rayleigh numbers (10^{14}–10^{16}). The measured heat flux distributions at the isothermal boundaries show that the downward heat flux strongly depends on the position along the curved wall. The heat flux at the vertical portion of the side wall, however, is essentially uniform and predicted well by Steinberner-Reineke correlation [34], while the upward heat transfer is 30% underestimated by the correlation beyond a Rayleigh number of 10^{15}.

COPO II

Helle et al. [35] has reported the results of the COPO II experiments. Two geometrically different versions of the COPO II facility were constructed: COPO II-Lo having the shape of the RPV lower head of VVER-440 reactor (torispherical bottom) and COPO II-AP with a semicircular shape modeling the RPV bottom of an AP600 PWR. A distinctive feature in the COPO II facilities is the cooling arrangement in which liquid nitrogen is circulated on the backside of the aluminium walls of the pool. Thus an ice crust forms at the inner walls to provide ideally an isothermal boundary and the temperature difference in the pool can be sufficiently large to allow investigations of possible effects resulting from temperature dependent fluid properties. It was shown in experiments with a crust at the top of the pool that the Nusselt number was remarkably higher (20–30%) than in experiments with an ice-free upper boundary. The effect of stratified pool was also investigated by using H_2O–$ZnSO_4$ solution at the bottom as a heat generating layer and distilled water on top of it as non-heat generating layer. The measured average upward and sideward Nusselt numbers from the distilled water layer are well predicted by the Globe and Dropkin correlation [36] and Churchill and Chu correlation [37], respectively.

BALI

The BALI facility was designed to investigate the natural convective heat transfer of the corium pool for in-vessel and ex-vessel cooled situation for the prototypic French PWRs, having a two-dimensional 1:1 scaled 1/4 circular slicing geometry. The tests were performed by Bernaz et al. [38] at CEA in France. The water was used as the simulant material and heated electrically by Joule effect with current supplies located on the sides. The curved and upper walls were

cooled from outside by organic liquid with the temperature range of -80 °C and 0 °C, thus ice crust is formed at the pool boundary to provide a constant temperature boundary condition. The tests with top cooling demonstrated that the height of upper layer occupies about 40% of total height and the heat flux was quite uniform over the top 60% height. A good agreement is observed between COPO II and BALI results for the average upper heat transfer. The average downward heat transfer correlation from BALI results can be applicable within a wide range of internal Rayleigh numbers between 10^{12} and 10^{17}. In addition, cellulose compound and solid glass balls were added in the contrast experiments to investigate the effect of viscosity and porosity, respectively.

SIMECO

The SIMECO experiments were performed at Royal Institute of Technology (KTH) in Sweden to investigate more in detail the heat transfer of a layer-stratified pool and the results of the experiments are reported by Sehgal et al. [39]. The facility consists of a 1:8 scaled two-dimensional slice of a prototypic PWR. A cable type heater is used to provide internal heating of the pool. The brass wall modeling the RPV wall is externally cooled by a controlled water loop and a heat exchanger on the top of the vessel with regulated water loop enables measurement of the upward heat transfer. The two-layer experiments were performed with a liquid mixture of Benzyl benzoate and Parafin oil. In the three-layer experiments, Parafin oil, water and chlorbenzene were used to investigate stratification of three immiscible fluids.

RASPLAV

The RASPLAV experiments were conducted at the Kurchatov Institute in Russia and its findings are summarized by Asmolov [23]. These experiments covered investigations in several facilities with prototypic materials (UO_2–ZrO_2–Zr mixture) and with salt (NaF–$NaBF_4$ mixtures) in a wide temperature range. The experiments were conducted under non-isothermal boundary conditions on the outer cooled wall with side wall heating method. For the contrast experiments investigating the impact of different heating techniques, a direct electric heating method was employed. The experiments with a 25%NaF–75%$NaBF_4$ non-eutectic composition, which is characterised by a wide temperature range between solidus and liquidus, show that thermal characteristics in the temperature region above liquidus temperature do not differ from those which were obtained with a 8%NaF–92%$NaBF_4$ eutectic melt composition in the second series of salt experiments. However, a difference is observed in the temperature distribution in the temperature region between solidus and liquidus temperature. The local heat flux distribution is rather similar to that obtained for regimes with and without crust but differs from both ones.

COPRA

The COPRA experiments have been performed at Xi'an Jiaotong University in China. The facility consists of a two-dimensional 1/4 circular slice to investigate the in-vessel molten corium pool behavior for the in-vessel corium retention during severe accidents in Chinese large-scale advanced PWRs in 1:1 scale [40]. For the simulant material, a non-eutectic binary mixture of

80mol% KNO_3–20mol% $NaNO_3$ composition is used. The volumetric heating system of electrical heating rods was designed to simulate the homogeneous decay heat. For the top boundary, the insulation lid and the cooling lid were designed to simulate the insulation condition and the top cooling condition, respectively. The curved vessel wall was enclosed from outside with the cooling path to keep the boundary temperature nearly isothermal. In the experiment, the internal Rayleigh numbers could reach to 1.188×10^{15}–1.784×10^{16}. The experimental results show that more times of heating power transition may facilitate crust cracking and create thicker crust. The comparison with previous experiments showed that the downward Nusselt number from COPRA experiments were lower than those from ACOPO and BALI predictions.

mini-ACOPO and ACOPO

The ACOPO experimental program was conducted by Theofanous et al. [41] at University of California, Santa Barbara (UCSB), aiming to simulate natural convection heat transfer from volumetrically heated hemispherical pools at high Rayleigh numbers. The mini-ACOPO facility has a smaller size of the vessel in scale of 1:8 [42], while the ACOPO facility has a hemispherical vessel in scale of 1:2 to the lower head of AP600. A distinctive feature of the ACOPO and mini-ACOPO experiments is that no internal heat source was installed. The simulant material is preheated to high initial temperature and then poured into the vessel. The idea behind this approach is to simulate volumetric heating, by suddenly cooling the boundaries and interpreting the transient system cool-down as a sequence of quasi-stationary natural convection states. A total heat loss rate can be obtained to define the instantaneous internal Rayleigh numbers, which are correlated then to the instantaneous Nusselt numbers. Although a completely different temperature and velocity field might be obtained compared to the case with internal heat sources, the ACOPO facility further confirms this experimental concept and extended the obtained results to fully cover the prototypic range of internal Rayleigh numbers of current interest concerning IVR.

UCLA

At University of California, Los Angeles (UCLA), Asfia and Dhir [43] performed a series of experiments to investigate natural circulation heat transfer in a hemispherical pool with internal heat generation. Some special experimental methods were applied in this project: Freon-113 contained in a Pyrex bell jar, was used as a test liquid and the pool was heated uniformly with a magnetron controlled by a conventional microwave oven. The insulated wall was installed for the top surface, while the external vessel was cooled by water. From the comparisons with results from pools with free surface, it's shown that different top boundary conditions make only a slight difference in heat transfer coefficients.

LIVE

In the LIVE facility at Karlsruhe Institute of Technology (KIT) in Germany, the late in-vessel phase of a postulated severe accident in a nuclear power plant is investigated by Gaus-Liu et al. [44]. The facility consists of three main parts: the test vessel including cooling system, the volumetric

Table 2.1: Summary of experimental studies in respect of IVR [46], [47]

Experiments	Geometry	Scale	Heating	Simulant	Ra_i	Pr	Boundary	Investigation emphasis
COPO I	Semi-elliptical slice	1:2 (VVER-440)	Joule heating	H_2O–$ZnSO_4$ solution	10^{14}–10^{16}	~3	Isothermal top and bottom walls	Natural convection
COPO II	Semi-elliptical slice Semicircular slice	1:2 (VVER-440 and AP600)	Joule heating	H_2O–$ZnSO_4$ solution Distilled water	10^{14}–10^{16}	~3	Isothermal top and bottom walls	Natural convection Crust formation Layer stratification
BALI	1/4 Circular slice	1:1 (French PWR)	Joule heating	Salted water	10^{13}–10^{17}	~7	Isothermal top and bottom walls	Effect of viscosity and porosity Focusing effect of the top metal layer
SIMECO	Semicircular slice	1:8 (AP600)	Cable-type heaters	$NaNO_3$–KNO_3 Paraffin-water-chlorobenzene	9.6×10^{12} –9.5×10^{13}	–	Isothermal top and bottom walls	Effect of two-layer and three-layer stratification
RASPLAV	Semicircular slice	1:10	Side wall heating Joule heating	UO_2–ZrO_2-Zr Naf-$NaBF_4$	4.7×10^{11} –1.61×10^{13}	4.56–7.74	Insulated top wall and cooled bottom wall	Prototypical material study Layer stratification Non-eutectic mushy zone
COPRA	1/4 Circular slice	1:1 (Chinese PWR)	Cable-type heating rods	$NaNO_3$–KNO_3	1.188×10^{15} –1.784×10^{16}	–	Insulated top wall and isothermal bottom wall	Natural convection
mini-ACOPO	Hemisphere	1:8 (AP600)	No heating	Feron-113 Water	10^{11}–7×10^{14}	7–11	Isothermal top and bottom walls	Natural convection
ACOPO	Hemisphere	1:2 (AP600)	No heating	Water	10^{12}–2×10^{16}	~7	Isothermal top and bottom walls	Extension of mini-ACOPO
UCLA	Hemisphere	1:10	Magnetron	Feron-113 Water	2×10^{10} –1.1×10^{14}	8.2–9.5	Isothermal or insulated top wall Isothermal bottom wall	Natural convection
LIVE	Hemisphere	1:5 (German PWR)	Cable-type coil heaters	$NaNO_3$–KNO_3	2×10^{13} –8×10^{13}	8.1–10.4	Insulated/isothermal top wall Isothermal bottom wall	Crust formation Different boundary conditions
FOREVER	Hemisphere	1:5	Cable-type heaters	CaO–B_2O_3	–	–	Isothermal top and bottom walls	Creep deformation Vessel failure mode
LHF/OLHF	Hemisphere	1:4.85	Radiant heater	–	–	–	–	Creep deformation Vessel failure mode

heating system and a separate heating furnace [45]. In Figure 2.1, a schematic drawing of the LIVE test facility is shown. The LIVE test vessel is a 1:5 scaled semi-spherical lower head of a typical PWR and is fabricated from stainless steel. The inner diameter of the test vessel is 1 m and the wall thickness is approximately 25 mm. To investigate the influence of different external cooling conditions on the melt pool behavior, the test vessel is enclosed by a second vessel (cooling vessel) to cool the test vessel from the outside. The cooling water inlet is located at the bottom of the cooling vessel and the outlet is positioned at the top of the vessel. A volumetric heating system with heating wires is installed to simulate the decay heat released from the corium melt. The heating wires were installed and controlled in such a manner that the heat was generated in the melt as homogeneously as possible. The melt is produced in the external heating furnace and it is poured into the test vessel by tilting the furnace. According to purposes of each test, different external cooling conditions, melt volumes and heat generation rates can be used. Up to now, two types of simulant materials were used: non-eutectic composition (80mol% KNO_3–20mol% $NaNO_3$) and eutectic composition (50mol% KNO_3–50mol% $NaNO_3$). Main focuses of the tests are heat flux distribution through vessel wall, melt pool temperature and crust thickness. In this study, three tests using non-eutectic simulant materials, LIVE-L1, -L7V and -L11, are analyzed, which have different melt surface cooling conditions; in LIVE-L1, the insulation lid is installed above the melt surface, while, in LIVE-L7V, the melt surface is cooled by water using the cooling lid. Although a number of experiments have been conducted using the insulation lid, a few tests including LIVE-L1 applied air-cooling transient at the beginning of the test. In order to evaluate the COUPLE module under different external cooling conditions, LIVE-L1 test was selected in this study. On the other hand, LIVE-L7V is the only test with non-eutectic melt where both the top cooling and external cooling have been applied. In both experiments, the internal Rayleigh number was $\sim 10^{13}$. The test conditions are summarized in Table 2.2 and the material properties of non-eutectic melt used in the analyses are given in Table 2.3.

LIVE-L1 After completion of the pouring process with 120 liters of simulant material with temperature of approximately 620 K, a total heating power of approximately 18 kW was applied to homogeneously heat the melt. The insulation lid was installed at the top of the vessel and the initial external cooling was conducted by air. To avoid overheating of the melt, the power was stepwise reduced to $\sim$10 kW within 3720 s and was kept at this level. Flooding of the vessel external wall was started at 7220 s initially with 1.5 kg/s to fill up the gap between the cooling vessel and the test vessel wall and then with $\sim$42 g/s. The measured temperature of the cooling water at the inlet was about 281 K and the temperature of the cooling water outflow increased to about 353 K at the beginning and decreased to about 343 K after about 25000 s. The homogeneous heating of the melt with 10 kW was continued about 72000 s to reach the steady state condition. Afterwards the heating power was reduced to 7 kW to observe the influence of the power reduction on the crust growth and heat flux distribution. This power level was kept for another 22000 s.

LIVE-L6 The objective of LIVE-L6 test was to investigate the behavior of two-layer melt pool scenario, which includes the heat generating lower layer and the unheated upper layer

of molten material. A total of 210-liter simulant material was poured into the test vessel. A horizontal copper plate of 2 mm thickness was installed at the level of 33.3 cm, which separated the melt into two parts. The test consisted of five heating periods in the order of 18kW-I, 10kW-I, 5kW, 10kW-II and 18kW-II. The test vessel was externally cooled from the beginning of the test with a flow rate of ~1.3 kg/s. The water inlet temperature was approximately 289.3 K through the test. An insulation lid was installed at the top of the vessel [48].

LIVE-L7V A total of 210-liter simulant material was filled into the vessel, corresponding to 100% of a core inventory. The decay heat in the melt is simulated by 8 planes of electrical resistance heating wires, which can be controlled separately to realize homogenous power generation in the melt pool. The test consisted of four steady states with heating power of 29 kW, 24 kW, 18 kW and 9 kW. The external wall was cooled by water with flow rate of ~250 g/s at the power generation of 29 kW. The flow rate was reduced to ~200 g/s at 24 kW and 18 kW, and finally to ~150 g/s. A water-cooled lid was installed to cool the melt surface. There were four peripheral water inlets and one central outlet at the cooling lid. The cooling lid had a diameter of 920 mm and was mounted at a height of 413 mm from the vessel bottom. The inlet and outlet water temperatures for both external cooling and melt surface cooling were respectively ~293 K and ~303 K throughout the whole experiment [49].

LIVE-L11 A total of 190 liters of a non-eutectic melt was heated in the furnace up to ~623 K and was poured centrally into the test vessel. The test consisted of five heating plateaus in the order of 21 kW-I, 16.4 kW-I, 9 kW, 16.4 kW-II and 21 kW-II. The cooling vessel was initially filled with water at room temperature. The cooling water was then gradually heated by the heat released in the molten pool and its temperature reached the boiling temperature. A very low flow rate served as a compensation of evaporated mass and maintained the water level constant. For the upper boundary, an insulated upper lid was installed at the top of the test vessel.

FOREVER

The FOREVER test series performed at KTH provided a rich source of data to validate creep models [50], [51]. The facility employs a 1:10 scale steel vessel representing a RPV with internal radius of 188 mm and the wall thickness of 15 mm. The schematic view of the facility is shown in Fig. 2.2. The vessel consists of a cylindrical part (15Mo3) which is welded to a hemisphere (16MND5 or SA-533B1). The experiment was performed by pouring a binary oxide melt into the vessel at approximately 1500 K, heating the melt with a heater and pressurizing the vessel to 25 bar with argon. The simulant material employed was a mixture of 70wt% CaO–30wt% B_2O_3. The material data used in the analysis are summarized in Table 2.4.

EC-FOREVER-2 The EC-FOREVER-2 test was conducted with 16MND5 steel vessel [52]. Although the heating power of 38 kW and the internal pressure of 25 bar were planned,
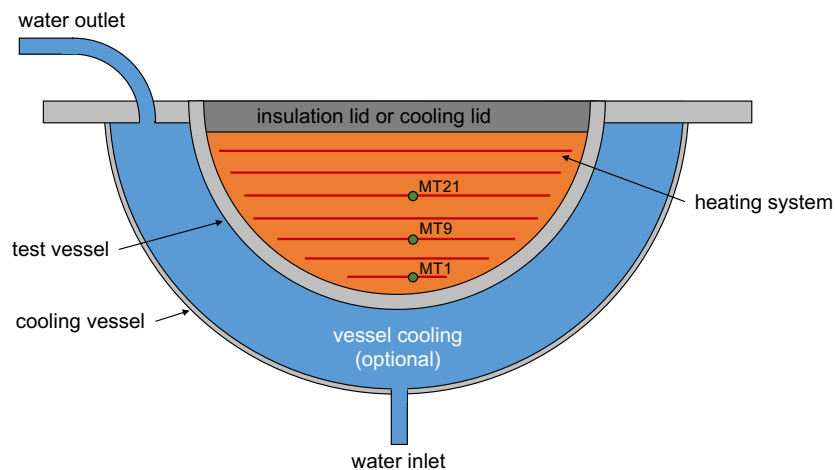
Figure 2.1: LIVE test facility and thermocouple positions (after [45])

the power reached only ~20 kW at the early phase of the experiment due to the technical failure [50]. At 12360 s, the power was regained and the pressure was set to 25 bar. The vessel failure occurred at around 3.5 hours after the initial pressurization and the failure location was about 50 mm below the weld line located at the angle of 73° from the vessel bottom.

EC-FOREVER-4 The EC-FOREVER-4 test was the only experiment in the FOREVER test series that was conducted with the American RPV steel SA533B1. The test condition was similar to the EC-FOREVER-2 experiment, having a heating power of ~38 kW and an inner pressure of ~25 bar, and similar results had been expected. The vessel, however, failed earlier and with different failure form [53], [54].

LHF and OLHF

The LHF (Lower Head Failure) and OLHF (OECD Lower Head Failure) experiments were performed at Sandia National Laboratories (SNL), USA [55], [31]. Models of a typical PWR lower head in the geometrical scale of 1:4.85 with SA533B1, a prototypical steel for American PWR, were used in the test. The LHF focused on high internal pressures (10 MPa) associated with TMI-2-like scenarios. The OLHF provided the data and insight to characterize the mode, timing and size of RPV lower head failure for conditions of lower to moderate pressure (2–5 MPa) with large wall temperature gradients (200–400 K difference).

Table 2.2: LIVE test conditions

	LIVE-L1	LIVE-L6	LIVE-L7V	LIVE-L11
Cooling medium	Air → Water	Water	Water	Saturated water
Cooling position	External vessel wall	External vessel wall	External vessel wall	External vessel wall
			Melt surface	
Amount of melt	120 liter	210 liter	210 liter	189 liter
Melt layer	1	2	1	1
Power plateau	2	5	4	5
	10 kW	18 kW-I	29 kW	21.1 kW-I
	7 kW	10 kW-I	24 kW	16.4 kW-I
		5 kW	18 kW	9.1 kW
		10 kW-II	9kW	16.4 kW-II
		18 kW-II		21.1 kW-II
Simulant material	Non-eutectic (80mol%KNO_3–20mol%$NaNO_3$)			

Table 2.3: Material properties of non-eutectic simulant debris (80mol%KNO_3–20mol%$NaNO_3$)

Specific heat (liquid) [J/(kg·K)]	1331 (at 573 K)
Specific heat (solid) [J/(kg·K)]	1060 (at 373 K)
Heat of fusion [J/kg]	161956
Liquidus temperature [K]	559
Solidus temperature [K]	439
Density [kg/m^3]	1868
Viscosity [Pa·s]	1.75×10^{-6}
Thermal conductivity (liquid) [W/(m·K)]	0.439
Thermal conductivity (solid) [W/(m·K)]	0.6

Table 2.4: Material properties of FOREVER simulant (70mol%CaO$_3$–20mol%B$_2$O$_3$)

Specific heat (liquid) [J/(kg·K)]	2200
Specific heat (solid) [J/(kg·K)]	1530
Heat of fusion [J/kg]	460000
Liquidus temperature [K]	1300
Solidus temperature [K]	1250
Density [kg/m^3]	2500
Viscosity [Pa·s]	4×10^{-5}
Thermal conductivity (liquid) [W/(m·K)]	3.0
Thermal conductivity (solid) [W/(m·K)]	2.0
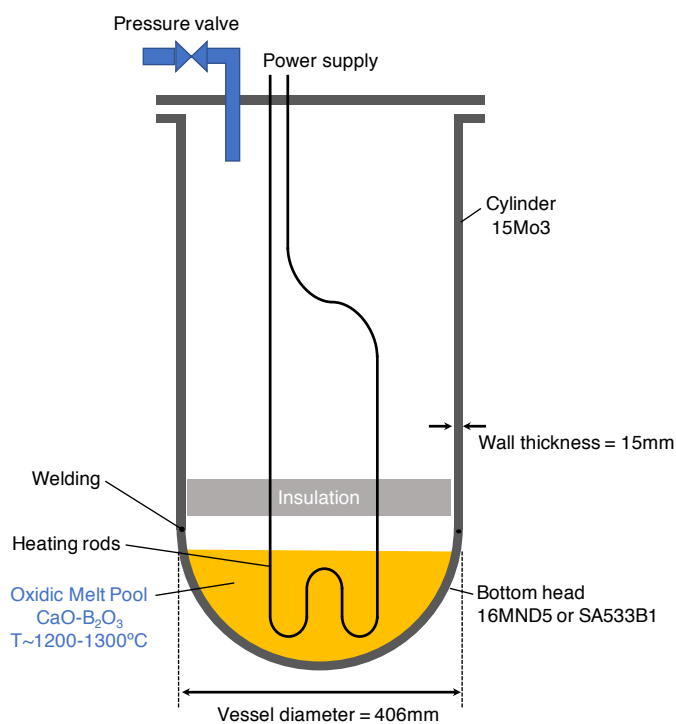
Figure 2.2: Schematic view of the FOREVER facility (after [56])

2.1.2 Numerical investigation

Reactor analysis codes

After the TMI-2 accident in 1979, the development of computer codes for simulation of severe accident scenarios was accelerated firstly in the United States and then progressively in the 1980s in Europe and Japan. The reactor analysis codes simulate the overall nuclear power plant response including the reactor coolant system, core heat-up and degradation, and source term to the environment. Their purpose is usually defined as yielding an overall analysis of severe accident with reasonably accurate estimates of the timing of the events and the consequences of the plant. Traditionally, the focus was on the source term determination for probabilistic safety assessment (PSA) Level 2 studies and the detailed studies on behavior of the lower head, where molten pool is formed, were not extensively conducted. Due to the recent high interest in IVR, re-assessment and improvement of the models in reactor analysis codes are necessary.

In reactor analysis codes such as MELCOR [57] and MAAP [58], a lumped-parameter method was used for prediction of thermal loads from an internally heated molten pool to its boundaries. The method is based on energy balance equation and heat transfer correlations describing turbulent natural convection in a molten pool or mixed natural convection in a molten metal fluid layer. Since the molten material is treated as a single uniform continuum, phase change problems cannot be considered, which is mostly the case with the oxide mixture of molten core.

A distributed-parameter method was used in the lower head analysis module in RELAP/ SCDAPSIM [59]. The method uses the modified effective conductivity to describe turbulent natural convection in a heated fluid layer with different initial and boundary conditions imposed to the top and lower boundaries. Although the effect of phase-change and crust formation can also be treated, application to the 3D complex geometry is limited.

Lower head specific analysis models

(a) Effective Convectivity Conductivity Model (ECCM)

A two-dimensional distributed parameter method, named the Effective Convectivity Conductivity Model (ECCM) was developed by Bui and Dinh [60] to describe convective heat transfer in an internally heated melt pool. The idea of the model is that the heat transfer inside the internally heated melt pool is assumed to be driven by two mechanisms: (a) vertical upward movement of plumes delivering heat to the upper boundary; and (b) the horizontal heat transfer to the cooled side wall through the liquid boundary layer developing downwards along the cooled curved wall. The first mechanism is modeled using a so called effective convectivity approach, in which the convective term in heat transfer is defined analytically. The second mechanism is modeled by means of the effective diffusivity approach [61], [62].

The mathematical formulation of the problem is based on the two-dimensional energy conservation equation:

$$\frac{\partial(\rho C_p T)}{\partial t} + \nabla \cdot (\rho C_p \mathrm{V} T) = \nabla \cdot (k\nabla T) + Q_v \tag{2.1}$$

In order to solve Eq. (2.1), the velocity $\mathrm{V} = [u, v]$ is analytically determined from the pool characteristics and the boundary conditions. The horizontal velocity component v is neglected in this model and the buoyancy-induced vertical velocity u is defined from the analytical and experimental correlations of heat transfer coefficients on the boundaries. The effective upward and downward velocities (u_{up} and u_{down}) are estimated from the simple heat balance equations:

$$u_{up} = \frac{\alpha}{L}(\overline{Nu} - Nu_{low}) \tag{2.2}$$

$$u_{down} = \frac{\alpha}{L}\left(\frac{\overline{Nu}Nu_{low}}{Nu_{up} + Nu_{low}} - Nu_{low}\right) \tag{2.3}$$

where α is thermal diffusivity, L is the height of the pool, $Nu_{up} = 0.338Ra_i^{0.227}$ [63] and $Nu_{low} = 1.389Ra_i^{0.095}$ [34], and $\overline{Nu}$ is given as follows:

$$\overline{Nu} = \frac{0.0471\Pi_N^{1/3}}{1 - 1.734\Pi_N^{-1/9}}; \quad \Pi_N = \frac{Ra_i}{1 + 0.0414Pr^{-1}} \tag{2.4}$$

For the horizontal heat transfer, the effective conductivity k_x for a vertical position is given as follows, using the thermal conductivity of the melt pool k:

$$k_x = k \times Nu_{side,local} \tag{2.5}$$

where the sideward heat transfer coefficient for ECCM is given by an Eckert-type correlation [64]:

$$Nu_{side,local} = 0.508Pr^{0.25}\left(\frac{20}{21} + Pr\right)^{-0.25}Ra_{local}^{0.25} \tag{2.6}$$

The vertical conductivity is assumed to be unchanged as $k_y = k$.

The ECCM was implemented in ANSYS by Willschütz et al. [65], further modified and extended for a coupled thermo-mechanical analysis. Thin boundary layers enveloping a debris cake were introduced as additional modeling parameters and used to adjust the temperature profile and energy splitting. The effective conductivity of the pool's well-mixed region is given by a large value, while in the stratified region of the melt pool, directional conductivities are applied. A two-way coupling between the thermal and mechanical model was introduced: first the transient temperature field was calculated and then the transient mechanical calculation was performed applying the updated temperature profile at each time step. A previous investigation of Willschütz et al. [66] showed that slight temperature difference with 10 K at temperature levels above 1000 K had significant effects concerning the vessel failure time.

The thermo-mechanic behavior of the vessel wall of VVER-1000 reactor in a scenario containing a developed molten pool was analyzed by Tusheva et al. [67]. The initial condition of the molten pool was based on an ASTEC simulation to start the ECCM calculation. Thus, the mechanical behavior was not taken into account for thermal calculation. It had been reported that the ECCM was not completely capable of reproducing the temperature distributions in the pool for high internal Rayleigh number, especially for non-spherical pool geometry [65]. A redistribution parameter for the heat generation was introduced to obtain the correct temperature profile in a non-spherical lower head.

Although the extended ECCM has given insights on vessel failure and importance of recursively coupled thermo-mechanical analysis, the application of the recursively coupled model was still limited to the analysis of experiments. A two-way coupling of the model and a reactor analysis code has not yet been performed, although slight temperature difference might affect prediction of the vessel failure time. Moreover, the model requires a high resolution and is cumbersome in treatment of the boundary layer or heat redistribution, especially for three-dimensional flow, and incorporation of the local effect.

(b) Phase-Change Effective Convectivity Model (PECM)

The Phase-Change Effective Convectivity Model (PECM) was developed by Tran and Dinh at KTH [68],[69]. It is a model for describing turbulent natural convection heat transfer and has been extensively validated against a set of experiments. The PECM uses directional effective heat-convecting velocities, or simply named "characteristic velocities" to effectively transfer the heat generated in the fluid volume toward the cooled boundary (wall) in an amount equal to the convective heat transport in the respective direction. The use of effective convectivity helps eliminate the need to solve a complete set of Navier-Stokes and energy equations with instantaneous fluid velocities. Instead, the energy conservation equation is solved using the effective convective terms represented by the characteristic velocities U:

$$\frac{\partial(\rho C_p T)}{\partial t} + \left(\frac{\partial \rho C_p U_x T}{\partial x} + \frac{\partial \rho C_p U_y T}{\partial y} + \frac{\partial \rho C_p U_z T}{\partial z} \right) = \nabla \cdot (k \nabla T) + Q_v \tag{2.7}$$

Computationally, the heat source Q_v can be combined with the effective convective terms in a modified source term S_c as follows:

$$S_c = Q_v - \left(\frac{\partial \rho C_p U_x T}{\partial x} + \frac{\partial \rho C_p U_y T}{\partial y} + \frac{\partial \rho C_p U_z T}{\partial z} \right) \tag{2.8}$$

Therefore, the final form of the energy conservation equation to solve is as follows:

$$\frac{\partial(\rho C_p T)}{\partial t} = \nabla \cdot (k \nabla T) + S_c \tag{2.9}$$

The characteristic velocities are given for each direction as shown in Figure 2.3. They are derived using energy balance equations and presented through thermal diffusivity and Nusselt numbers as follows:

$$U_{up} = \frac{\alpha}{H_{pool}}\left(Nu_{up} - \frac{H_{pool}}{H_{up}}\right) \tag{2.10}$$

$$U_{side} = \frac{\alpha}{H_{pool}}\left(Nu_{side,local} - \frac{2 \times H_{pool}}{W_{pool}}\right) \tag{2.11}$$

$$U_{down} = \frac{\alpha}{H_{pool}}\left(Nu_{down} - \frac{H_{pool}}{H_{down}}\right) \tag{2.12}$$

where H_{pool} is the height of the melt pool, H_{up} is the height of the pool upper mixed region, H_{down} is the height of the lower stratified region, and W_{pool} is pool width. H_{up} (and H_{down}) is assumed to be as follows:

$$H_{up} = \frac{Nu_{up}}{Nu_{up} + Nu_{side} + Nu_{down}}H_{pool} \tag{2.13}$$

Assuming that the coordinate system shown in Fig. 2.3 is used, the characteristic velocities can be given as follows:

$$U_x = U_{side} \tag{2.14}$$

$$U_y = \begin{cases} U_{up} & (\partial T/\partial y < 0) \\ U_{down} & (\partial T/\partial y \geq 0) \end{cases} \tag{2.15}$$

$$U_z = U_{side} \tag{2.16}$$

The upward, sideward and downward Nusselt numbers were empirically obtained and expressed as follows using the internal Rayleigh number [34]:

$$Nu_{up} = 0.345 Ra_i^{0.233} \tag{2.17}$$

$$Nu_{side} = 0.85 Ra_i^{0.19} \tag{2.18}$$

$$Nu_{down} = 1.389 Ra_i^{0.095} \tag{2.19}$$

In order to describe the sideward heat transfer coefficient profile due to the boundary layer development along an inclined cooled surface, the Eckert-type correlation [70] is used:

$$Nu_{side,local} = 0.508 Pr^{0.25}\left(\frac{20}{21} + Pr\right)^{-0.25} Ra_{local}^{0.25} \tag{2.20}$$

where Ra_{local} is the local Rayleigh number and is expressed using the distance from the melt pool surface h:

$$Ra_{local} = \frac{g\beta\Delta T h^3}{\alpha\nu_{vis}} \tag{2.21}$$

In a developed molten pool, a metal layer is assumed to appear on the top of an oxide layer. The metal layer is heated from below and cooled from the top (and side), which lead to
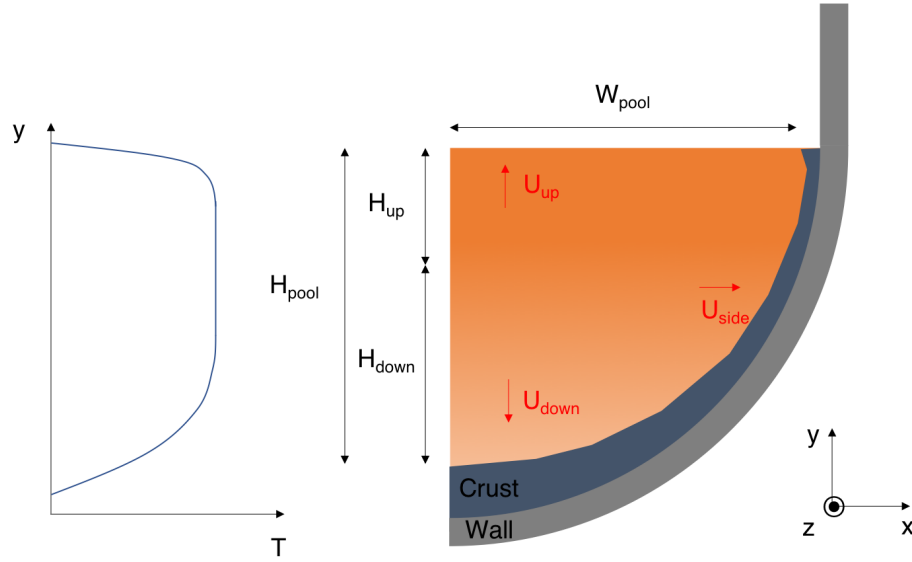
Figure 2.3: Illustration of homogeneous corium pool

Rayleigh-Bénard convection as shown in Fig. 2.4. For such a fluid layer, the characteristic velocity is positive on a cooled surface and negative on a heated surface. The driving force of upward convection is the temperature difference between the lower and upper boundaries, while the driving force for the boundary layer development along the inclined phase-change boundary is the difference between the bulk and liquidus temperatures [48], [71]. The PECM calculates two external Rayleigh numbers (Ra_e and $Ra_{e,local}$) based on the temperature differences to determine the heat transfer coefficients. The Globe-Dropkin correlation [36] is used for calculation of the upward characteristic velocity:

$$Nu_{up} = 0.069 Ra_e^{0.333} Pr^{0.074}$$
$$\text{for} \quad 3 \times 10^5 < Ra_e < 7 \times 10^9; \quad 0.02 < Pr < 8750 \tag{2.22}$$

and the Churchill-Chu correlation [37] is used for the sideward characteristic velocity:

$$Nu_{side}^{1/2} = 0.825 + \frac{0.387 Ra_{e,local}^{1/6}}{[1 + (0.492/Pr)^{9/16}]^{8/27}} \tag{2.23}$$

The characteristic velocities are determined as follows by using the above Nusselt numbers:

$$U_{up} = \frac{2\alpha}{H_{m,pool}} \left(Nu_{up} - 1 \right) \tag{2.24}$$

$$U_{side} = \frac{\alpha}{H_{m,pool}} \left(Nu_{side} - \frac{H_{m,pool}}{W_{m,pool}} \right) \tag{2.25}$$

Villanueva et al. [72] implemented the PECM in ANSYS Fluent and transient heat transfer characteristics were provided for thermo-mechanical strength calculations of a Swedish BWR lower head. The creep analysis model was coupled in order to take into account both the
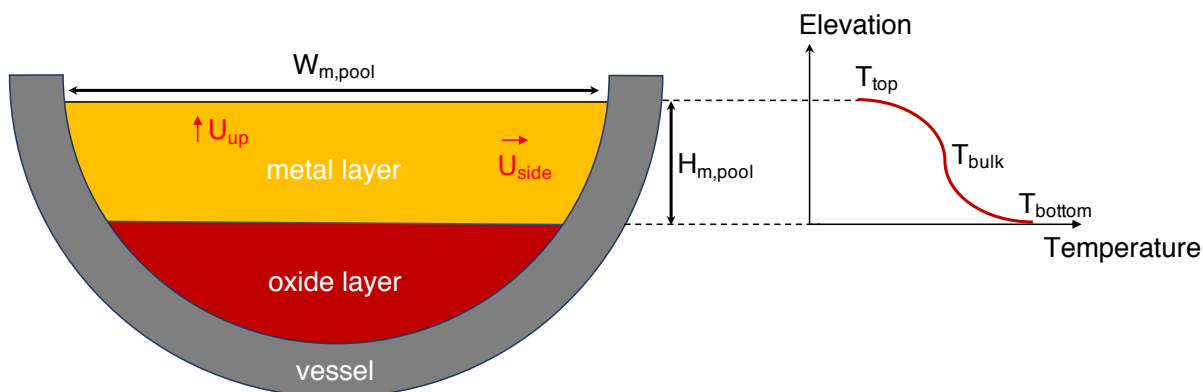
Figure 2.4: Schematic illustration and vertical temperature profile of a fluid layer with classical Rayleigh-Bénard convection (metal layer), heated from bottom and cooled from top

thermal and integral mechanical loads on the RPV. Two cases with assumptions of different melt height were analyzed. The external surface of the vessel wall was fully insulated with a small heat flux in case without external cooling. Once the external cooling is applied, the Dirichlet boundary condition with water saturation temperature was used. Since the deformation of the vessel wall was assumed to have negligible effect on the melt pool heat transfer, only one-way coupling has been employed.

The coupled analysis of PECM and MELCOR was conducted by Dietrich [73], in order to calculate whole nuclear power plant behavior during the accident in which the molten pool is formed in the lower head. Since MELCOR did not capture the behavior of the molten pool material in the lower head in sufficient detail, the coupled analysis has improved the prediction of molten core material during the severe accident. In a severe accident analysis with MELCOR–PECM, the PECM calculation was firstly started when all the molten material was slumped into the lower head. The vessel rupture was assumed when the vessel wall temperature increased abruptly induced by the heat flux from the oxide pool exceeding the CHF of external cooling side.

2.2 Objective of the work

To be sure that the research conducted on severe accident is efficient and focusing on relevant topics, the ranking of research issues reflecting the Fukushima-Daiichi accidents was summarized by Klein-Heßling et al. [32] in the framework of the Severe Accident Research Priority (SARP). The phenomena during in-vessel accident progression concerning the lower head listed in the ranking are: (a) corium behavior in lower head, (b) integrity of RPV due to external vessel cooling, and (c) RPV failure mode. A deeper understanding of these severe accident phenomena and accident progression is still important. Since the costs of experiments are prohibitively high and large-scale experiments cannot be conducted iteratively, numerical tools must be developed at the same time to simulate a real-scale severe accident and to improve further SAM measures. Although, after the Fukushima-Daiichi accident, the importance of researches on BWR-specific topics is emphasized, few experimental data is available for the lower head behavior of BWR that can be used for validation of numerical tools. Thus, as a first step, the focus of the study is on PWR lower head behavior.

As mentioned in Section 2.1.2, RELAP/SCDAPSIM includes a lower head heat transfer analysis module and has a potential to be applied for IVR related scenarios. However, the model has been validated only with a simple experiment and with CFD analysis during the developmental phase [74] and has not been recently assessed with recent molten pool experiments. Therefore, re-evaluation and improvement of the model are necessary due to the recent interest on IVR strategy. In order to improve the prediction of vessel failure, a detailed structure analysis model should be included. In order to reach this objective, this study is conducted in the following manner:

- Assessment and improvement of the COUPLE module, the lower head heat transfer analysis model of a reactor analysis code RELAP/SCDAPSIM

- Implementation and extension of PECM to include structure analysis model and creep data base.

- Coupling of the RELAP/SCDAPSIM and the extended PECM, which allows analysis of core-melt severe accident scenario with consideration of detailed creep deformation and failure of the RPV lower head

- Application of the coupled analysis tool to IVR scenarios

3 Numerical analysis models for IVR

3.1 Description of RELAP/SCDAPSIM

The RELAP/SCDAPSIM computer code is designed to describe the overall reactor coolant system (RCS), thermal-hydraulic response, core damage progression, fission product release and transport during severe accidents [74]. The code was originally developed at the Idaho National Laboratory (INL –Former: Idaho National Engineering and Environmental Laboratory (INEEL)) under the primary sponsorship of the Office of Nuclear Regulatory Research of the U.S. Nuclear Regulatory Commission (NRC). The code is being developed as part of the international SCDAP Development and Training Program (SDTP) and its activities are summarized by Allison and Hohorst [59].

The code is the result of merging the RELAP5 (Reactor Excursion and Leak Analysis Program), SCDAP (Severe Core Damage Analysis Package) and COUPLE models. The RELAP5 models calculate the overall RCS thermal-hydraulics, control system interactions, reactor kinetics, and the transport of non-condensable gases. The RELAP5 code is based on a two-fluid model allowing for unequal temperatures and velocities of the fluids that is solved by either a semi-implicit or nearly-implicit numerical scheme to permit economical calculation of system transients. The SCDAP code models the core behavior during a severe accident from the heat-up of fuel rod till the relocation of molten material to the lower head. Once the molten core relocates into the lower head, the heat transfer in the lower head of RPV is treated by the COUPLE models that is a two-dimensional, finite element, steady-state and transient heat conduction model, solving the two-dimensional energy equation.

The RELAP/SCDAPSIM code includes many generic component models from which general systems can be simulated. The component models include fuel rods, control rods, pumps, valves, pipes, heat structures, reactor point kinetics, electric heaters, jet pumps, turbines, separators, accumulators, and control system components. In addition, special process models are included for effects such as form loss, flow at an abrupt area change, branching, choked flow, boron tracking, and non-condensable gas transport. Detailed descriptions of each model can be found in the code manual [74], [75].

3.1.1 RELAP5

The RELAP5 hydrodynamic model is a one-dimensional, transient, two-fluid model for flow of a two-phase steam-water mixture that can contain non-condensable components in the steam phase and/or a soluble component in the water phase. The two-fluid equations of motion that

are used as the basis for the RELAP5 hydrodynamic model are formulated in terms of volume and time-averaged parameters of the flow. Phenomena that depend upon transverse gradients, such as friction and heat transfer, are formulated in terms of the bulk properties using empirical transfer coefficient formulations. In situations where transverse gradients cannot be represented within the framework of empirical transfer coefficients, such as subcooled boiling, additional models specially developed for the particular situation are employed.

The RELAP5 thermal-hydraulic model solves eight field equations for eight primary dependent variables: pressure, phasic specific internal energies, vapor volume fraction (void fraction), phasic velocities, non-condensable quality and boron density. The independent variables are time and distance. Non-condensable quality is defined as the ratio of the non-condensable gas mass to the total gaseous phase mass. The secondary dependent variables used in the equations are phasic densities, phasic temperatures, saturation temperature and non-condensable mass fraction in non-condensable gas phase.

The basic field equations for the two-fluid non-equilibrium model consist of two phasic continuity equations, two phasic momentum equations and two phasic energy equations. The model can be extended to include a non-condensable component in the gas phase. The non-condensable component is assumed to move with the same velocity and to have the same temperature as the vapor phase. The steam/non-condensable mixture conditions can still be non-homogenous and non-equilibrium compared to the liquid and saturation conditions. The general approach for inclusion of the non-condensable component consists of assuming that all properties of the gas phase are mixture properties of the steam/non-condensable mixture. In addition, boron concentration in the liquid field can also be treated in the RELAP5. An Eulerian boron tracking model is used that simulates the transport of a desolved component in the liquid phase. The detailed modeling can be found in the code manual.

3.1.2 SCDAP

The SCDAP code models the core behavior during a severe accident. Treatment of the core includes fuel rod heat-up, ballooning and rupture, fission product release, rapid oxidation, Zircaloy melting, UO_2 dissolution, ZrO_2 breach, flow and freezing of molten fuel and cladding, and debris formation and behavior. The code also models control rod and flow shroud behavior.

3.1.3 COUPLE

Natural convection of liquefied debris

The COUPLE module is a two-dimensional, finite element, steady-state and transient heat conduction model [74]. The code solves the two-dimensional energy equation. An effective thermal conductivity is used to represent the heat transfer in regions that contain partially or completely molten core material and where the heat transfer is dominated by natural convection instead of conduction. The effective thermal conductivity of molten corium is multiplied by a large number to represent mixing of the molten material due to natural convection. Fig. 3.1 is
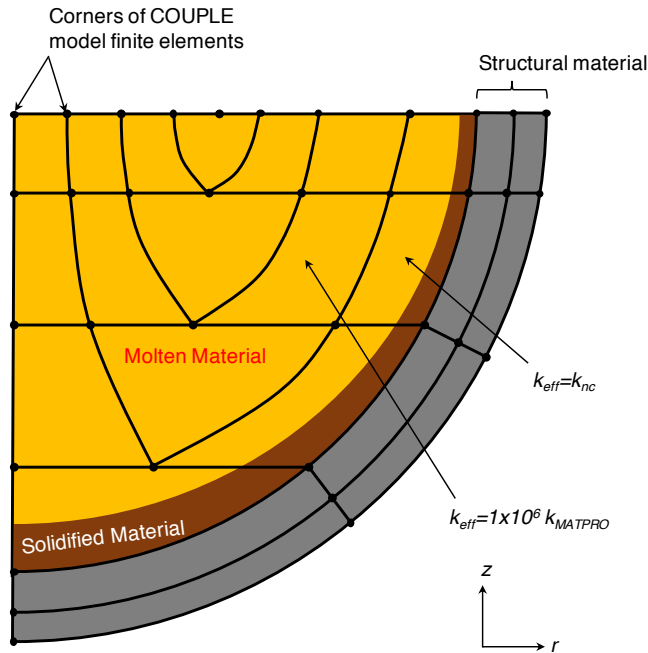
Figure 3.1: Schematic illustration of COUPLE elements and effective thermal conductivity (after [74])

a schematic illustration of a COUPLE mesh that shows the finite elements in a COUPLE mesh at which an effective thermal conductivity is calculated. In Fig. 3.1, k_{eff} is the effective thermal conductivity of the element, k_{MATPRO} is the thermal conductivity of the element as calculated by MATPRO [74], and k_{nc} is the effective thermal conductivity of the element that accounts for natural convection. The natural convection heat transfer correlations used to calculate heat transfer at the liquid-solid interfaces assume that the bulk molten material is at a uniform temperature. Therefore, the multiplication factor on thermal conductivity for elements with molten material needs to be sufficiently large that all elements with molten material are at the same temperature. The multiplication factor is defined to have a value of 1×10^6. With this value of the multiplication factor, the maximum variation in the calculated temperature of molten material is less than 4 K.

A local heat transfer model is applied to calculate the effective thermal conductivity of a COUPLE finite element that contains molten material that interfaces with solidified material. Heat is driven by natural convection through the molten material in the left part of the element to the liquid-solid interface and then is transferred by conduction through the solidified layer to the right boundary of the element.

Heat transfer correlations

According to Lee et al. [76], natural convection plays an important role in determining thermal-hydraulic phenomenon in the debris pool. The heat transfer inside the corium pool can be characterized by buoyancy-induced flows arising from internal decay heating. The heat transfer coefficient for the liquid-solid interface due to natural convection in the molten material is cal-

Table 3.1: Nu-Ra_i relations

	Correlations	Ra_i	Pr
COUPLE	$Nu_{up} = 0.36 Ra_i^{0.23}$	$7{\times}10^6$– $5{\times}10^{10}$	~7
	$Nu_{down} = 0.54 Ra_i^{0.18}$		
ACOPO	$Nu_{up} = 1.95 Ra_i^{0.18}$	10^{12}–$2{\times}10^{16}$	~7
	$Nu_{down} = 0.3 Ra_i^{0.2}$		
UCLA	$Nu_{up} = 0.403 Ra_i^{0.226}$	$2{\times}10^{10}$–$1.1{\times}10^{14}$	8.2–9.5
	$Nu_{down} = 0.55 Ra_i^{0.2}(H/R)^{0.25}$		

H: height of molten pool, R: radius of molten pool

Table 3.2: Local heat transfer correlations along the vessel wall

		Correlations
mini-ACOPO	$\dfrac{Nu_{down}(\theta)}{Nu_{down}} =$	$\begin{cases} 0.1 + 1.08\left(\dfrac{\theta}{\theta_{max}}\right) - 4.5\left(\dfrac{\theta}{\theta_{max}}\right)^2 + 8.6\left(\dfrac{\theta}{\theta_{max}}\right)^3, & 0 \le \dfrac{\theta}{\theta_{max}} \le 0.6 \\[2ex] 0.41 + 0.35\left(\dfrac{\theta}{\theta_{max}}\right) + \left(\dfrac{\theta}{\theta_{max}}\right)^2, & 0.6 < \dfrac{\theta}{\theta_{max}} \le 1 \end{cases}$
UCLA	$\dfrac{Nu_{down}(\theta)}{Nu_{down}} =$	$\begin{cases} C_1 \sin\Theta + C_2 \cos\Theta & (0 \le \dfrac{\theta}{\theta_{max}} \le 0.73) \\[2ex] C_3 \sin\Theta - C_4 \cos\Theta & (0.73 < \dfrac{\theta}{\theta_{max}} \le 1) \end{cases}$

$C_1 = -0.31\cos\theta_{max} + 1.06 \quad C_2 = 0.24\cos\theta_{max} + 0.15$

$C_3 = -1.2\cos\theta_{max} + 2.6 \qquad C_4 = -2.65\cos\theta_{max} + 3.6$

$\Theta = \dfrac{\pi}{2}\dfrac{\theta}{\theta_{max}}$

culated using correlations developed from experimental data. These correlations were developed from the results of experiments that measured the natural convection heat transfer coefficients at the boundary of a pool of fluid with internal heat generation. The correlations calculate heat transfer coefficients at the bottom and top surfaces of the molten pool and at the sides of the molten pool. They are given as the Nusselt number by a function of the internal Rayleigh number. The correlation originally used in COUPLE is based on the one obtained by Mayinger [77]. In this study, the correlations from more recent experiments are additionally implemented as a comparison (Table 3.1). The local heat transfer along the hemispherical vessel wall is not uniform but depends on the angular position position from the centerline of the molten pool. The local downward Nusselt number is obtained by multiplying the normalization factor to the average downward Nusselt number. The normalization correlations are developed through the experimental studies and given in Table 3.2 and Fig. 3.2. COUPLE uses the normalization factor based on the experimental data obtained by Jahn and Reineke [74]. In Table 3.2, θ is the polar angle from the vessel bottom and $\theta_{\max}$ is the maximum angle where the molten pool exists.
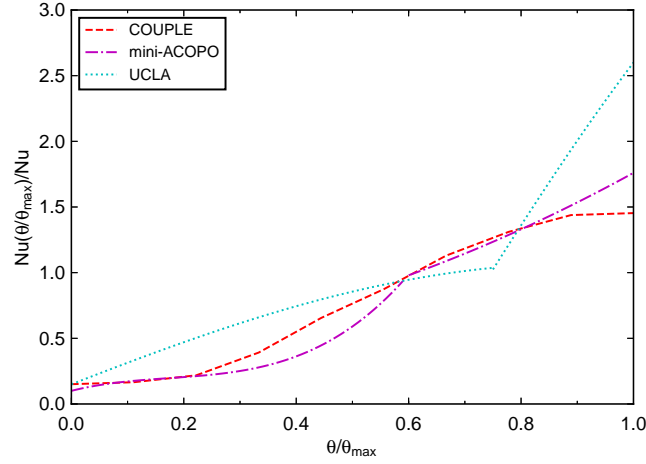
Figure 3.2: Ratio of local Nusselt number to mean Nusselt number as a function of normalized polar angle

Heat transfer at surface of COUPLE mesh

The COUPLE finite element mesh makes use of a connection to a hydrodynamic volume, allowing heat transfer to and from a surrounding fluid. Convective and radiative heat transfer conditions may be applied at all surfaces of a finite-element mesh exposing to hydrodynamic volumes: the interface of melt and inner atmosphere, the interface of inner vessel wall and inner atmosphere, and the interface of external vessel wall and external atmosphere. Convective heat transfer coefficients and sink temperatures are determined at the surface of the COUPLE finite element mesh. The emissivity of 0.7 is currently used for every surface in the radiation calculation. The boundary conditions are:

$$-k_{eff}\frac{\partial}{\partial n}T(z,r) = h_c(z,r)[T(z,r) - T_c(z,r)] + q_{rad}(z,r) \tag{3.1}$$

where

$T(z,r)$ temperature of external surface of node on COUPLE finite element mesh with coordinates of (z, r) [K],

k_{eff} effective thermal conductivity at location with coordinates (z, r) [W/(m·K)],

r radius of node on external surface on mesh [m],

z elevation of node on external surface on mesh [m],

n coordinate in direction normal to external surface [m],

$h_c(z,r)$ RELAP5-calculated convective heat transfer coefficient for node on external surface with coordinates of (z, r) [W/(m²·K)],

$T_c(z,r)$ RELAP5-calculated temperature of the fluid at surface coordinates of (z, r) [K],

$q_{rad}(z,r)$ radiation heat flux [W/m²].

Creep rupture model of structural components

In RELAP/SCDAPSIM, a model based on creep rupture theory is used to calculate the damage and nearness to rupture of structural components. The materials that can be modeled for creep rupture are (a) A-508 Class 2 carbon steel, (b) 316 stainless steel and (c) Inconel 600. For 316 stainless steel and Inconel 600 materials, the Larson-Millar theory [78] is used. For A-508 Class 2 carbon steel, the Manson-Haferd theory [79] is applied for the lower range of stress and the Larson-Millar theory for the higher range of stress.

A parameter that measures creep damage is calculated at each time step for each structure being monitored for creep rupture. The creep damage is evaluated by the equation:

$$D_{cr}(t + \Delta t) = D_{cr}(t) + \frac{\Delta t}{t_{frac}(t)} \tag{3.2}$$

where D_{cr} is creep damage, Δt is time step at current problem time [s], t_{frac} time required for the structure to fail by creep rupture at the current state of temperature and stress [s] , and t is problem time [s]. D_{cr} is in the range of zero and one: if zero, the structure has not experienced any creep damage; and if one, the structure has failed due to creep damage. The equation for calculating t_{frac} is dependent on the material composition and stress and summarized in Table 3.3. The temperature term in the equations shown in Table 3.3 is the average temperature through the thickness of the wall. For the lower head of a reactor vessel, the stress term in the equations is calculated as follows:

$$\sigma = \frac{P_i r_i^2 - P_o r_o^2}{(r_o - r_i)^2} + 0.5(P_i - P_o) \tag{3.3}$$

where σ, P_i, P_o, r_i and r_o are stress, internal pressure, external pressure, inner radius and external radius of the wall, respectively.

Table 3.3: Equations for calculating the time to creep rupture t_{frac}

Material	Range of stress [MPa]	Equation for creep rupture time [s]	Theory
A-508 carbon steel	$0 < \sigma < 96.5$	$t_r = 10^{\left[\frac{T-1503.69}{P}+3.499\right]}$	MH
		$P = 158.233\log(\sigma) - 255.346$	
	$96.6 \leq \sigma$	$t_r = 10^{\left[\frac{P}{T}-20\right]}$	LM
		$P = 9603.0\log(\sigma) - 46454.0$	
316 stainless steel	$0 < \sigma < 358.5$	$t_r = 10^{\left[\frac{P}{T}-20\right]}$	LM
		$P = -13320.0\log(\sigma) + 54870.0$	
	$358.5 \leq \sigma$	$t_r = 10^{\left[\frac{P}{T}-20\right]}$	LM
		$P = -64000.0\log(\sigma) + 142000.0$	
Inconel 600		$t_r = 10^{\left[\frac{P}{T}-15\right]}$	LM
		$P = -11333.0\log(\sigma) + 43333.0$	

LM: Larson-Millar, MH: Manson-Haferd, T: temperature [K]

3.2 Development of a thermal structural analysis solver (PECM/S)

3.2.1 Thermal analysis model

In the molten pool in the RPV lower head, natural convection occurs due to the internal heat generation in the corium pool and the external cooling of the RPV walls. Since it is computationally expensive to simulate this complex behavior by solving a set of Navier-Stokes equations, a number of models using lumped parameter methods and distributed parameter methods are developed, in order to construct a computationally-effective and sufficiently-accurate simulation platform. In the previous study by Dietrich [73], the PECM has been implemented in OpenFOAM. In this implementation, only the model for internally heated pool was considered. In my study, the model for a metal layer was additionally implemented into the OpenFOAM in order to be able to simulate a stratified pool. Detailed description is given in Section 2.1.2.

3.2.2 Structural analysis model

The RPV lower head is loaded mechanically by the weight of the molten pool and of the vessel, the internal pressure and the temperature field. The primary stresses are the internal pressure and the gravity, which are not relieved by the deformation of the vessel wall, but they are even increased due to the reduction of wall thickness. The temperature gradients cause secondary stresses, which are relieved by visco-plastic deformation. Creep and plasticity mechanisms play a decisive role in the failure process of the RPV wall. In my study, three parts of deformation have been considered: elastic deformation, plasticity and creep. The plasticity is a prompt process, taking place only above the yield stress, while creep is a time dependent process at elevated temperatures, occurring at rather low stress. They can occur simultaneously and the corresponding material damage is evaluated by the damage module. The models are based on the previous researches by Willschütz et al. and Mao et al. [66], [80] and are implemented into OpenFOAM in this study.

Elastic deformation and plasticity

The elastic material properties are assumed to be isotropic and can be completely characterized by the temperature-dependent Young's modulus and the constant Poisson's ratio (ν_p=0.3). To represent the plastic deformation, a concept of the multi-linear isotropic hardening model is used, in which plasticity is represented by a function of stress over strain consisting of six linear sections. At each temperature, the six points of the stress-strain curves are defined as follows by Willschütz et al. [66]:

- Point 1: Stress at true strain of 0.0005. Pure elastic deformation is assumed until this point.
- Point 2: Stress at true strain of 0.002.
- Point 3: Stress at true strain of 0.01.
- Point 4: Stress at true strain of 0.05.
- Point 5: Highest true stress observed before necking at the according true strain.
- Point 6: Maximum stress at the fracture strain.

Table 3.4: Creep parameters for the French steel 16MND5

T [K]	873.15	973.15	1073.15	1173.15	1273.15	1373.15	1473.15	1573.15
d_1 [1/s]	3.890E-14	2.394E-12	1.412E-11	5.672E-11	2.540E-10	1.890E-09	1.571E-08	2.954E-07
d_2 [–]	3.418	3.411	3.316	3.366	3.367	3.340	3.346	3.620
d_3 [–]	-0.201	-0.218	-0.454	-0.455	-0.459	-0.470	-0.476	-0.436

Creep model

The creep strain rate can be formulated as follows with a number of free parameters:

$$\dot{\varepsilon} = d_1 \cdot \sigma^{d_2} \cdot \varepsilon^{d_3} \cdot \exp\left(-\frac{d_4}{T}\right) \tag{3.4}$$

The constants d_1, d_2, d_3 and d_4 are used to adapt the creep laws to a number of creep tests, each of which performed at constant nominal load and temperature. The above equation can, however, only handle the primary creep stage and the secondary creep stage ($\ddot{\varepsilon}_{cr} = 0$), while it is necessary to capture also the tertiary creep stage ($\ddot{\varepsilon}_{cr} > 0$), where the strain rate exponentially increases due to reduction of material resistance caused by necking phenomena, internal cracks or voids. In order to reproduce the later creep stages, the damage parameter (D) is introduced taking into account the material deformation, which is expressed between 0 (no damage) and 1 (completely damaged). The creep strain increment is coupled with the damage and is evaluated as follows:

$$\Delta\varepsilon_{cr} = \frac{\dot{\varepsilon}_{cr}}{1 - D}\Delta t \tag{3.5}$$

The creep strain rate obtained by the material creep acceleration is realized by the damage coupling, i.e. by the factor of $(1 - D)^{-1}$. A creep database for two types of steels is considered in the model: the French steel 16MND5 and the American steel SA533B1. In practice, it is difficult to achieve a satisfying fit for a wide range of temperatures and stresses with only one set of coefficients as shown in Eq. (3.4). Therefore, the strain hardening formulation of power law creep is given for each temperature as Eq. (3.6) and the creep strain rate between two temperature points is interpolated.

$$\dot{\varepsilon}_{cr} = d_1 \cdot \sigma^{d_2} \cdot \varepsilon^{d_3} \tag{3.6}$$

The database for the French steel 16MND5 was developed by Altstadt and Mössner [81] and is summarized in Table 3.4. The material characterization for the American steel SA533B1 was conducted during the LHF and OLHF test program at SNL [31]. The creep parameters were calculated based on the correlation proposed by SNL and are given in Table 3.5. Since the primary creep did not show a noticeable instantaneous strain that is often seen in other materials, the exponent of strain (d_3) has been taken as unity.

Table 3.5: Creep parameters for the American steel SA533B1

T [K]	800	900	1000	1050	1150	1250	1350	1500
d_1 [1/s]	3.933E-17	3.324E-15	4.682E-13	5.136E-12	1.582E-10	8.455E-10	5.555E-09	2.987E-08
d_2 [–]	4.2152	4.2152	4.2152	3.6675	3.6675	3.6675	3.6675	3.6675
d_3 [–]	1.0	1.0	1.0	1.0	1.0	1.0	1.0	1.0

Material damage

The material damage increment due to creep and plastic strains are incrementally accumulated for each element at the end of each time step and given as follows:

$$\Delta D = \left[\frac{\Delta\varepsilon_{cr}}{\varepsilon_{cr}^{frac}(\sigma, T)} + \frac{\Delta\varepsilon_{pl}}{\varepsilon_{pl}^{frac}(T)}\right] R_\nu \tag{3.7}$$

where creep fracture strain ε_{cr}^{frac} is set for each temperature level. The plastic fracture strain ε_{pl}^{frac} is obtained from the last point of the stress-strain curve at corresponding temperature. The triaxiality factor R_ν considers the damage behavior in dependence on the triaxiality of the stress tensor [82]:

$$R_\nu = \frac{2}{3}(1 + \nu_p) + 3(1 - 2\nu_p)\left(\frac{\sigma_h}{\sigma_{eqv}}\right)^2 \tag{3.8}$$

where σ_h and σ_{eqv} are hydrostatic stress and von-Mises equivalent stress, respectively.

Formulation

The plasticity and creep term are added into the steady-state governing equation expressed in the following incremental form:

$$\nabla \cdot \left\{\mu\nabla(d\mathrm{u}) + \mu[\nabla(d\mathrm{u})]^T + \lambda\mathrm{Itr}[\nabla(d\mathrm{u})] - \underbrace{[2\mu(d\varepsilon_p) + \lambda\mathrm{Itr}(d\varepsilon_p)]}_{\text{plasticity}} - \underbrace{[2\mu(d\varepsilon_{cr}) + \lambda\mathrm{Itr}(d\varepsilon_{cr})]}_{\text{creep}}\right\} = 0$$
$$\tag{3.9}$$

where $d\mathrm{u}$, $d\varepsilon_p$, $d\varepsilon_{cr}$, λ and μ are incremental displacement vector, incremental plastic strain tensor, incremental creep strain tensor, Lamé's first parameter and Lamé's second parameter (shear modulus), respectively. In order to solve Eq.(3.9), the equation is split into implicit and explicit parts as follows:

$$\underbrace{\nabla \cdot [(2\mu + \lambda)\nabla(d\mathrm{u})]}_{\text{implicit}} = \underbrace{\begin{aligned}&-\nabla \cdot \left\{\mu[\nabla(d\mathrm{u})]^T + \lambda\mathrm{Itr}[\nabla(d\mathrm{u})] - (\mu + \lambda)\nabla(d\mathrm{u})\right\}\\&+\nabla \cdot [2\mu(d\varepsilon_p) + \lambda\mathrm{Itr}(d\varepsilon_p)]\\&+\nabla \cdot [2\mu(d\varepsilon_{cr}) + \lambda\mathrm{Itr}(d\varepsilon_{cr})]\end{aligned}}_{\text{explicit}} \tag{3.10}$$
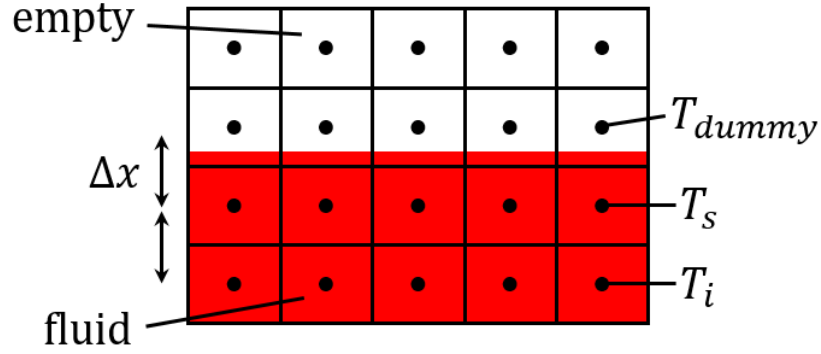
Figure 3.3: Boundary at the melt surface

3.2.3 Melt surface boundary condition

During a severe accident, the amount of melt in the lower head is not constant but variable against accident sequence due to the relocation of molten material into the lower head. The geometry of the molten pool changes according to vessel deformation. In order to be able to treat these effects, a special treatment at boundaries needed to be performed. At the melt surface, convective and radiation heat transfer are considered i.e. heat flux at the both sides of the boundary should be equal:

$$k\frac{(T_i - T_s)}{\Delta x} = h_c(T_s - T_{amb}) + e\sigma_{sb}(T_s^4 - T_{amb}^4) \tag{3.11}$$

where T_i, T_s and T_{amb} are inner cell temperature, surface cell temperature and ambient temperature, respectively. In addition, Δx, k, h, e and σ_{sb} are distance between cell centers, thermal conductivity, heat transfer coefficient, emissivity and Stefan-Boltzmann constant, respectively. Assuming that the amount of melt is smaller than the calculation domain, the melt surface exists inside of the calculation domain and its boundary cannot be given as a boundary of the calculation domain. Since the whole domain should be calculated at a time, a dummy temperature is introduced in the cells above the melt surface such that the heat transfer at the surface should be maintained and can be expressed by heat conduction:

$$k\frac{(T_s - T_{dummy})}{\Delta x} = h_c(T_s - T_{amb}) + e\sigma_{sb}(T_s^4 - T_{amb}^4) \tag{3.12}$$

3.3 Coupling of RELAP/SCDAPSIM and PECM/S

Although RELAP/SCDAPSIM (R/S) is a well-validated reactor analysis code, it has a simple structural analysis model based on Larson-Millar creep model. As shown in Section 4.2, the developed solver, PECM/S, has a capability to simulate the detailed RPV lower head behavior. However, the boundary conditions should be defined manually and the application of standalone PECM/S to the reactor analysis is limited. In order to utilize the strength of each code/solver, coupling of RELAP/SCDAPSIM and PECM/S is necessary.

There are several possibilities to realize a coupled analysis: (1) combining the reactor analysis code and the developed solver, (2) file-based data exchange, and (3) using coupling interface. Since only one executable is used in the first option, the calculation might be the fastest. However, the development effort is high. Although the parameters can be exchanged by files, treatment of data files might be complex and, moreover, the calculation time will be longer due to input/output of the data at each coupling time. Considering the developmental effort and the calculation time, a coupling interface, OpenMPI [83] is used in this study. OpenMPI is a Message Passing Interface (MPI) library and could be used for parallel calculation and coupling of solvers.

In order to utilize the parallel run and information exchange through OpenMPI, several MPI functions are needed to be used in the codes for initialization, finalization of the calculation, and sending and receiving message (Fig. 3.4). The functions `MPI_Init`, `MPI_Comm_rank`, `MPI_Comm_size` and `MPI_Finalize` are called only once in the calculation in each code for initialization: `MPI_Int` initialize MPI execution environment; `MPI_Comm_rank` and `MPI_Comm_size` determine the rank of the calling process in the communicator and the size of the group associated with a communicator, respectively; and `MPI_Finalize` terminates MPI execution environment. By the command `mpirun`, RELAP/SCDAPSIM and PECM/S implemented in OpenFOAM will be started in parallel. Two codes run parallel during the calculation and the information of parameters is exchanged at every coupling time step by using the MPI functions: `MPI_Send` and `MPI_Recv`. Thermal hydraulics and core behavior are calculated in RELAP/SCDAPSIM. Once the molten material relocates into the lower head, the heat transfer and structural behavior in the lower head was originally calculated by COUPLE module included in RELAP/SCDAPSIM. In my coupled analysis using OpenMPI, this part is replaced by PECM/S. Since smaller time steps are needed in RELAP/SCDAPSIM, the coupling is not performed at every time step in order to reduce calculation time. The main parameters to be exchanged are listed in Table 3.6 .
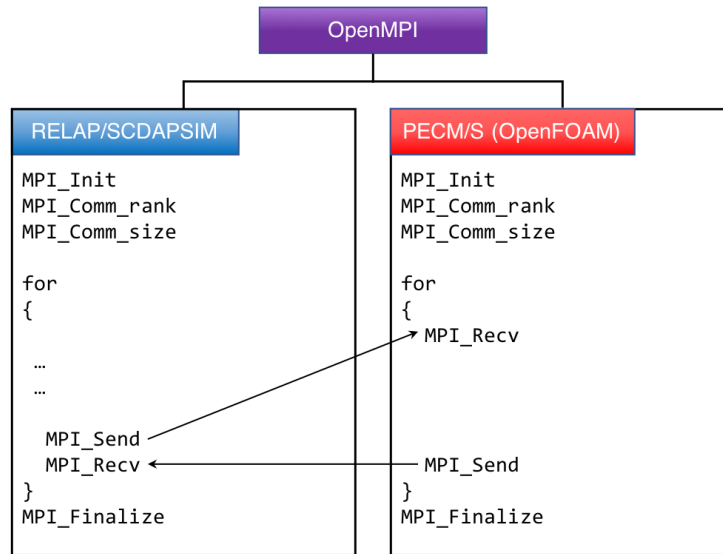
Figure 3.4: Execution of coupled analysis system

Table 3.6: Parameters exchanged between RELAP/SCDAPSIM and OpenFOAM

General initial parameters	
RELAP/SCDAPSIM → OpenFOAM	OpenFOAM → RELAP/SCDAPSIM
Initial melt weight	Coordinate of vessel
Initial melt temperature	
Type of melt	
Run-time parameters	
RELAP/SCDAPSIM → OpenFOAM	OpenFOAM → RELAP/SCDAPSIM
Current time	Wall temperature
Current time step	Heat transfered to RELAP volumes
Slumped mass	
Material properties of melt	
Pressure	
Fluid temperature	
Heat transfer coefficient	

4 Assessment and Validation

In this chapter, the assessment and validation of different codes are presented. Table 4.1 shows the assessment and validation matrix and the list of experiments along with the phenomena investigated. Section 4.1 will describe assessment and validation of the COUPLE module implemented in RELAP/SCDAPSIM. In order to evaluate the module against two tests using different melt surface cooling conditions, LIVE-L1 and -L7V will be numerically analyzed. Main focuses will be the molten pool heat transfer, crust formation along the inner vessel wall and the vessel wall temperature profile. The corresponding parameters predicted by the code will be compared with the experimental data. In Section 4.2, the validation of PECM/S will be explained. Since the PECM itself has been evaluated against LIVE-L1 test in a previous study [84], LIVE-L7V will be calculated for evaluation purpose. More emphasis will be on the PECM/S, which is the extension of the PECM and includes a structural analysis model. The FOREVER test series, investigating vessel deformation and failure, will be calculated and the results will be discussed. Finally, the coupled system of RELAP/SCDAPSIM-PECM/S will be validated and the results will be presented in Section 4.3. The validation will be performed against the LIVE tests with a homogeneous pool under different cooling conditions (LIVE-L1, -L7V and -L11) as well as a stratified molten pool test (LIVE-L6).

Table 4.1: Assessment and validation matrix and list of experiments

phenomena	Assessment and validation target			Experiments				
	COUPLE	PECM/S	R/S-PECM/S	LIVE-L1	LIVE-L7V	LIVE-L11	LIVE-L6	FOREVER
homogeneous molten pool heat transfer	x	x	x	x	x	x		
stratified molten pool heat transfer			x				x	
crust formation	x	x	x	x	x	x	x	
vessel wall heat transfer / temperature distribution	x	x	x	x	x	x	x	x
vessel deformation and failure		x	x					x
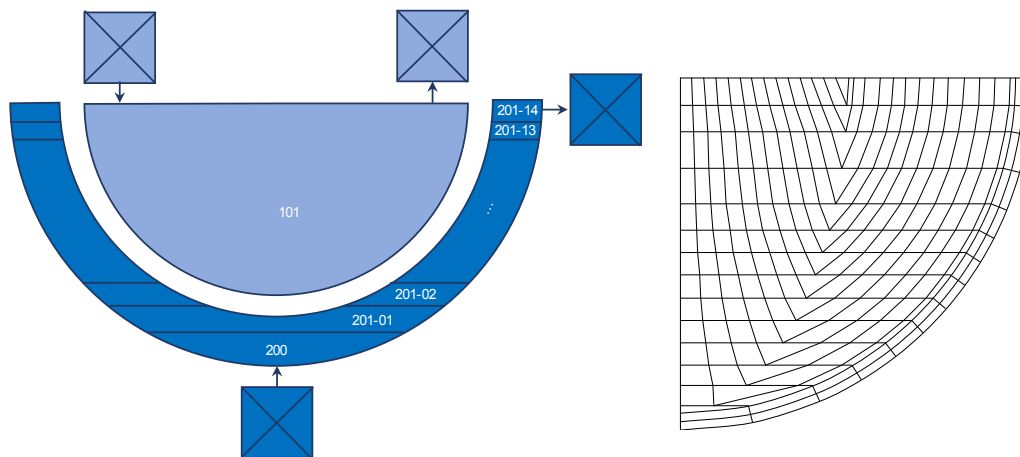
Figure 4.1: RELAP5 and COUPLE nodalizations

4.1 Assessment and improvement of the lower head heat transfer model in RELAP/SCDAPSIM

4.1.1 COUPLE input description

Since only one volume and saturated water condition were assumed for the external vessel in the original model, my modification enabled multiple RELAP5 volumes and any cooling conditions. The thermal hydraulic nodalization scheme and the COUPLE nodes are shown in Fig. 4.1. The external cooling vessel is realized by pipe/annulus components (components 200 and 201) of RELAP5 and the heat structure components are used to represent the outer wall of the cooling vessel. A single volume (component 101) is used for the lower plenum and two volumes are attached to it for the water/air inlet and outlet, respectively. The heat transfer of molten pool and the vessel wall is calculated by the COUPLE module, which has a two-dimension axisymmetric mesh as shown in Fig. 4.1 (right). The nodes representing the lower head volume where molten materials exist are connected with the corresponding RELAP5 volume (component 101) and the nodes representing the external vessel wall are connected with the ex-vessel hydrodynamic volumes (components 200 and 201). The convective boundaries between simulant melt and coolant and between vessel wall and external volume are calculated by heat structure package used in RELAP5. The ex-vessel hydrodynamic volumes (components 200 and 201) are modeled by vertical pipe/annular components and the vessel wall is assumed to be vertically connected on the side of the volumes.

4.1.2 LIVE-L7V analysis

Initial calculation

Although the COUPLE module was validated against the simple experiments in the developmental phase, few evaluation studies have been performed against the hemispherical molten pool experiments recently conducted due to the high interest of external reactor vessel cooling.
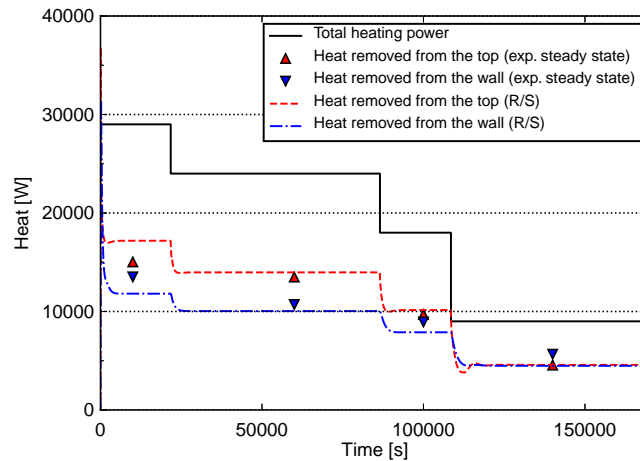
Figure 4.2: LIVE-L7V: comparison of removed heat from the melt surface cooling lid and the external wall

As a first step, the LIVE-L7V test has been analyzed. Fig. 4.2 shows the comparison of the removed heat from the melt surface and from the external vessel wall. For the experimental data, the steady-state values are shown in the figure. Although a discrepancy can be seen at the heating power of 29 kW, the calculated results show good agreement with the experimental data. The calculated molten pool temperature is compared with the measured values in Fig. 4.3. The temperatures at three thermocouples are displayed: MT1, MT9 and MT21, positions of which are shown in Fig. 2.1. Since the uniform temperature is expected in the COUPLE model due to a high effective thermal conductivity, only one value is given for the simulation result. The calculated value was higher than the temperature at MT21 where maximum temperature is expected. This result is consistent with the assessment work using a CFD code presented in the appendix of the code manual [74]. The temperature predicted by COUPLE was higher than the one predicted by the CFD code that models in detail the hydrodynamic behavior of the molten material and the heat transfer from the molten material to the external surface of the lower head. Fig. 4.4 shows the heat flux along the vessel wall. The calculated heat flux profile was rather flat compared to the measured values and the maximum heat flux was underestimated. In a real-scale severe accident analysis, the critical heat flux is one of the important parameter to know whether the cooling capability is sufficient. The underestimation of the maximum heat flux lead to overestimation of cooling capability, which might overlook a possible vessel rupture.

Comparison of heat transfer correlations

In this section, the calculation results with different heat transfer coefficients will be compared. Different Nu–Ra_i correlations induce different fractions of heat removed from the melt surface and from the side wall. Fig. 4.5 shows the comparison of removed heat from the melt surface with the different heat transfer correlations. A discrepancy of approximately 2500 W could be seen in the first plateau with the COUPLE default correlation, while the ACOPO and the UCLA correlations have given better agreement with the experiment. Through the four steady-states in the experiment, reasonable results were obtained by using the ACOPO and the UCLA correlations. In Fig. 4.6, the molten pool temperature is shown. Both the ACOPO and
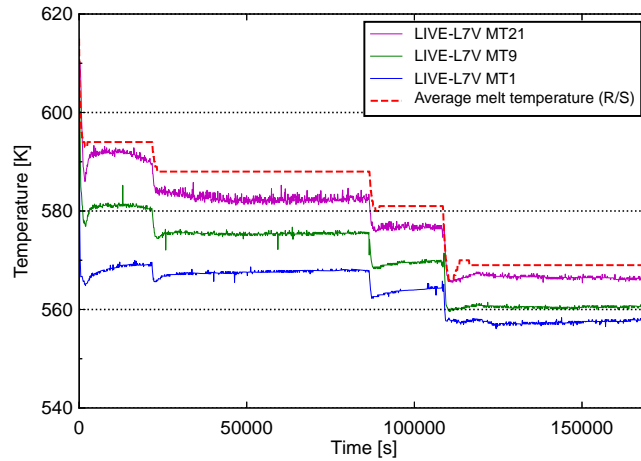
Figure 4.3: LIVE-L7V: comparison of molten pool temperature
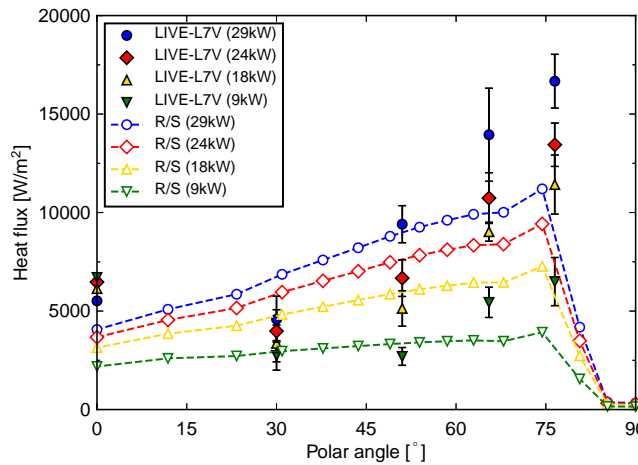
Figure 4.4: LIVE-L7V: heat flux profile along vessel wall obtained with original COUPLE model

UCLA correlations predicted the temperature lower than the COUPLE default correlation and were between MT1 and MT21, which indicates that the average molten pool temperature is reasonably predicted.

The heat flux profile along the vessel inner wall with different correlations is compared in Fig. 4.7. The difference between the COUPLE and the ACOPO correlations become significant at the higher vessel region, whereas they give similar profile at the lower half. The maximum heat flux is better predicted by the ACOPO correlation. Although the maximum heat flux by the UCLA correlation gives also reasonable value, the results from the UCLA correlation show different trend compared to the measured data and give much higher heat flux at the lower half of the vessel, which result in the thinner crust prediction in this region unlike other two correlations. At the lower position, the ACOPO correlation gives better agreement with the experiment, though it slightly overestimated around the polar angle of 30°.

Fig. 4.8 shows the crust thickness along the inner vessel wall. The thermocouple trees are installed at the inner wall at the polar angles of 4.6, 37, 51 and 67°. Each thermocouple tree consists of four to nine thermocouples arranged parallel to the vessel wall. The distance between each thermocouple is 3–10 mm depending on the positions. It should be noted that the maximum length of the thermocouple tree at the polar angle of 4.6° was 30 mm and that whole thermocouple tree was inside the crust through the experiment. Thus, the crust thickness at this position was more than 30 mm, although it could not be measured. The COUPLE default correlation and the ACOPO correlation give a similar curve except for the higher vessel region. The thickness is thinner at the lower region with the UCLA correlation, which led to higher heat flux profile in this region. Comparing the three correlations, all the correlations give a similar trend that the thickness is overestimated in the higher position. Since the number of crust thickness measurement positions is limited, the thickness cannot be compared in the lower vessel region. According to the fact that the thermocouple tree at the polar angle of 4.6°, whose length is 30 mm, was inside the crust, it can be assumed that the calculated crust thickness was underestimated at the lower vessel region.

Due to lower heat transfer in the crust, the crust thickness and the vessel wall temperatures have a strong relation with each other. As can be seen in Fig. 4.9, the inner and outer vessel wall temperatures are overestimated with all correlations and the discrepancy was the largest at the polar angle of 30°. A possible reason is that the calculated crust thickness at the lower vessel region was thinner than the experimental one, which led to larger heat transfer from the pool to the cooling water. Since larger amount of heat is transferred to the external cooling water at the lower vessel region, the predicted water temperature is higher than the experiment. As a result, the calculated vessel wall temperature was overestimated.

Considering the discussion above, the ACOPO correlation gives the most reasonable results among three correlations in heat flux and heat balance. Therefore, the ACOPO correlation is recommended to be used.
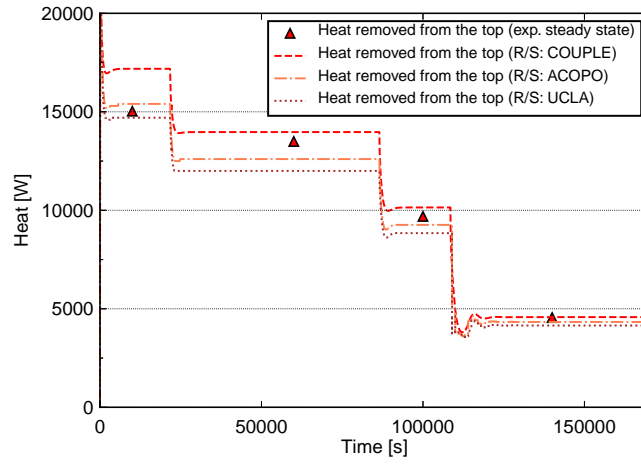
Figure 4.5: LIVE-L7V: removed heat from the melt surface with different heat transfer correlations
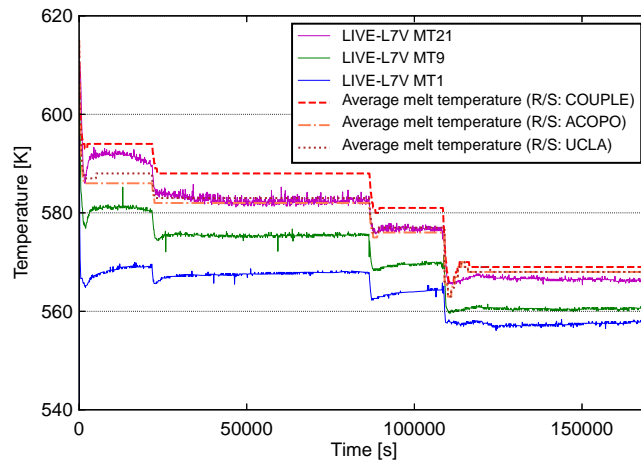
Figure 4.6: LIVE-L7V: molten pool temperature with different heat transfer correlations
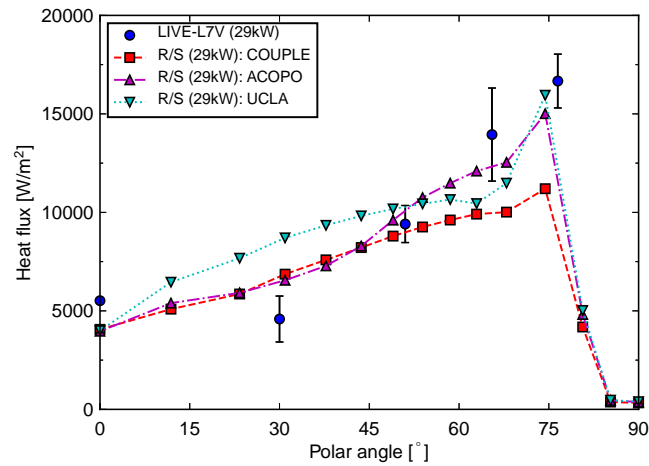
Figure 4.7: LIVE-L7V: heat flux profile along the vessel wall at power of 29kW
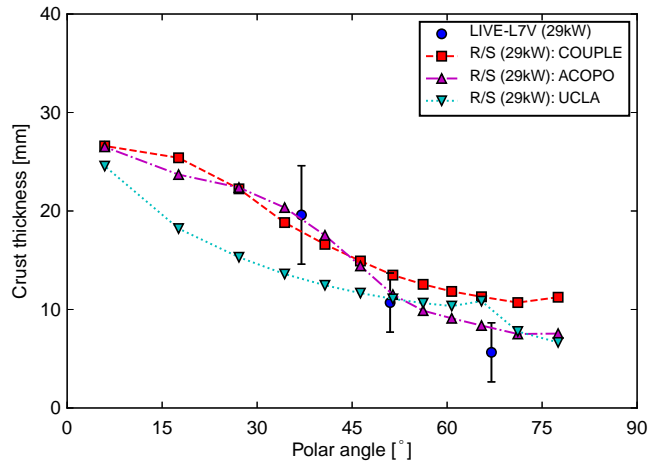
Figure 4.8: LIVE-L7V: crust thickness along the inner vessel wall at power of 29kW
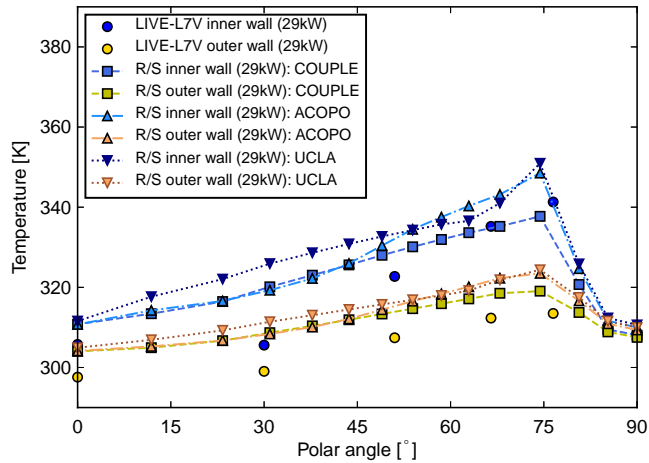
Figure 4.9: LIVE-L7V: inner and outer wall temperature at power of 29kW

4.1.3 LIVE-L1 analysis

Calculation results in steady-state

In order to evaluate the model with a different cooling condition, the LIVE-L1 test was analyzed for this dissertation. Considering the results of the LIVE-L7V analysis, the ACOPO correlation was used. The heat flux along the vessel wall is compared in Fig. 4.10. The maximum heat flux at heating power of 7 kW agrees well with the measured data, while it is slightly underestimated at 10 kW. On the other hand, the heat flux is overestimated in the middle of the vessel in both heating plateaus. In a post-test analysis, the crust thicknesses at three positions (polar angles of 41.4, 52 and 62°) were measured in order to investigate crust formation during each heating power. Additionally, the crust thickness was measured at the end of the test all along two meridians, which are denoted as SW and NE in Fig. 4.11. In the experiment, the area between liquidus and solidus temperature was a thin mushy region where the composition of each phase changes locally and the crust front was assumed to exist between these temperatures.
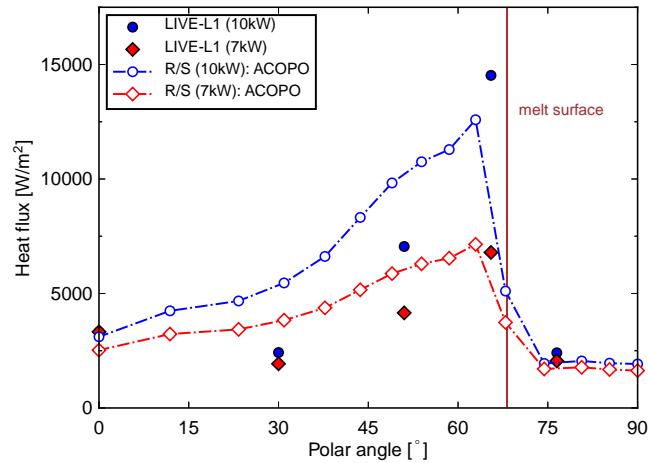
Figure 4.10: LIVE-L1: heat flux profile along the vessel wall

On the other hand, in the calculation a mushy zone is considered in the energy equation including the latent heat, and the position whose temperature is the liquidus temperature is regarded as the crust front, so that a maximum crust thickness is predicted. Nevertheless, as can be seen from the figure, the crust thickness is underestimated all along the inner vessel wall and the discrepancy is larger in the lower region. One of the reasons that the heat flux is overestimated in the middle of vessel would be that the crust thickness is underestimated all along the vessel wall (Fig. 4.11). The thinner the crust thickness is predicted, the larger the temperature gradient between the molten pool and the wall becomes, which leads to higher heat flux. Another reason would be the effect of non-uniform heating in the experiment and the heat generation at the bottom of the vessel, while a homogeneous heating is assumed in the calculation. Since the heating was performed by six heating planes in LIVE-L1 and the temperature was locally higher where the heating planes were installed, less crust formation has taken place at those positions comparing to other regions. The corresponding polar angles, where the heating planes were installed, are 12, 30, 47, 54 and 60°. As shown in Fig. 4.11, the crust thickness profile has a local minimum at those positions, which indicates the local non-uniform heating and crust formation.

The vessel wall temperature agrees well in the middle of the vessel, while it is underestimated around the melt surface (Fig. 4.12). In the COUPLE module, more crust is tended to be formed at the very top corner of the molten pool near the vessel wall. Due to thicker crust at the molten pool corner, the heat flux and temperature at the very top of the melt are underestimated. Therefore, further investigation in the crust formation model should be conducted in the future.
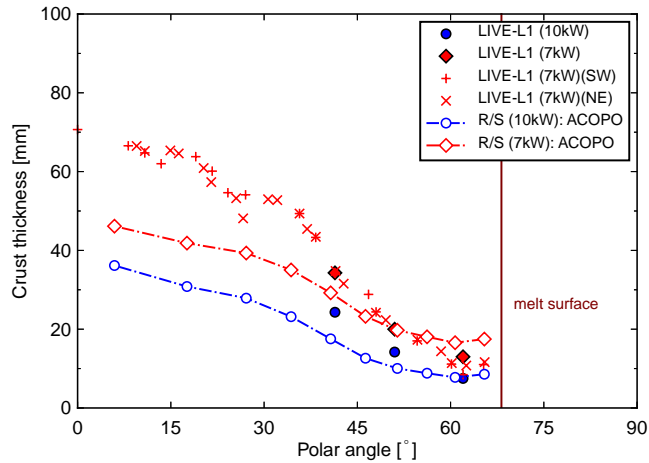
Figure 4.11: LIVE-L1: crust thickness along the inner vessel
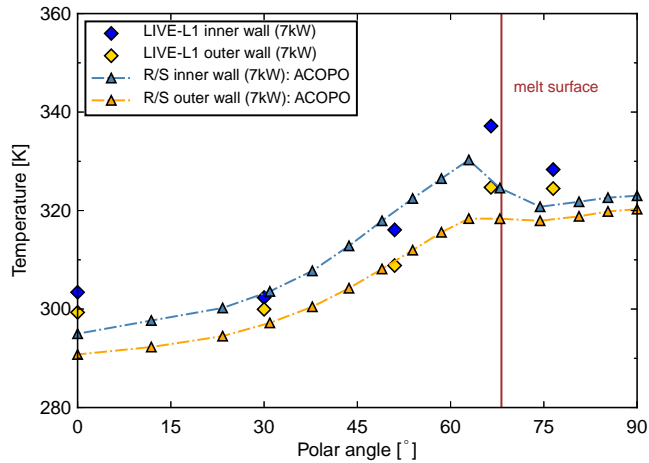
Figure 4.12: LIVE-L1: inner and outer wall temperature at 7kW

Transient calculation before external cooling initiation

Before the water injection at 7200 s, the cooling vessel was filled with air and a weak natural convection occurred. The inner wall temperature and the cooling vessel temperature at 6000 s are compared in Fig. 4.13. In order to compare the effect of radiation heat transfer from the test vessel to the cooling vessel, two cases were calculated: with and without consideration of radiation heat transfer between the test vessel wall and the cooling vessel wall.

Although the calculated inner wall temperature has reasonable agreement with the measured data at lower region of the vessel, it is underestimated above the polar angle of 45°. The cooling vessel temperature measured at the experiment has a rather flat profile along the vessel, while the calculated temperature has a curved profile. In reality, radiation heat transfer may occur from any surface to any facing surface. In the model, however, heat transfer from the test vessel to the external cooling volume and to the cooling vessel is considered at the same
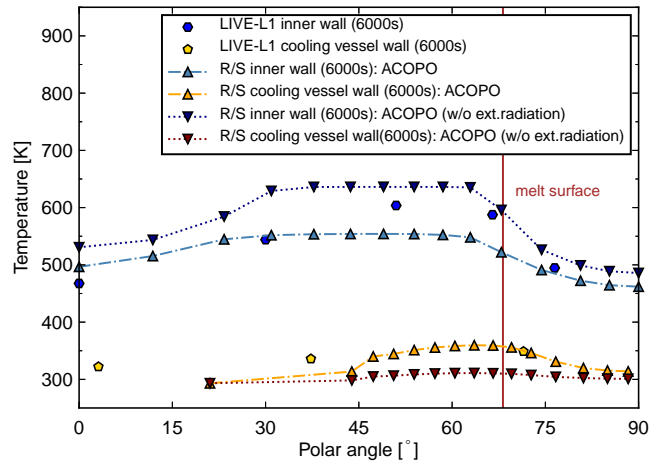
Figure 4.13: LIVE-L1: vessel inner wall temperature during transient phase
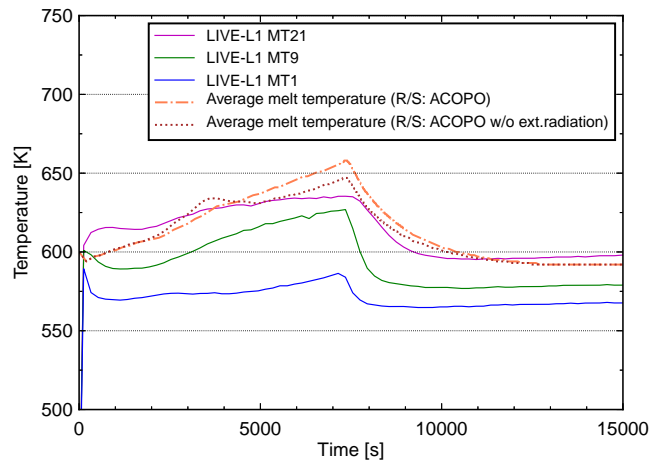
Figure 4.14: LIVE-L1: molten pool temperature during transient phase

elevation, which led to the curved temperature profile of the cooling vessel temperature in comparison to the measured profile. Considering detailed view factors at each surface is needed to improve the radiation heat transfer calculation. Fig. 4.14 shows the molten pool temperature during the air-cooled phase. Since more heat was removed from the external wall in case that radiation heat transfer was considered at the external wall, the molten pool temperature was lower than that of the case without radiation until 4000 s. This led to the formation of the thin crust layer with the thickness of ~1 mm all along the inner vessel wall, while it was not observed in case of no radiation heat transfer at the external wall. Because of this crust, the heat transfer through the vessel wall was limited and much higher molten pool temperature and lower vessel wall temperature were predicted. This indicates that there is a possibility to underestimate the vessel wall temperature during core-melt severe accidents before external cooling is initiated.

4.2 Validation of PECM/S

4.2.1 Thermal analysis

For evaluation of PECM implemented into OpenFOAM, I have compared the prediction against the LIVE-L7V test. As the boundary conditions of the melt surface and of the external vessel, constant heat transfer coefficients were given. The comparisons of the heat flux profile along the vessel wall are shown in Fig. 4.15. The calculated shape of the heat flux agrees very well with the experimental findings. In the experiment, the heat flux through the middle section of the vessel is slightly lower than the one at the vessel bottom, while the calculation shows gradual increase of heat flux along the vessel wall. This can be explained by the effect of non-uniform heating in the experiment and a non-uniform heat generation in the crust at the bottom of the vessel. The predicted wall temperature profile at the heating power of 29 kW reasonably matches with the experimental data (Fig. 4.16). Through a perspective of IVR through external water cooling, heat flux and wall temperature are two important parameters. Therefore, it can be concluded that the PECM has the potential to predict a molten pool behavior in the lower plenum.
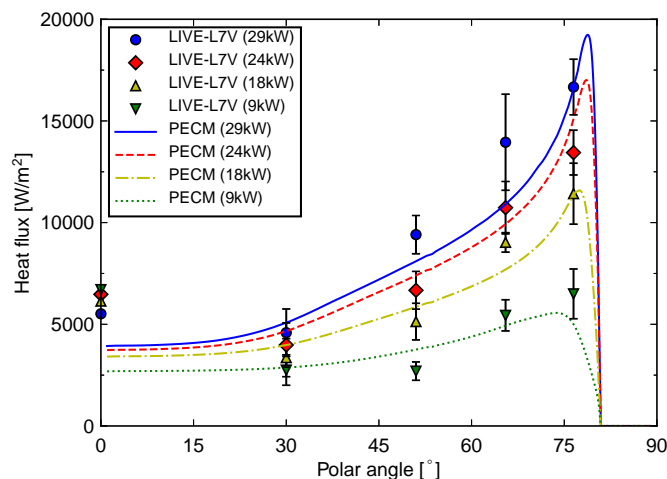
Figure 4.15: Heat flux profile along vessel wall

4.2.2 Thermal structural analysis

EC-FOREVER-2 analysis

As soon as creep deformation occurs due to thermal and mechanical loads, the vessel may experience large displacement. In order to compare the large displacement effect, two calculations have been conducted: one with updated-mesh and one with fixed-mesh. In case of the updated-mesh, the mesh is moved according to the calculated displacement in each time step. The molten pool in the vessel is also moved according to the vessel deformation. Additionally, the emissivity of the melt surface is one of the uncertainties in the experiment and its effect was also compared. Considering calculation effort, an axi-symmetrical mesh was developed
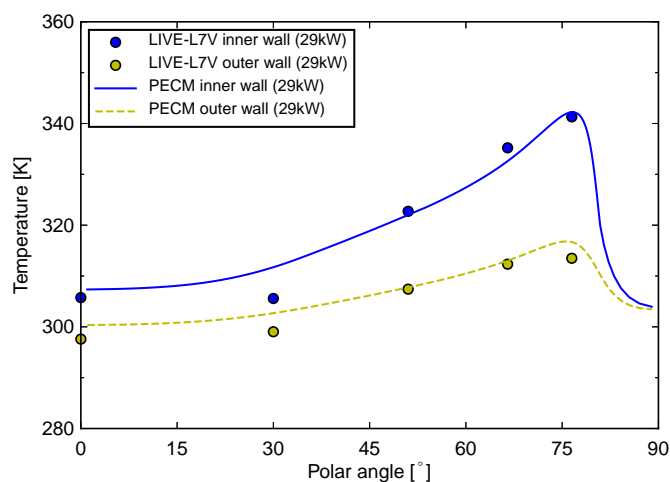
Figure 4.16: Vessel wall temperature profile at heating power of 29kW

(Fig. 4.17). Thermal calculation is conducted by PECM and its results are reflected in the structural analysis. According to the deformation of the vessel, the geometry of the molten pool is changed in case of updated-mesh.

The temperature profile along the external wall at 15500 s is compared in Fig. 4.18. In case that the emissivity of melt surface is 0.5, the updated-mesh gives lower temperature along the vessel compared to the fixed-mesh. This is due to larger heat loss to the environment according to larger vessel surface resulting from thermal expansion of the vessel. The calculated displacement at the vessel bottom, however, differed significantly between the cases (Fig. 4.19) and the difference of the failure time was more than 3 hours. In EC-FOREVER-2 test, the vessel failure occurred from the outside of the vessel and this was qualitatively well demonstrated as shown in Fig. 4.20. The thermal and mechanical load lead to the thickness changes of vessel wall with time and space. The location of the largest thickness change where the vessel failure occurred agrees well with the experiment (Fig. 4.21), which quantitatively shows a capability of the solver to simulate the vessel deformation and failure. Assuming the emissivity of the melt surface being 0.8, the vessel wall temperature was lower than the one with emissivity of 0.5. As shown in Fig. 4.18, the maximal difference was ~50 K at the position where the highest temperature is given. Its effect on the vessel deformation behavior was significant and the failure time differed approximately by 3 hours.

Several different mesh sizes have been compared to investigate mesh sensitivity. Fig. 4.22 shows the failure time against the number of cells along the vessel. The results with different mesh sizes in the direction vertical to the vessel was compared. Although the case with a larger mesh size predicted a later failure time than the finer mesh cases, the difference was within ~5%.
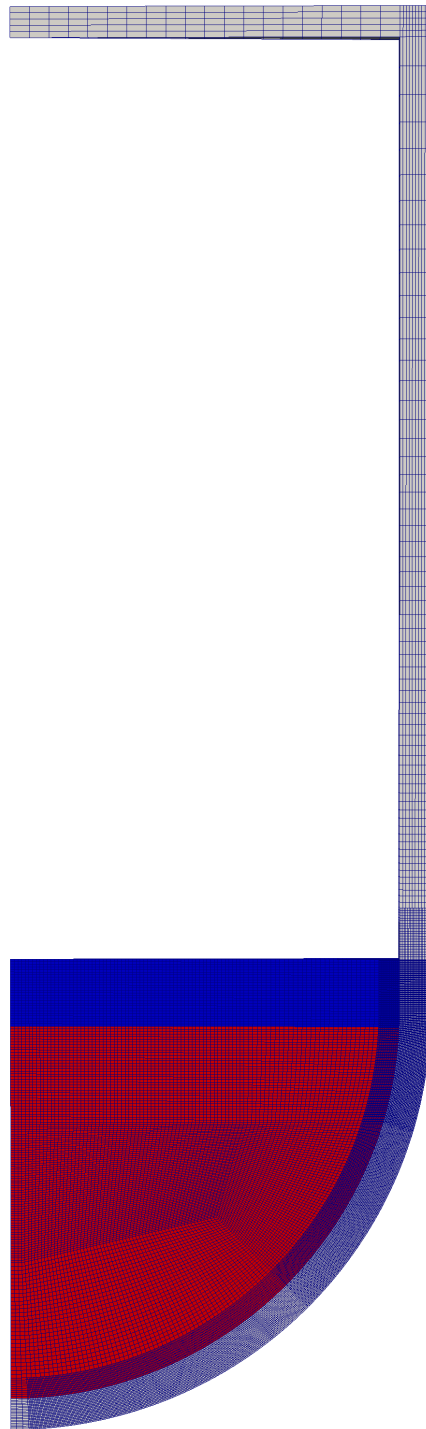
Figure 4.17: FOREVER calculation domain
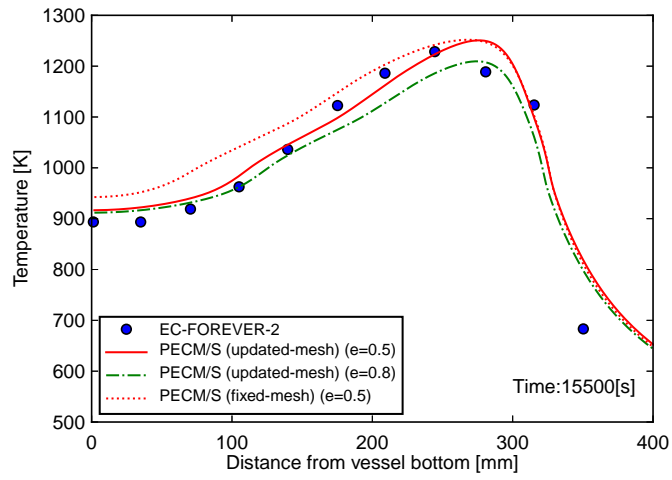
Figure 4.18: EC-FOREVER-2: external vessel wall temperature
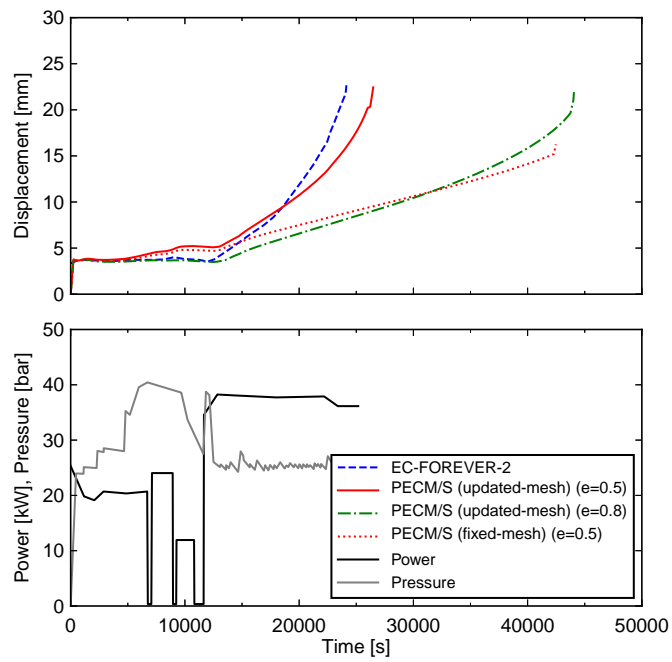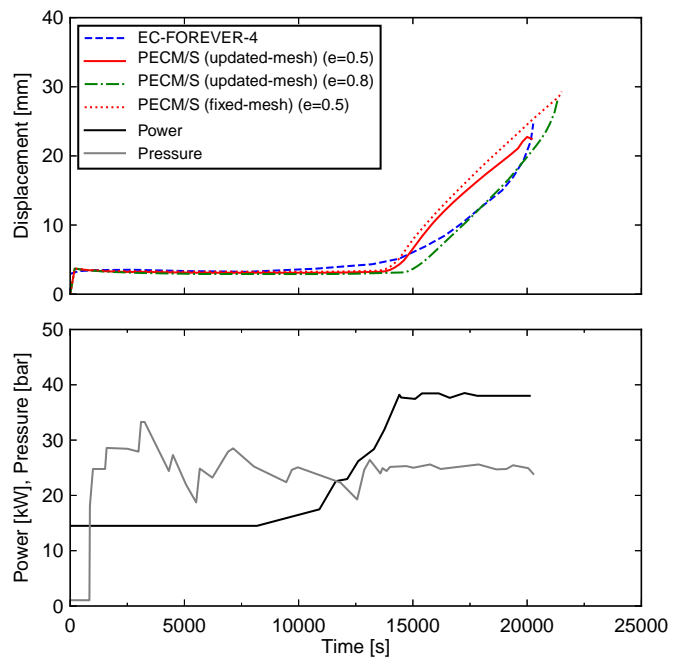

Figure 4.19: EC-FOREVER-2: heating power, pressure and vessel bottom displacement against time at different emissivity
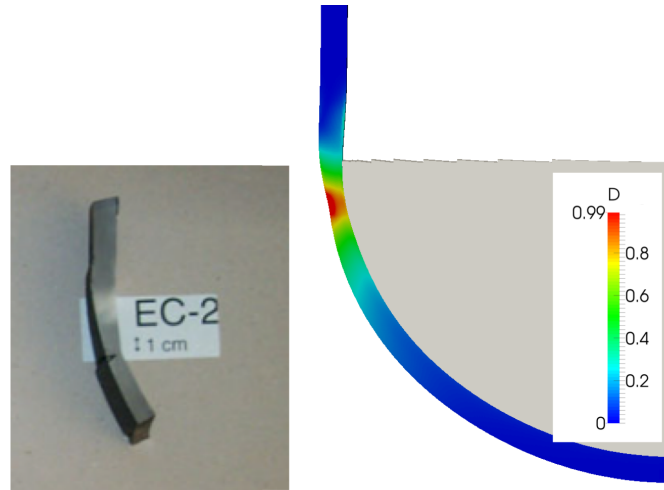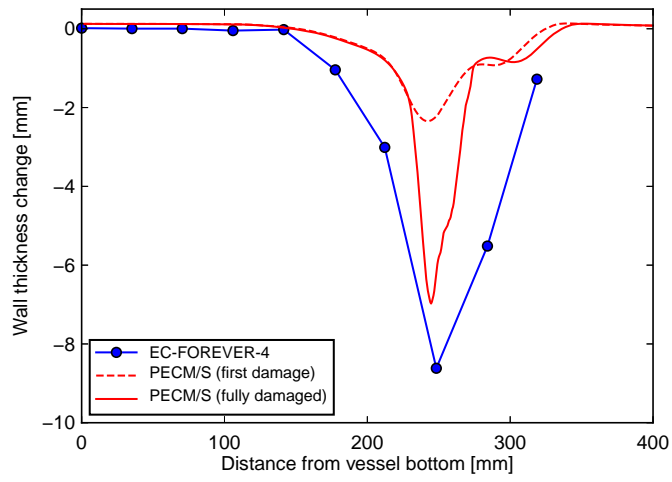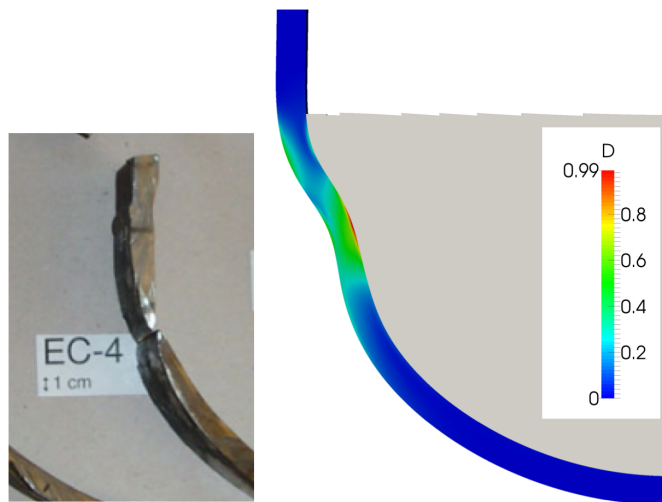
Figure 4.20: EC-FOREVER-2: comparison of vessel failure position [56] along with calculated damage parameter profile
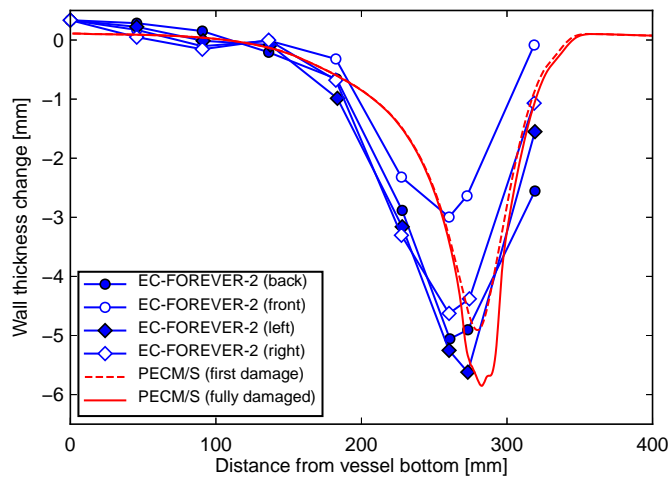
Figure 4.21: EC-FOREVER-2: wall thickness change along the vessel wall

EC-FOREVER-4 analysis

Although the wall temperature profile at 16000 s shows a temperature difference of approximately 50 K among the cases, which is the similar trend as EC-FOREVER-2, the displacement of the vessel bottom and the failure time were not significantly different, as can be seen in Fig. 4.23 and Fig. 4.24. As mentioned in Section 3.2.2 in case of SA533B1 steel, the primary creep was not noticeable. Therefore, the secondary creep, where the creep strain rate is determined by stress and temperature, was immediately initiated and the creep process was not notably different. The wall thickness change at the end of the experiment is compared in Fig. 4.25. The location of vessel failure was where the thinnest wall was observed and the solver was able to predict it reasonably. Unlike EC-FOREVER-2, the vessel behavior was more ductile and the failure star-
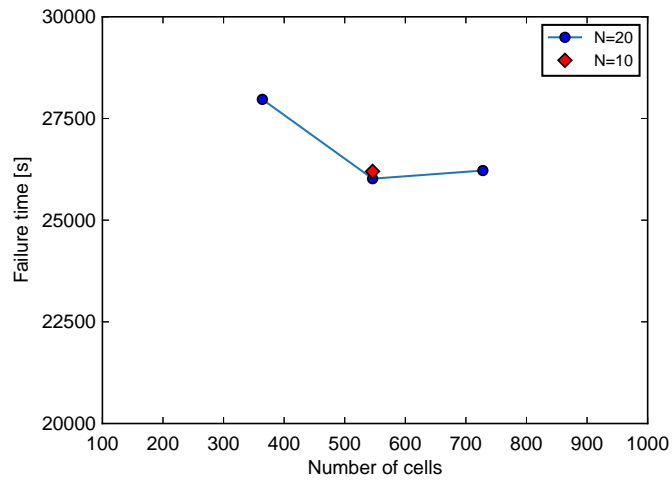
Figure 4.22: EC-FOREVER-2: mesh sensitivity

ted at the inner wall. As shown in Fig. 4.26, the failure mode agrees well with the experiment qualitatively.
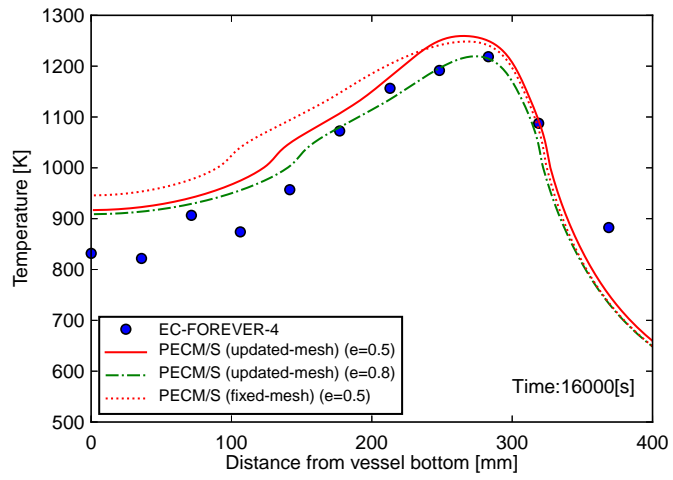
Figure 4.23: EC-FOREVER-4: external vessel wall temperature

Figure 4.24: EC-FOREVER-4: heating power, pressure and vessel bottom displacement against time at different emissivity

Figure 4.25: EC-FOREVER-4: wall thickness change along the vessel wall

Figure 4.26: EC-FOREVER-4: comparison of vessel failure position [56] along with calculated damage parameter profile

4.3 Validation of coupled system

In this section, my validation calculations of the coupled system are shown. The results of the coupled analysis are compared with the experimental data and the RELAP/SCDAPSIM stand-alone calculations. In the figures, the results of the coupled calculation and the RELAP/SCDAPSIM stand-alone calculation are denoted as R/S-PECM/S and R/S, respectively.

4.3.1 LIVE-L1 analysis

The vertical profile of melt pool temperature is shown in Fig. 4.27. The RELAP/SCDAPSIM-PECM/S predicted rather uniform temperature profile compared to the experiment. This is due to the modeling assumptions in PECM, where ideal turbulent mixing of the molten pool material is assumed. In reality, however, for a low Prandtl number, the cold liquid is more accumulated in the lower region due to descending flow from the boundary layer [85]. The heat flux profile along the vessel wall is compared in Fig. 4.28. The heat flux is calculated according to the temperature difference between the inner wall and outer wall. The heat flux calculated by RELAP/SCDAPSIM-PECM/S was smaller than that of RELAP/SCDAPSIM in the lower vessel region and closer to the experimental data. The location and the value of maximum heat flux was well predicted.

In a post test analysis, the crust thickness at three positions (polar angles of 41.4°, 52° and 62°) were measured to investigate crust formation during each heating power. Additionally, the crust thickness was measured at the end of the test all long two meridians, which are denoted as SW and NE in Fig. 4.29. In the experiment, the area between liquidus and solidus temperature was a thin mushy region where the composition of each phase changed locally and the crust front was assumed to exist between these temperature regions. On the other hand, in the calculation, a mushy zone is considered in the energy equation including the latent heat. The position, temperature of which is the liquidus temperature, is regarded as the crust front, such that a maximum crust thickness is predicted. The predicted crust thickness has a good agreement with the experiment at the higher part of the vessel. At the lower region, however, it is approximately 30% overestimated. One possible reason is the effect of non-uniform heating in the experiment at the vessel bottom, which prevented formation of the crust. Since the temperature was locally higher near the heater, less crust formation took place at those positions compared to other regions. The positions, where the heating planes were installed, are the polar angles of 12°, 30°, 47°, 54° and 60°. As can be seen in Fig. 4.29, the crust thickness profile has a local minimum at those positions, which indicates the local non-uniform heating and crust formation. The inner and outer wall temperatures are shown Fig. 4.30 and Fig. 4.31. Compared to the RELAP/SCDAPSIM stand-alone calculation, the RELAP/SCDAPSIM-PECM better predicted the maximum inner wall temperature at both heating power levels.

Before the water injection to the cooling vessel was initiated at 7200 s, the test vessel was cooled by a weak natural circulation of the air. In this transient phase, the flat melt

temperature was predicted similar to the steady state and the difference between the maximum experimental temperature and the predicted temperature was approximately 30 K at 6000 s (Fig. 4.32). Fig. 4.33 shows the outer wall temperatures at 1000 s and 6000 s. Since the thin crust layer was predicted by RELAP/SCDAPSIM-PECM/S at the early stage of the transient phase, the outer wall temperature was underestimated. At 6000 s, the crust was predicted only at the very bottom of the vessel (from 0° up to 30°) and the outer vessel wall temperature at the higher vessel region reached up to 580 K. According to the experimental temperature profile, it can be assumed that the same behavior should have happened in the experiment.
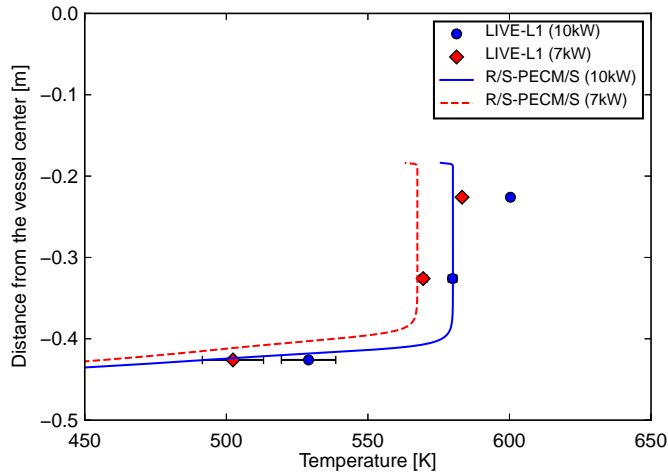
Figure 4.27: LIVE-L1: melt pool temperature profile at a radius of 0.174m
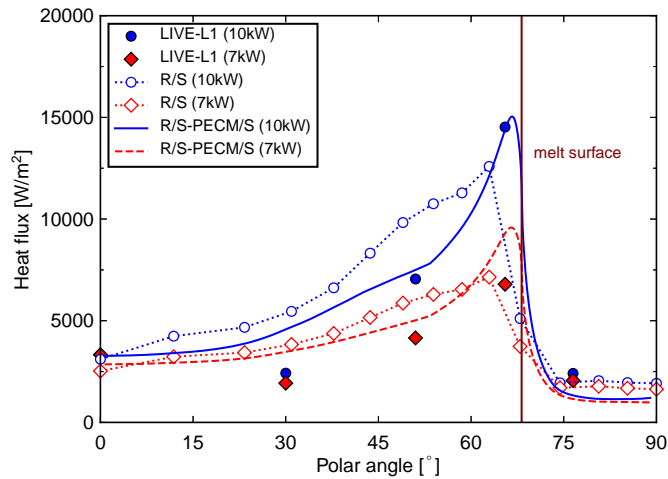
Figure 4.28: LIVE-L1: heat flux profile along vessel wall
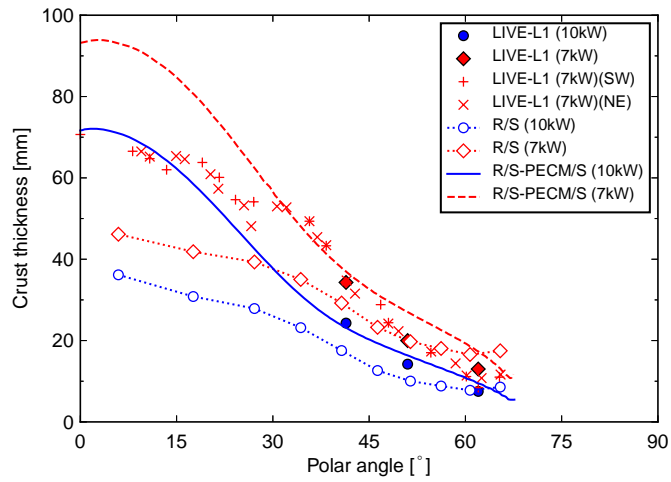
Figure 4.29: LIVE-L1: crust thickness profile along vessel wall
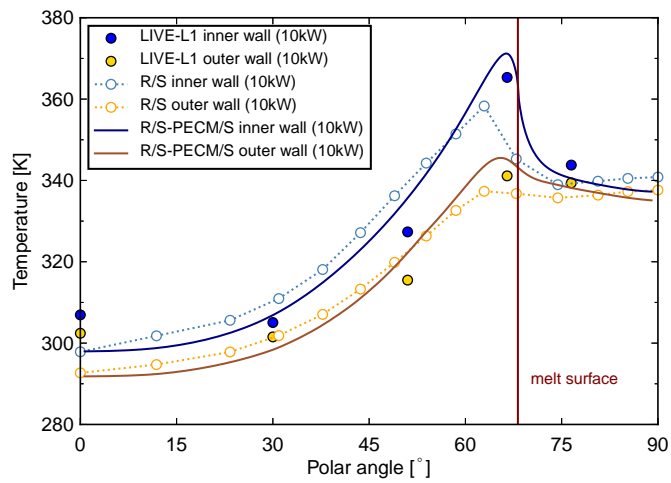
Figure 4.30: LIVE-L1: vessel wall temperature profile (10kW)
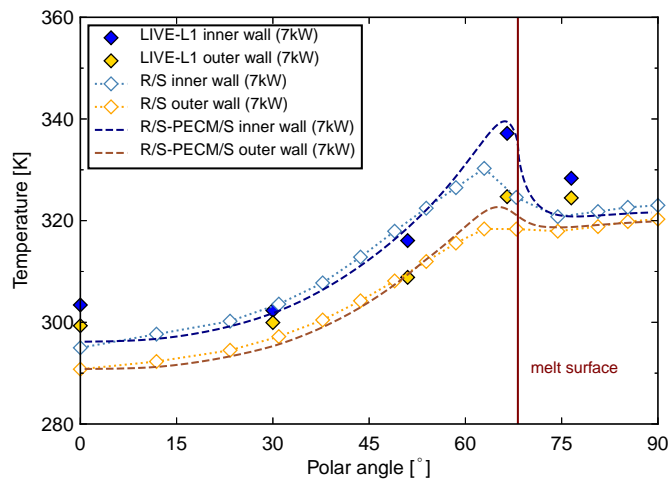
Figure 4.31: LIVE-L1: vessel wall temperature profile (7kW)
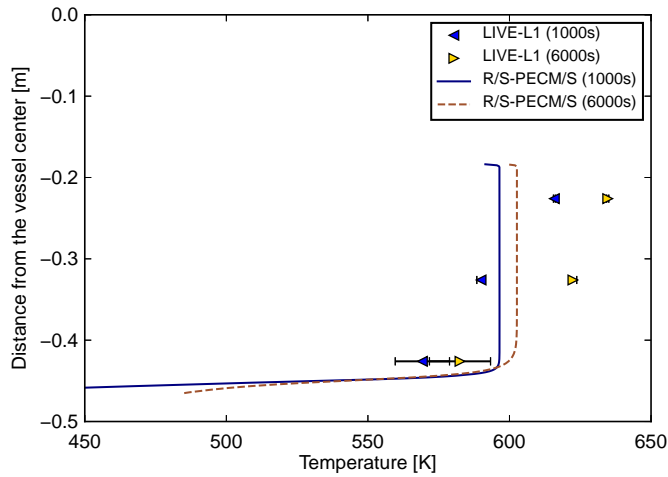
Figure 4.32: LIVE-L1: melt pool temperature profile at the radius of 0.174m (transient)
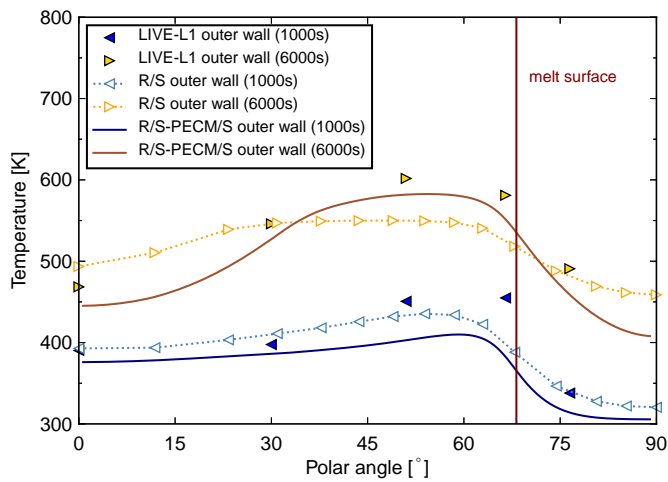
Figure 4.33: LIVE-L1: vessel wall temperature profile (transient)

4.3.2 LIVE-L7V analysis

In the LIVE-L7V test, the upper cooling lid was installed at the top of the vessel. Unlike other experiments, the cooling of the melt is performed not only from the external vessel wall but also from the melt surface. Since both surfaces were cooled by the cooling water with fixed inlet temperature, the amount of heat removed from each surface can be obtained by measuring outlet temperature. Fig. 4.34 shows the removed heat from the top surface and from the external wall in each heating plateau. As can be seen from the figure, the RELAP/SCDAPSIM-PECM/S predicted more heat transfer from the melt to the upper surface as the heating power increases. Especially at the the heating power of 29 kW, the difference between the predicted and measured values was more than 15%, which led to the underestimation of the heat flux profile along vessel wall (Fig. 4.35). At the heating power of 18 kW, both the heat balance and heat flux agreed with the experiment. The vessel wall temperature was well predicted in both cases as shown

in Fig. 4.36 and Fig. 4.37. More investigation might be needed in case of top cooling condition with higher Rayleigh number.
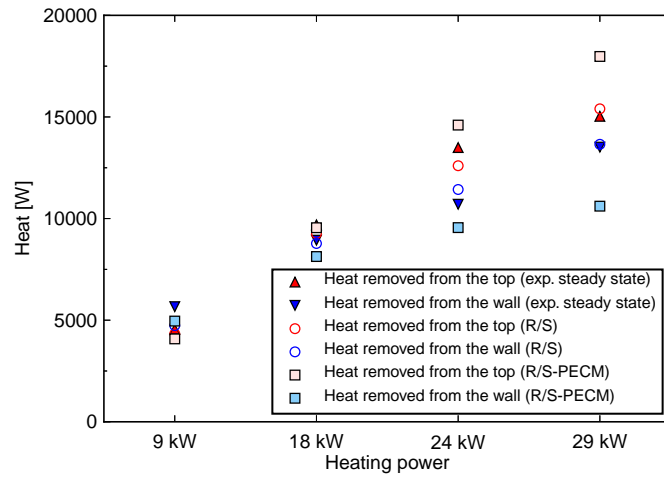
Figure 4.34: LIVE-L7V: heat balance
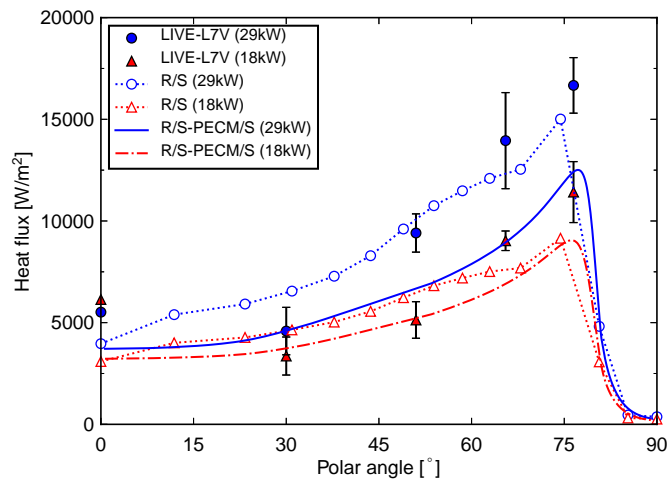
Figure 4.35: LIVE-L7V: heat flux profile along vessel wall at the heating power of 29 kW and 18 kW
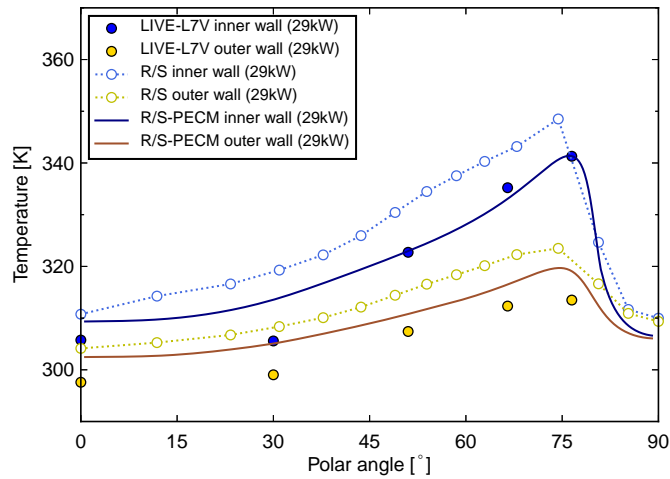
Figure 4.36: LIVE-L7V: vessel wall temperature profile (29 kW)
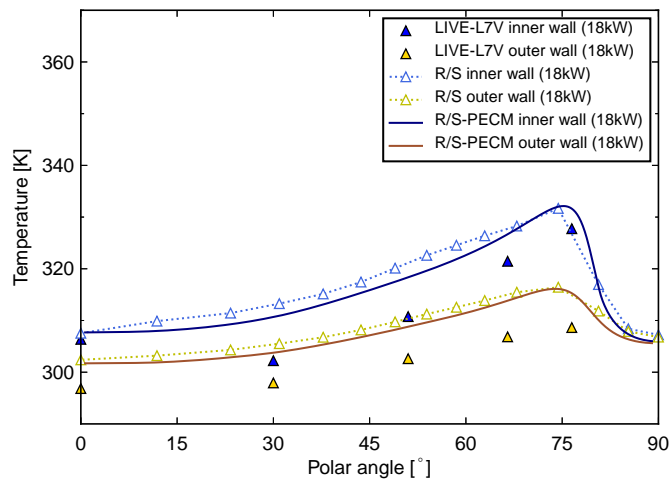
Figure 4.37: LIVE-L7V: vessel wall temperature profile (18 kW)

4.3.3 LIVE-L11 analysis

One of the features of the LIVE-L11 test was the external cooling condition. Unlike the other experiment, only a small amount of water was injected to compensate the evaporation of cooling water and the test vessel was cooled by the boiling water through the experiment. The insulation lid was installed at the top of the vessel and thus the melt surface was weakly cooled by radiation and convective heat transfer. With this cooling condition, a temperature stratification was observed again in the melt pool. As the LIVE-L1 analysis, the RELAP/SCDAPSIM-PECM/S predicted rather uniform temperature profile compared to the experiment (Fig. 4.38). The heat flux profile along the vessel wall is shown in Fig. 4.39. In general, the heat flux is well predicted by RELAP/SCDAPSIM-PECM/S compared to the RELAP/SCDAPSIM stand-alone calculation. Although the location of the maximum heat flux match with the experiment, it is underestimated. This is due to lower predicted inner wall temperature at the top of melt pool (Fig. 4.40 and

Fig. 4.41). The predicted cooling water temperature at the bottom of the vessel did not reach boiling temperature and remained ~340K. This resulted from the underestimation of the inner and outer wall temperatures at the lower region of the vessel. The crust thickness along the inner vessel wall at the final heating plateau with heating power of 21 kW is shown in Fig. 4.42. The coupled system has captured the similar trend as the measured values, although it has underestimated in most regions. On the other hand, the stand-alone RELAP/SCDAPSIM could not capture the steep decrease of the thickness between the polar angles of 15° and 45° and had a rather flat profile.
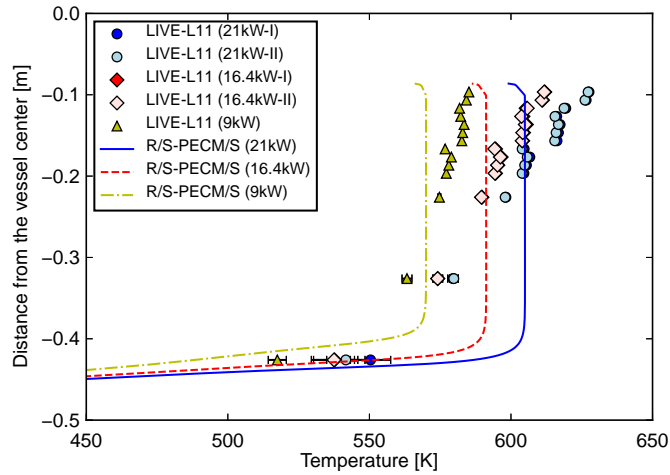
Figure 4.38: LIVE-L11: melt pool temperature profile at the radius of 0.174m
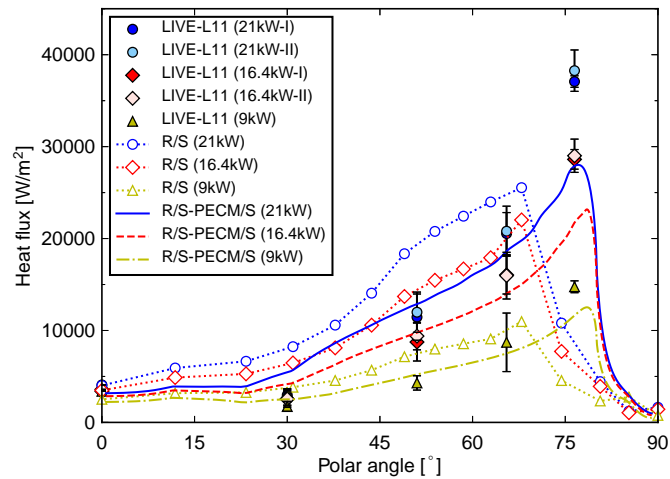
Figure 4.39: LIVE-L11: heat flux profile along vessel wall
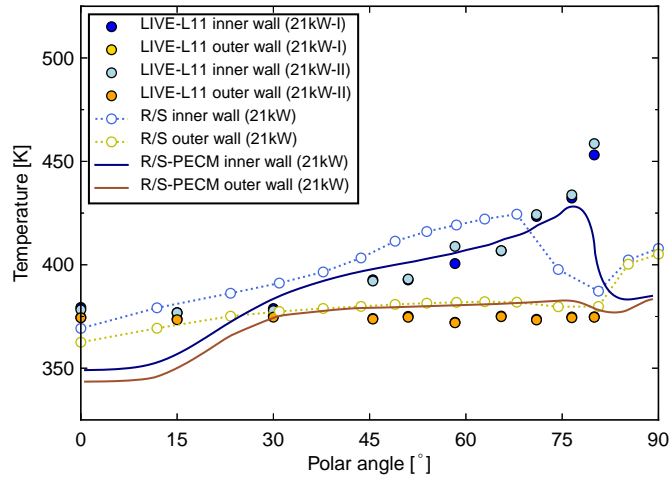
Figure 4.40: LIVE-L11: vessel wall temperature profile (21kW)
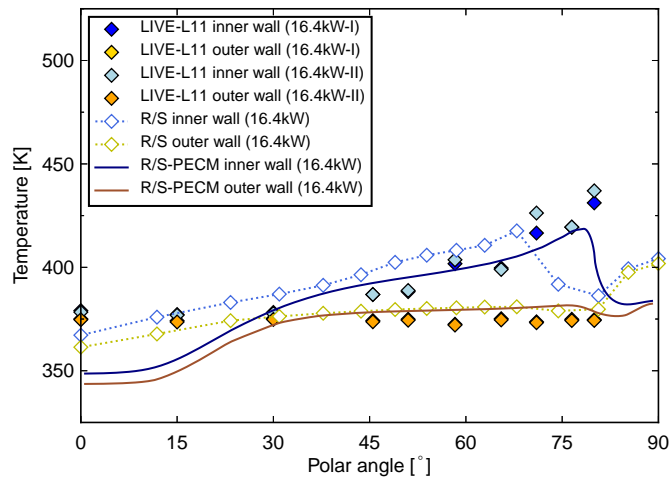
Figure 4.41: LIVE-L11: vessel wall temperature profile (16kW)
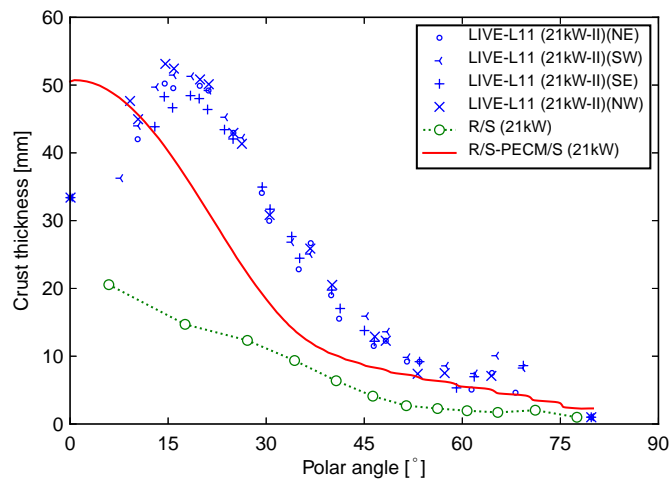
Figure 4.42: LIVE-L11: crust thickness profile along vessel wall (21kW)

4.3.4 LIVE-L6 analysis

In order to validate the capability of simulating a two-layer melt pool, the LIVE-L6 test was analyzed. In the experiment, the melt pool was separated by a copper plate. The lower pool was heated by the heating system with different heating power, while the upper pool was not heated. Fig. 4.43 shows the vertical melt pool temperature. The results of RELAP/SCDAPSIM-PECM were rather flat in both pools compared to the experimental values. In the heated pool, the average temperature is well reproduced, while in the upper pool, the temperature is approximately 20 K underestimated at a heating power of 18 kW, while the difference between the predicted value and the measured value decreases as the heating power being smaller. This indicates that the solver overestimates the natural circulation heat transfer from the melt pool to the cooled side wall. The heat flux profile along the vessel wall is presented in Fig. 4.44. At each power level, the heat flux generally agrees very well with the experiment, although the details of maximum heat flux positions and values are not clear due to the limited number of heat flux measurement points. The inner and outer wall temperatures are overestimated in all the heating levels. The maximum temperature difference is up to 20 K (Fig. 4.45 and Fig. 4.46). The inlet temperature of cooling water was set as 289 K as measured in the experiment. The predicted outlet cooling temperature was 320 K and 305 K with heating power of 18 kW and 10 kW, respectively, whereas in the experiment the temperature was ~295 K. Therefore, one of the reasons of the difference is assumed to be due to the heat transfer from the melt pool to the cooling water. As can be seen in Fig. 4.44, the heat flux is overestimated in the lower vessel region, which indicates higher heat transfer from the melt pool to the cooling water. Another reason would be the crust thickness difference. As presented in Fig. 4.47 .The predicted crust thickness in the lower vessel region is thinner than the measured value. The thinner the crust thickness is, the higher the inner wall temperature due to the conduction in the crust, which leads to the higher outer wall temperature.
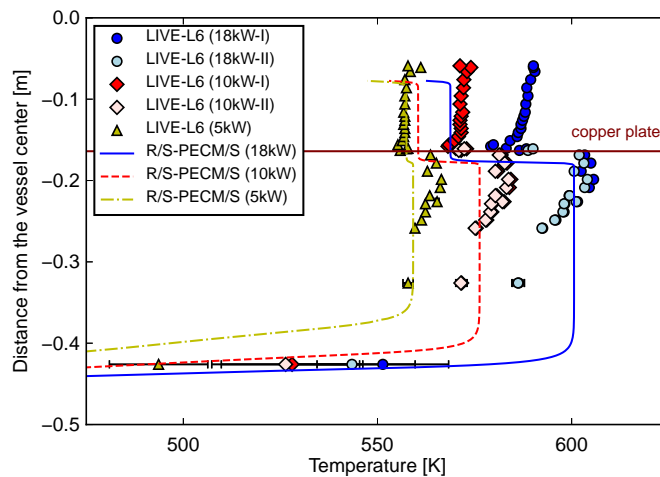

Figure 4.43: LIVE-L6: melt pool temperature profile at the radius of 0.174m
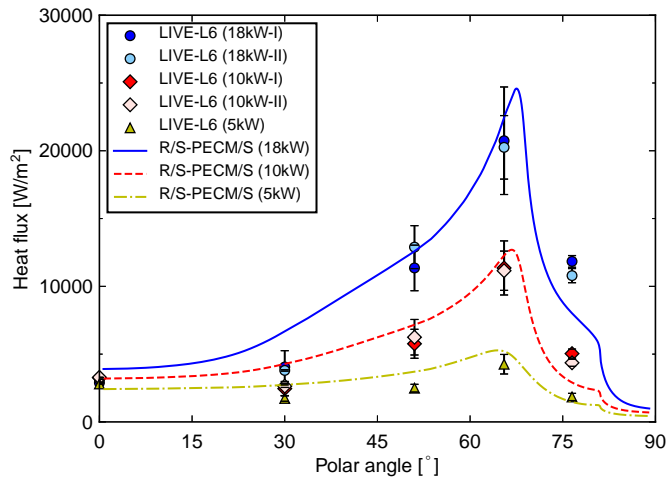
Figure 4.44: LIVE-L6: heat flux profile along vessel wall
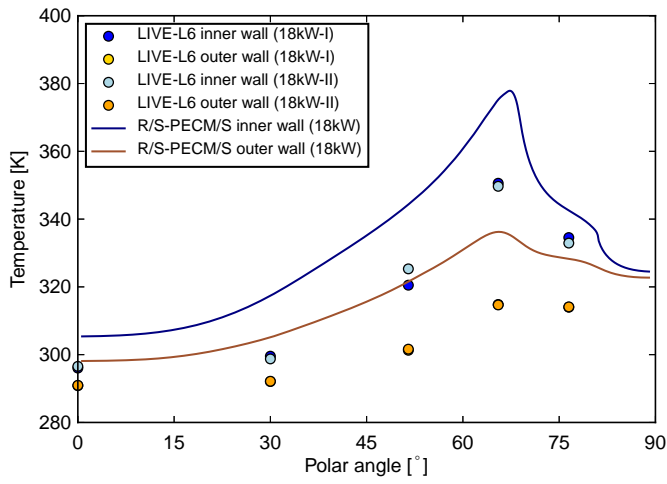

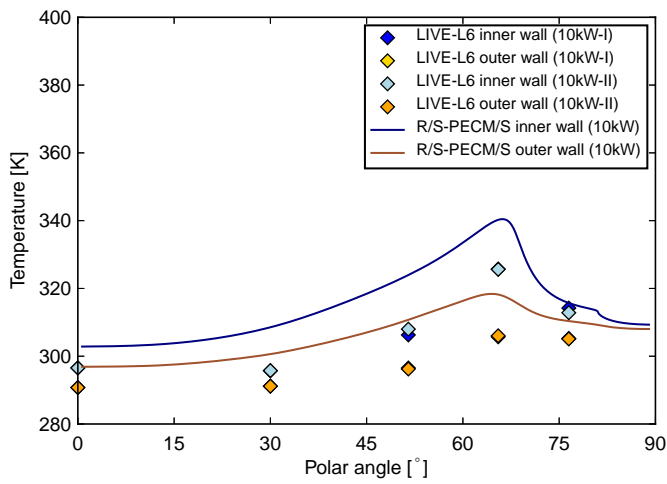Figure 4.45: LIVE-L6: vessel wall temperature profile (18kW)

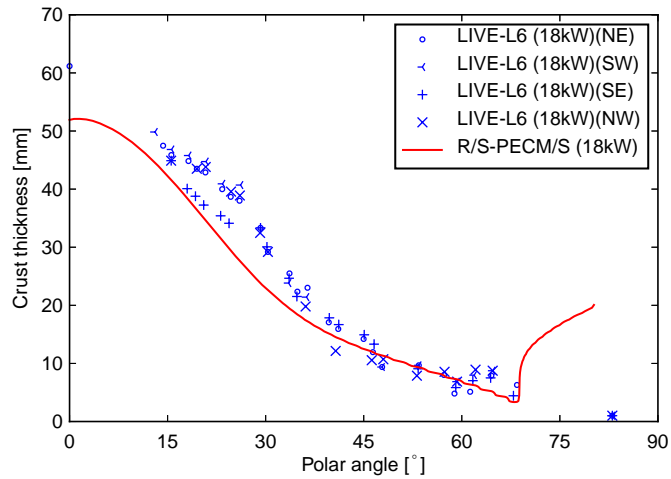Figure 4.46: LIVE-L6: vessel wall temperature profile (10kW)

Figure 4.47: LIVE-L6: crust thickness profile along vessel wall

4.3.5 Summary

In my study, several validation calculations using LIVE test series have been conducted. The results are compared with the measured values as well as the results of RELAP/SCDAPSIM stand-alone calculation. In general, the RELAP/SCDAPSIM-PECM/S coupled system has predicted better heat flux, crust thickness and vessel wall temperature profiles compared to the stand-alone RELAP/SCDAPSIM simulation. The RELAP/SCDAPSIM-PECM/S provided a better agreement also in a transient calculation, which might have impact on creep bahavior in case the structural analysis is coupled. A stratified pool, the lower pool of which was homogeneously heated, was also simulated and the reasonable agreement has been obtained, which cannot be calculated with the stand-alone RELAP/SCDAPSIM. In a top cooling condition, however, the deviation of heat balance was observed as the heating power increases. More investigation is needed when both the melt surface and external wall are cooled by water.

5 Application to a PWR analysis

5.1 IVR analysis of a prototypic PWR

5.1.1 Accident sequence

The benchmark exercise using the TMI-2 reactor showed that the accident sequence of a station blackout (SBO) with surge line break (SLB) was faster than a small break loss of coolant accident (SBLOCA) case [86]. Faster accident progression implies that less time is left for plant operators to take active accident measures such as additional water injection. Some code has predicted that core reflooding could not prevent the core degradation progression and relocation of the molten core into the lower plenum, which led to the vessel failure. It seems thus important to investigate the capability of external reactor vessel cooling system, a passive accident measure, in case of SBO with SLB.

In case of the loss of offsite power, immediate reactor scram, primary pump coastdown and turbine trip occur. It leads also to a feedwater trip, meaning that main feedwater is reduced down to 0 in 60 s on the secondary side, without auxiliary feedwater start-up. The large primary coolant leakage started by the surge line break leads to quick depressurization of the primary system with rapid primary coolant inventory depletion and consequent onset of core uncovery and heat-up.

In this study, the break size of 0.0387 m^2 in the surge line is assumed along with the loss of offsite power. All the emergency core cooling system is assumed to be not functioning, including high pressure injection (HPI), low pressure injection (LPI) and make-up flow. In addition, the recovery of water injection system is not considered, which causes severer conditions, and the core reflooding is not started in all the calculations. The steam generator pressure stays at steady-state value (6.41 MPa) in the first 100 s, then the pressure rises up to 7 MPa linearly in 100 s and remains constant until the end of the transient. Because of the simultaneous loss of offsite power and emergency power, the auxiliary feedwater injection is never activated. The steam generator (SG) water level is let free to evolve according to water evaporation by heat transfer with the primary side. The core has the total power of 2772 MW before the scram. After the scram, the decay heat is given as shown in Table 5.1.

5.1.2 Results of benchmark study

In the benchmark study of Bandini et al. [86], the results of 11 different calculations are compared which were conducted by 10 other organizations. The list of participants as well as the list of used computer codes are given in Table 5.2. In this section, the results of the base

Table 5.1: Core power evolution

Time [s]	Power [MW]
0	2772.00
t_{scram} (scram time)	2772.00
t_{scram} + 1	167.94
t_{scram} + 4	147.96
t_{scram} + 10	130.14
t_{scram} + 40	103.14
t_{scram} + 100	86.13
t_{scram} + 400	65.34
t_{scram} + 800	52.92
t_{scram} + 1000	49.95
t_{scram} + 2000	42.39
t_{scram} + 4000	34.56
t_{scram} + 8000	28.35
t_{scram} + 10000	26.05
t_{scram} + 20000	21.46

case calculations of SBO with SLB are explained. In the base case calculation, HPI/LPI injection systems are assumed not to recover and additional water injection to the core is not performed.

Fig. 5.1 and Fig. 5.2 show the upper plenum pressure and the core collapsed water level, respectively. After the event initiation, all the code predicted similar thermal-hydraulic behavior. The primary pressure approaches the containment pressure within 1000 s, which led to decrease of the coolant inventory. Note that a constant value of 1.5 bar was imposed as a boundary condition of the containment pressure. All the codes estimated early core uncovery in the time range of 400–800 s. Although the timing of molten core relocation varied among the calculations, almost all the codes predicted whole core damage during the transient phase with a total amount of degraded core materials in the range of 140000–160000 kg. The consequent material slumping into the lower head was in the range of 110000–140000 kg. ATHLET-CD used by GRS and RUB as well as RELAP/SCDAPSIM by KIT predicted a much reduced core degradation and material slumping into the lower plenum. The total mass of relocated material in the lower head is shown in Fig. 5.3. The timing of predicted vessel failure was quite different among the codes and varied from 3820 s to 6500 s. The vessel failure criteria used by most participants was the vessel wall melting by temperature. In the GRS calculation, four different vessel failure models were compared: response surface method ASTOR, Larson-Millar approach, Larson-Millar approach with additional consideration of instantaneous plastic rupture, and

simple temperature criterion. The earliest vessel failure was predicted by Larson-Millar approach with additional consideration of instantaneous plastic rupture and was 6509 s, while the latest vessel failure was predicted by response surface method ASTOR and was 8684 s. Tractebel Engineering has used a failure criteria calculated by creep and plastic strain. More investigation of lower head models was recommended as a conclusion of the benchmark analysis.

RELAP/SCDAPSIM/MOD3.5 was used in the benchmark calculation, which is denoted as KIT-SR. The input model for TMI-2 was developed based on the input deck developed by Hohorst et al. [87] at the Idaho National Engineering Laboratory. The input deck was modified to match with the boundary condition given in the benchmark exercise [86]. The RELAP/SCDAPSIM calculation showed a similar thermal-hydraulic behavior compared with the other codes as shown in Fig. 5.1 and Fig. 5.2. The timing of the first material relocation into the lower head was at 1350 s, which was rather earlier compared with other calculations. The main relocation, however, took place at around 4500 s, while other codes have predicted earlier slumping. The adiabatic condition was applied as the boundary condition of the external vessel wall and a vessel failure was not investigated.

In this dissertation, the external cooling volumes were added to the input deck and heat transfer on the external vessel wall was considered. A vessel failure due to creep damage was also taken into account in order to investigate a vessel behavior. The calculation conducted in this dissertation will be described in the following section.

Table 5.2: Participants and codes in OECD-TMI2 benchmark study

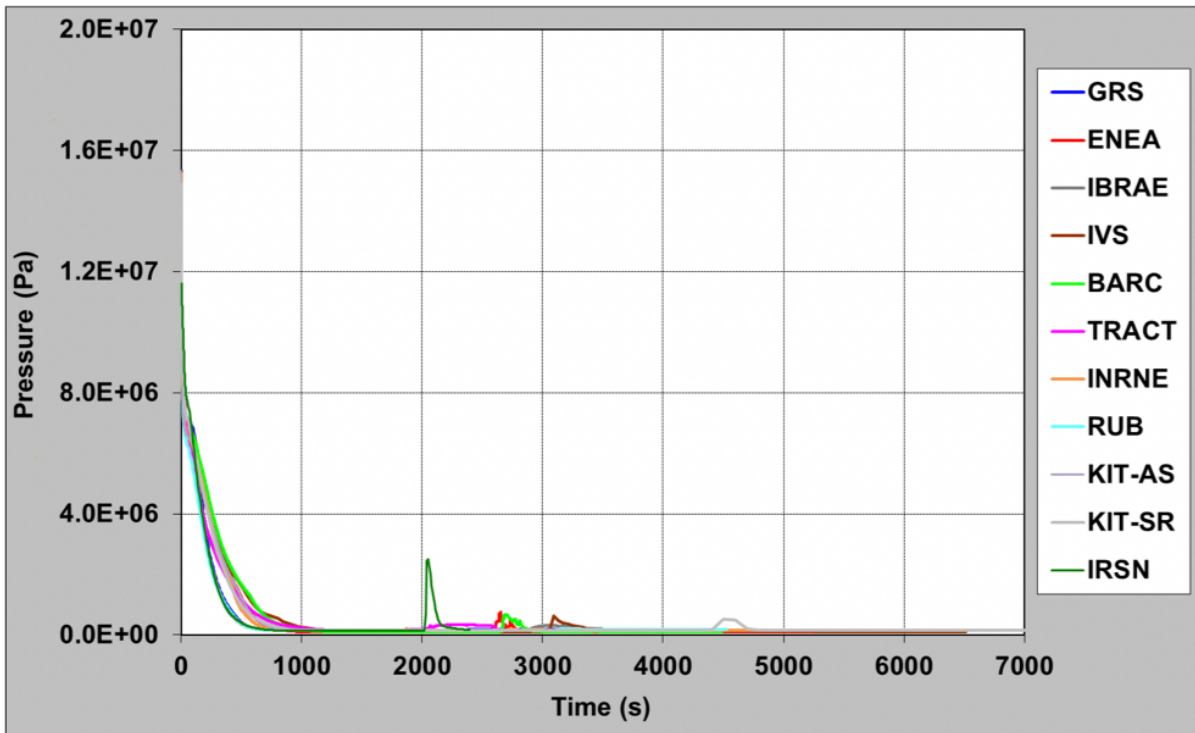| Participant	Country	Code	Acronym
GRS	Germany	ATHLET-CD	GRS
KIT	Germany	ASTEC	KIT-AS
KIT	Germany	RELAP/SCDAPSIM	KIT-SR
RUB	Germany	ATHLET-CD	RUB
ENEA	Italy	ASTEC	ENEA
IRSN	France	ICARE/CATHARE	IRSN
IVS	Slovak Republic	ASTEC	IVS
Tractebel Engineering	Belgium	MELCOR	TRACT
BARC	India	ASTEC	BARC
IBRAE RAS	Russia	SOCRAT	IBRAE
INRNE	Bulgaria	ASTEC	INRNE

Figure 5.1: Upper plenum pressure calculated by different codes in the OECD-TMI 2 benchmark study [86]
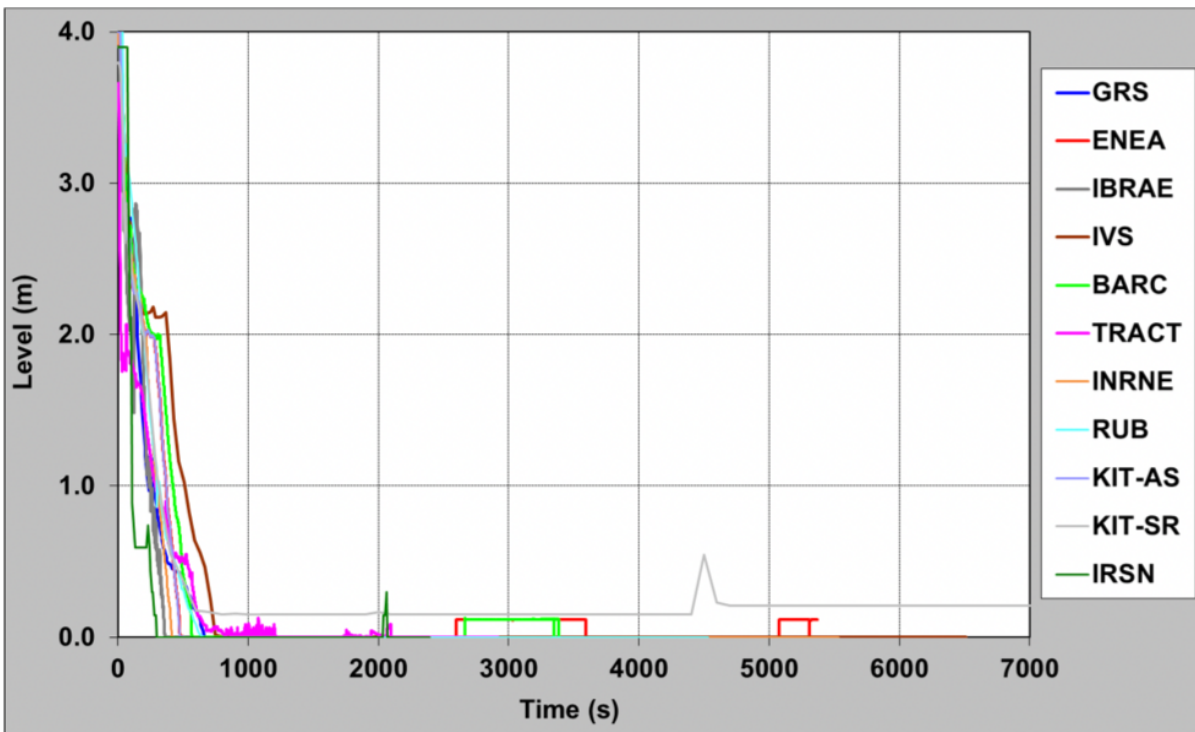

Figure 5.2: Core collapsed water level calculated by different codes in the OECD-TMI 2 benchmark study [86]
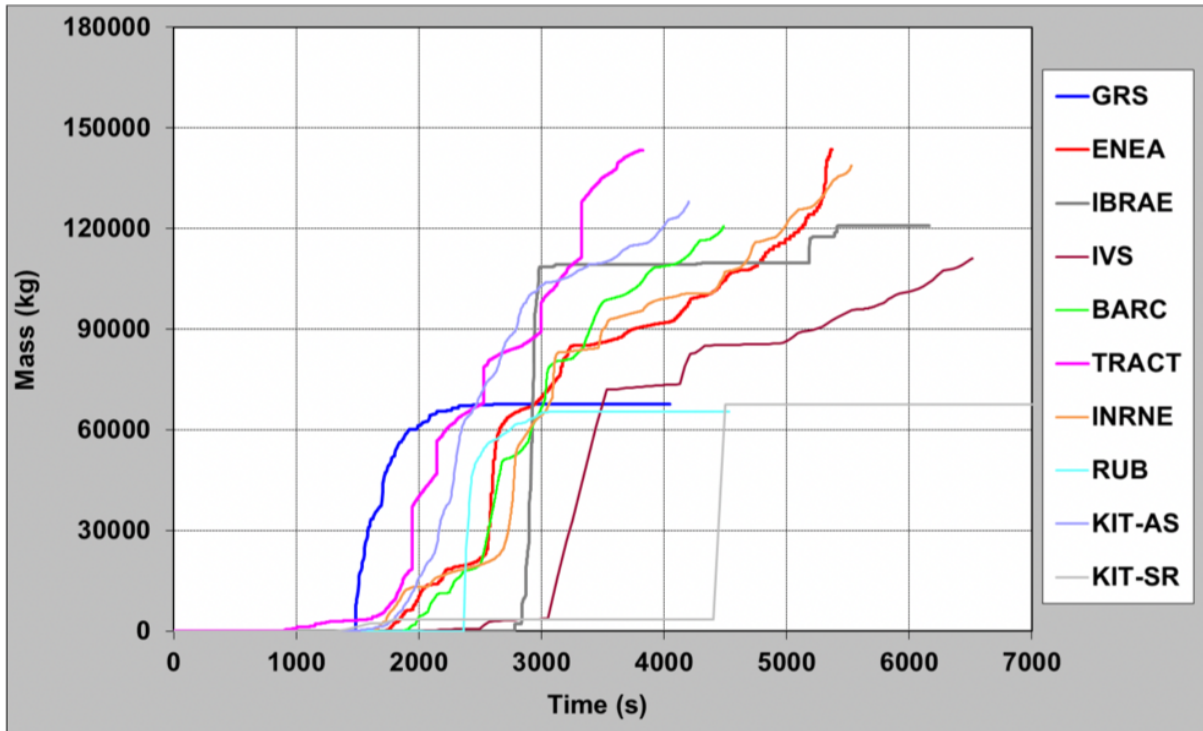
Figure 5.3: Total mass relocated into the lower plenum calculated by different codes in the OECD-TMI 2 benchmark study [86]

5.2 Calculation results of RELAP/SCDAPSIM

5.2.1 RELAP/SCDAPSIM input models for TMI-2

The input deck used for this dissertation was based on the one developed for the benchmark exercise by Bandini et al. [86]. In this dissertation, an external vessel cooling loop was added for IVR calculations. In a previous study by Dinh et al. [20], different sizes and shapes of the gap between the RPV and the cooling vessel were compared to support the investigation of IVR capability of AP1000. As a first step, a gap of 3 inch was applied in this study. The schematic image of the RELAP5 nodalization is shown in Fig. 5.4. Heat transfer of the RPV lower head wall and the molten pool in the lower head is treated by COUPLE module. The COUPLE nodes representing the vessel external wall are connected with the RELAP5 volumes for external cooling loop, while those representing the lower head volume that captures relocated molten materials from the core are connected with the RELAP5 volume of the lower head (Fig. 5.5).

5.2.2 Without external cooling

As soon as the break opening and loss of offsite power were initiated at the time of 0 s, the reactor scram occurred and the primary pump stopped. Within 600 s, the primary system was depressurized to the containment pressure of 0.15 MPa, which led to the coolant inventory depletion. The complete core uncovery was predicted at around 1000 s. The upper plenum pressure and the collapsed water level are shown in Fig. 5.6. Due to this early core uncovery, heat-up of core material started within 1000 s after the event initiation. The molten pool started
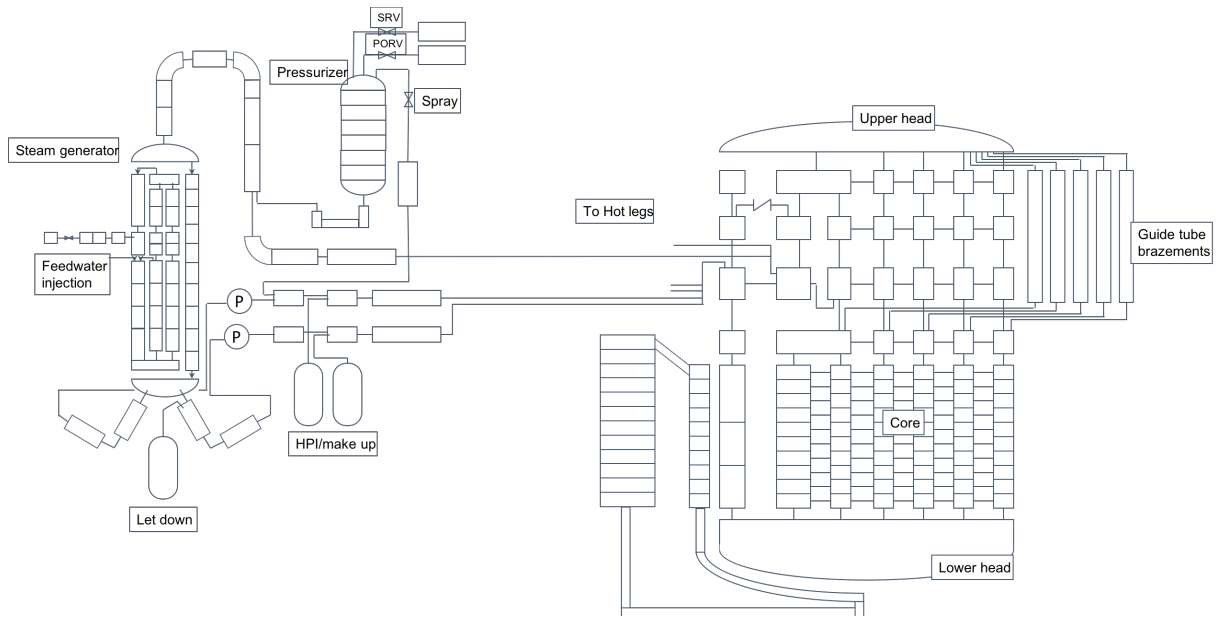
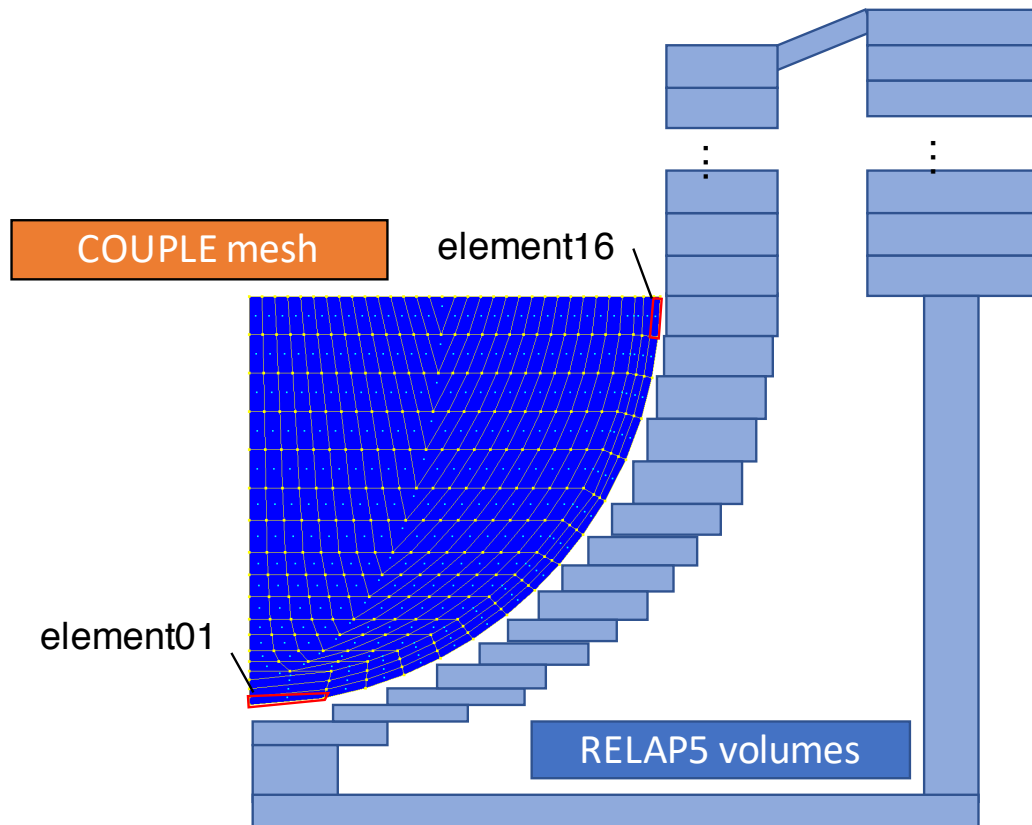Figure 5.4: RELAP5 nodalization of the TMI-2 reactor system

Figure 5.5: COUPLE nodalization in the lower head and RELAP5 nodalization for external reactor vessel cooling volumes
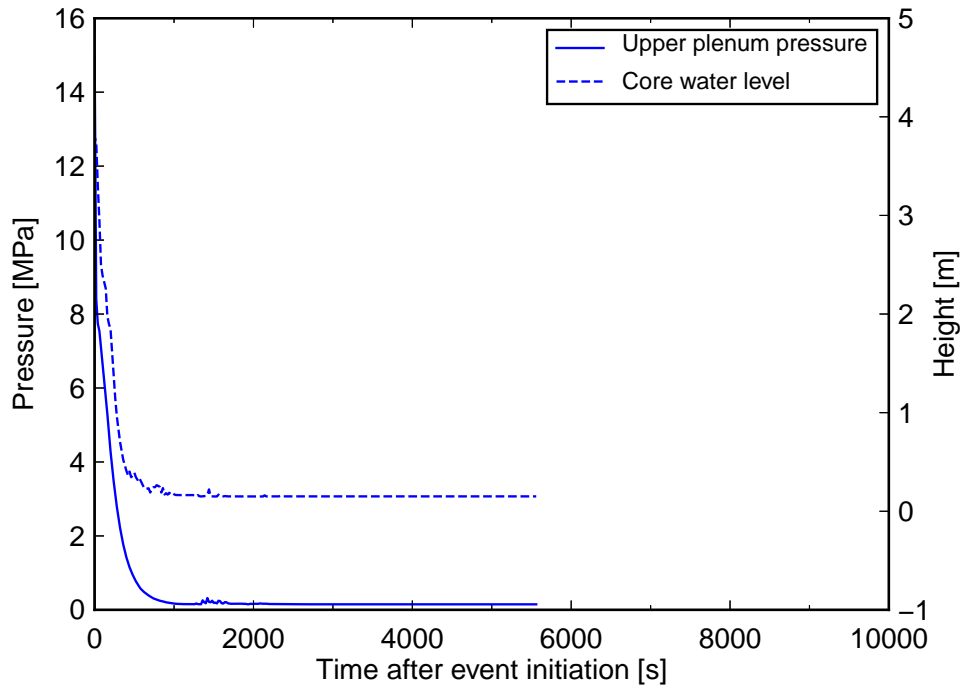
Figure 5.6: Upper plenum pressure and core water level in case with external cooling

to form at first in the core region at around 1500 s. The first relocation of molten material to the lower head took place at 3140 s, main components of which were the absorber materials with the mass of 550 kg. The absorber material relocated constantly until 4000 s and the accumulated mass was 2733 kg. Since the absorber material does not contain the internal heat source, the vessel wall temperature increased only gradually and did not reach its melting temperature. The mass of core material relocated into the lower head and the maximum outer wall temperature are illustrated in Fig. 5.7. The material damage due to the creep deformation was not predicted at this time. The main relocation event happened at 4840 s with U-Zr-O mixture. The total mass of relocated material in the lower head reached 104847 kg, which corresponded to the molten pool height of 1.58 m. Since the heat could not be removed enough and the vessel temperature increased continuously, the vessel rupture was predicted at 5375 s in the element 09 due to the creep deformation.
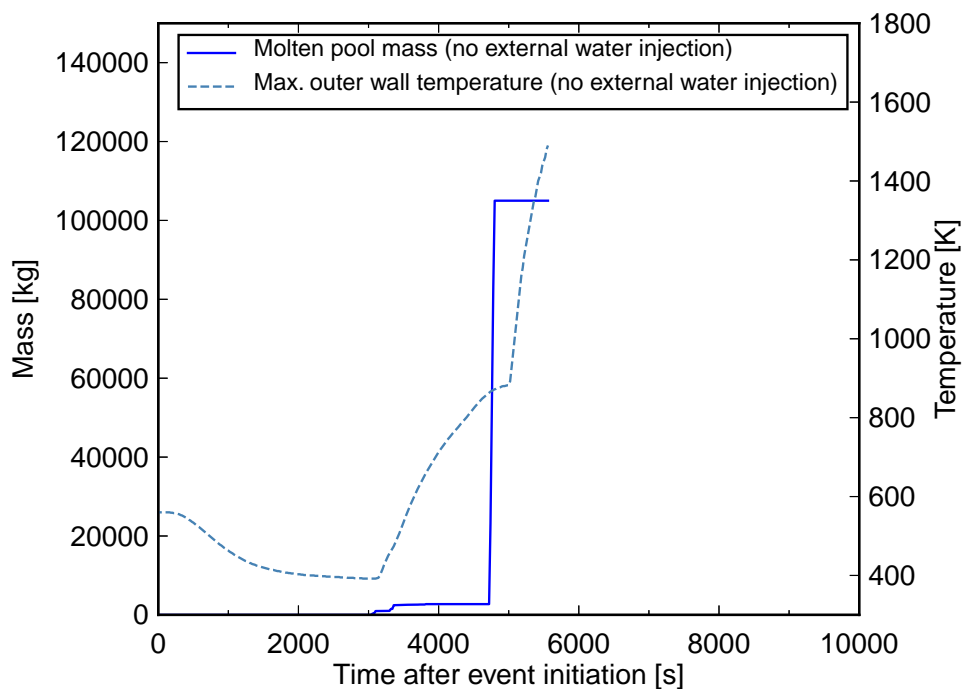
Figure 5.7: Mass of relocated material in the lower head and maximum outer wall temperature in case without external cooling

5.2.3 With external cooling

In order to evaluate the IVR system which is assumed to be installed in the TMI-2 reactor, different water injection cases have been analyzed for this dissertation. The external water injection was initiated when the core exit temperature exceeds 920 K with the mass flow rate of 200 kg/s. The total amount of water available for the external cooling was assumed to be 100 t. As a comparison, two cases with different injection water temperatures were assumed: 20 °C and 95 °C.

The accident progression was the same as the case without external cooling until the core exit temperature exceeds 920 K at the time of 660 s. As shown in Fig. 5.8, similar relocation events are observed, although slight difference in the amount and timing of relocation can be seen. In the case of 20 °C, the time of relocation was delayed approximately 440 s compared to the case of 95 °C. Fig. 5.9 shows the water injection and the mass flow rate at the vessel bottom inlet. The water injection to the external volume was completed at 5660 s and natural circulation was established after the molten pool in the lower head was formed, as a result of density difference caused by lower head surface direct heating.

In case of 20 °C, large fluctuation were observed in mass flow rate between 10000 s and 20000 s until the temperature of external cooling water reaches the boiling temperature. On the other hand, smaller fluctuation has occurred in case of 95 °C. After 20000 s, the mass flow rate of

both cases remained steady around 300 kg/s. A reason of the fluctuation might be geysering phenomena, defined as repeated vaporization, caused by thermal non-equilibrium due to a change in hydrostatic head, and being observed in a subcooled boiling condition. Flow instabilities including geysering have been observed by Janssens-Maenhout et al. [88] in the SUCOT (Sump Cooling Two-phase) tests at KIT, in which behaviors of a cooling loop with subcooled boiling at a heated bottom plate were investigated. The ULPU-V tests conducted by Dinh et al. [20] at University of California Santa Barbara (UCSB) has a cooling loop representing a prototypic design of AP1000. The lower part of the cooling loop represents the lower head with molten pool and was heated by copper plates to simulate heat transfer from the molten pool to the external cooling water. Although additional coolability margins were confirmed compared with the previous experiments, the natural circulation flow was dominantly subcooled, and was modulated by periodic flashing and frictional phenomena. Therefore, a further examination of flow fluctuation and of CHF performance was recommended. A numerical analysis on the ULPU-V tests was conducted by Azka [89] and it was concluded that geysering phenomena were predicted in case bubble nucleation exists and caused a very severe mass flow oscillation.

The heat balance of each case is shown in Fig. 5.10, respectively. Due to the large fluctuation between 10000 s and 20000 s, the heat removed from the molten pool showed also varied between 15 MW and 40 MW in case of 20 °C, while stable heat removal was performed in case of 95 °C. The fluctuation of heat removal rate had affected the accumulation of damage parameter. As shown in Fig. 5.11a, the damage parameter increased up to 0.1 by 20000 s. In case of 95 °C, its values were small and the material damage was negligible (Fig. 5.11b). One of the reasons why the damage parameter increased more in case of 20 °C compared to in case of 95 °C might be the pressure fluctuation observed in case of 20 °C. Fig. 5.12 illustrates the inner and external vessel pressures for each case. The inner vessel pressure remained steady in 0.15 MPa, which was the same as the containment pressure. The difference between two cases is clear in the external vessel pressure. Due to the large fluctuation of mass flow rate in the external path, the pressure oscillated between 0.06 MPa and 0.29 MPa in case of 20 °C, while the pressure difference was rather small and was between 0.15 MPa and 0.19 MPa. Another reason would be the higher vessel wall temperature. The evolution of the vessel inner and outer wall temperatures at 10000 s, 15000 s and 30000 s is shown in Fig. 5.13. The difference of external wall temperature between the cases was small compared to the difference of inner wall temperature. Due to the smaller heat removal capacity between 10000 s and 20000 s, the inner wall temperature was higher in the polar angle range of 10° and 50°. Larger temperature difference was observed at 15000 s. At 30000 s when the natural circulation with constant mass flow rate was established, the temperature difference became smaller except for the vessel bottom. The difference of maximum inner temperature was resulted from the difference of the molten material amount and corresponding decay heat relocated in the pool. The RELAP/SCDAPSIM does not consider ablation of the lower head wall caused by the thermal attack of the molten core material. In both cases, the inner vessel temperature exceeded 1700 K, the melting temperature of the steel. When the thickness change of the vessel wall was considered, creep deformation

might be larger, which leads to more material damage. Therefore, in the future, the inclusion of ablation and investigation on its effect is inevitable.
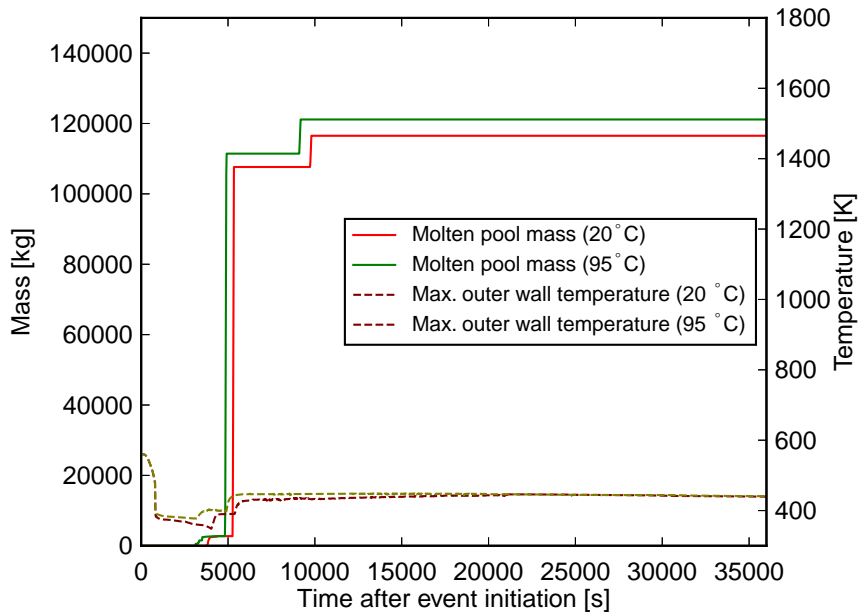

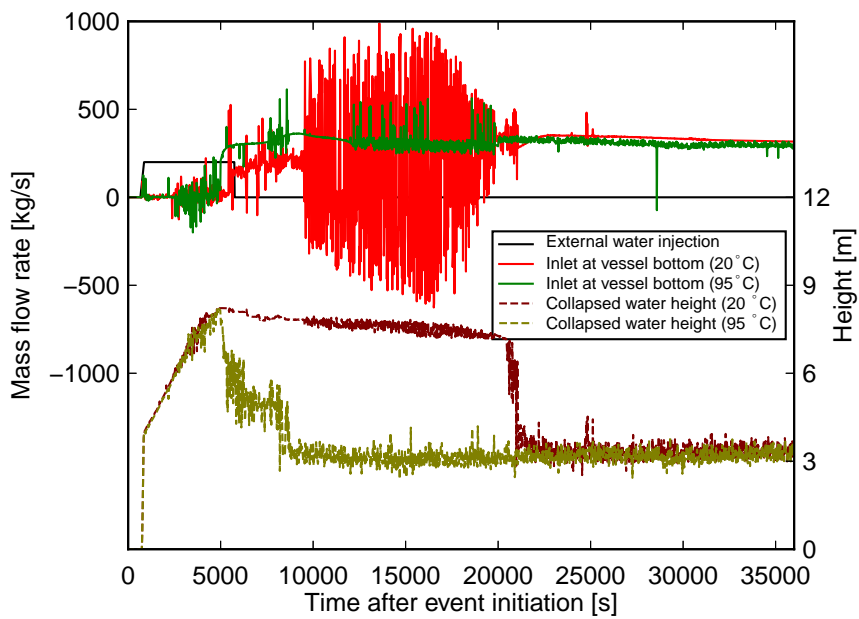Figure 5.8: Mass of relocated material in the lower head and maximum outer wall temperature

Figure 5.9: Mass flow rate and collapsed water height of external cooling
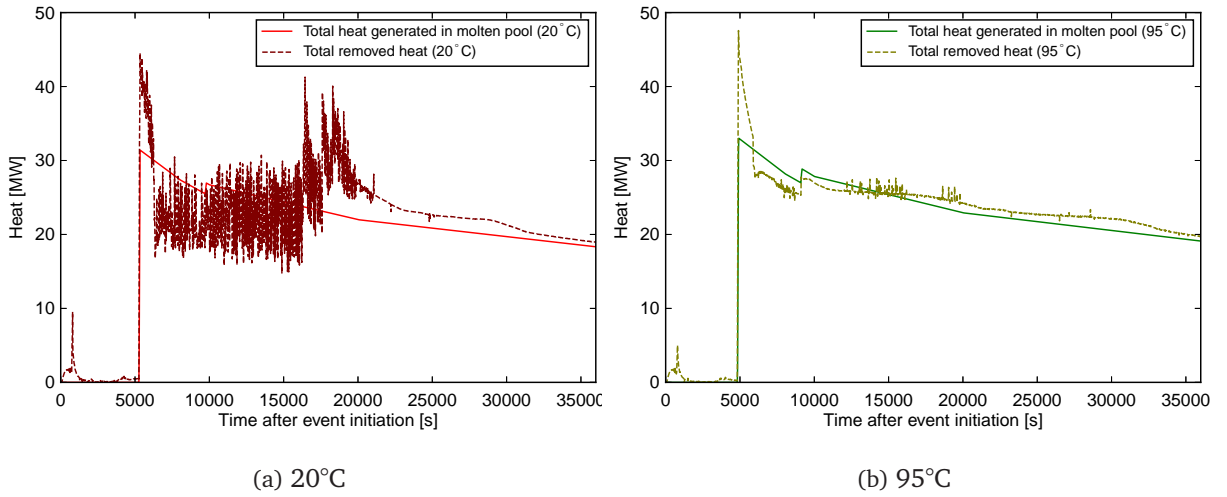
(a) 20°C

(b) 95°C

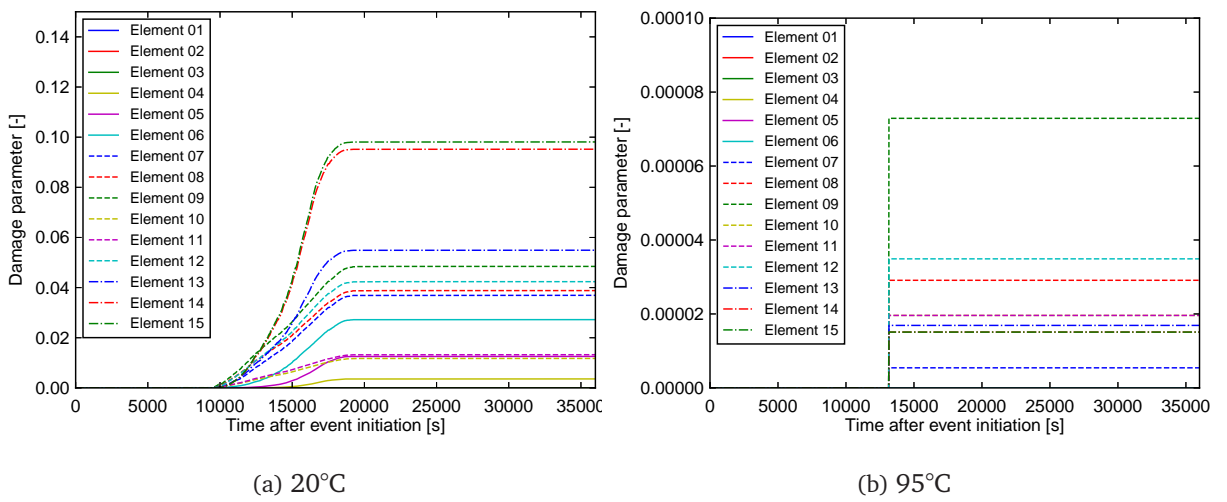Figure 5.10: Heat balance

(a) 20°C

(b) 95°C

Figure 5.11: Damage parameter of vessel wall
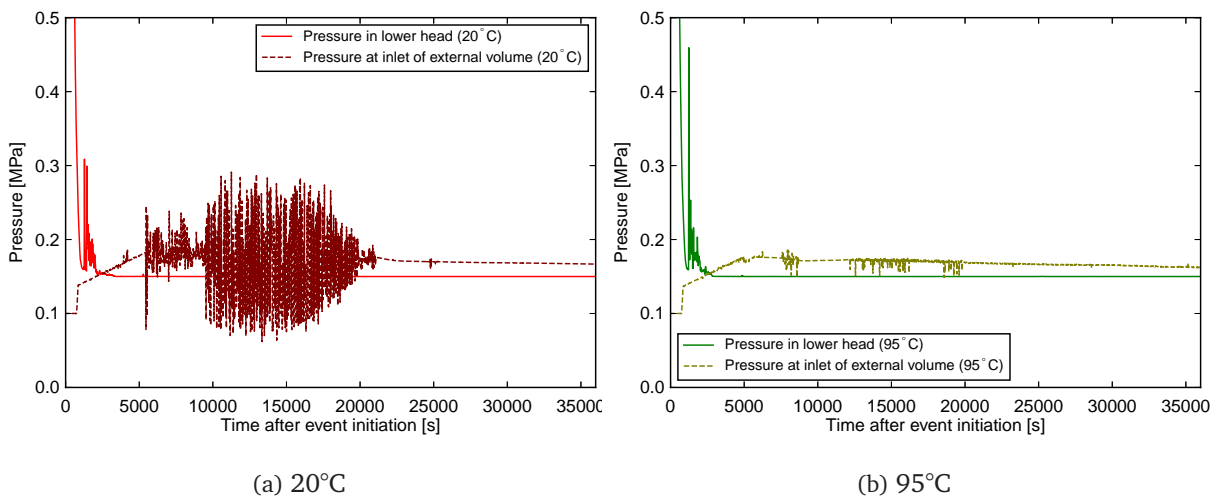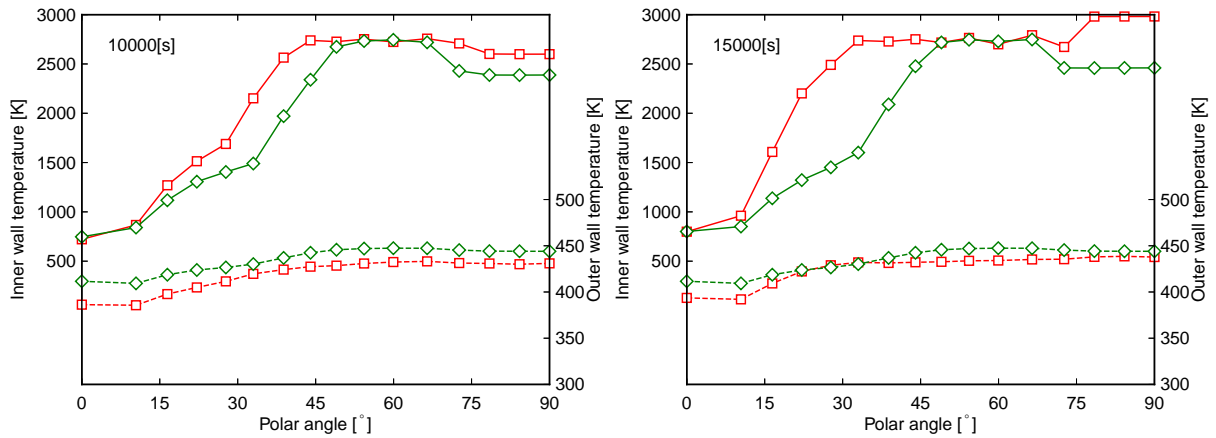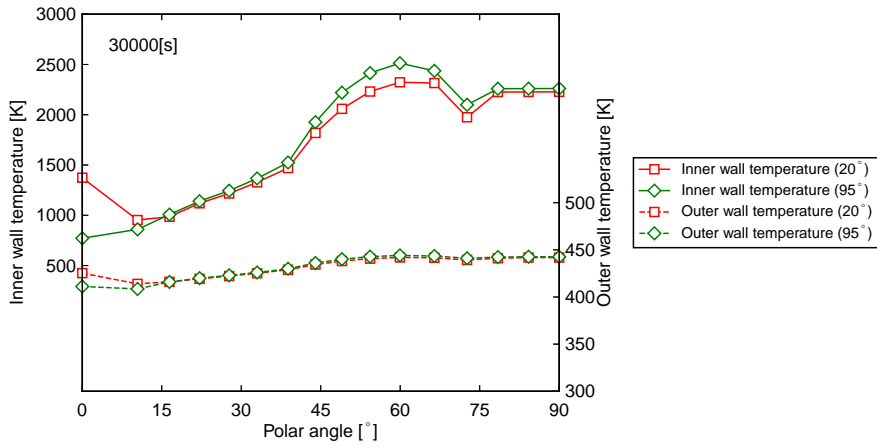

(a) 20°C

(b) 95°C

Figure 5.12: Pressure of inner and outer vessel volumes

(a) 10000 s

(b) 15000 s

(c) 30000 s

Figure 5.13: Vessel wall temperature

5.3 Calculation results of coupled system

5.3.1 Without external cooling

An accident scenario of SBO with SLB was calculated for this dissertation by using the RELAP/SCDAPSIM-PECM/S coupled system. The same boundary conditions were used as the one in the RELAP/SCDAPSIM stand-alone calculation in Section 5.2. As shown in Fig. 5.14, the lower head heat transfer and its mechanical behavior were calculated by PECM/S instead of the COUPLE module.

The predicted accident progression was identical until the molten core relocation to the lower head. The first relocation into the lower head occurred at 3314 s, the main components of which were the absorber material with a mass of 623 kg. The absorber materials intermittently relocated into the lower head until 4385 s and the accumulated mass was 2733 kg. The main relocation event took place at 4753 s with U-Zr-O mixture. At 4827 s, the total mass of relocated material in the lower head reached 102411 kg. The liquid fraction of molten pool at 5000 s is shown in Fig. 5.15. The crust was predicted along the inner vessel wall, which led to slower heat up of the lower head wall compared to the vessel wall above the molten pool. The heat generated in the molten pool was mostly removed from the pool surface by the convection and radiation heat transfer to the environment. The steam inside the RPV was superheated to more than 2000 K. The inner vessel wall above the molten pool surface was heated through convection and radiation heat transfer. The vessel temperature profile and the damage parameter profile at 5256 s are show in Fig. 5.16 and Fig. 5.17, respectively. A fast temperature escalation at the inner vessel wall resulted in large temperature difference inside the vessel wall, which caused high stress due to different thermal expansion in hot and cold areas.
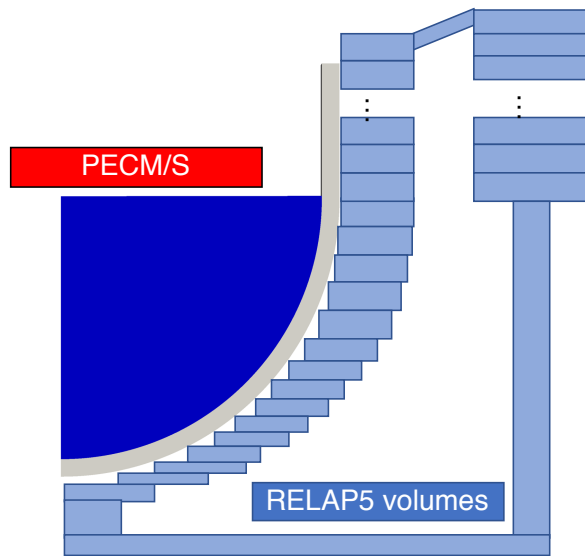
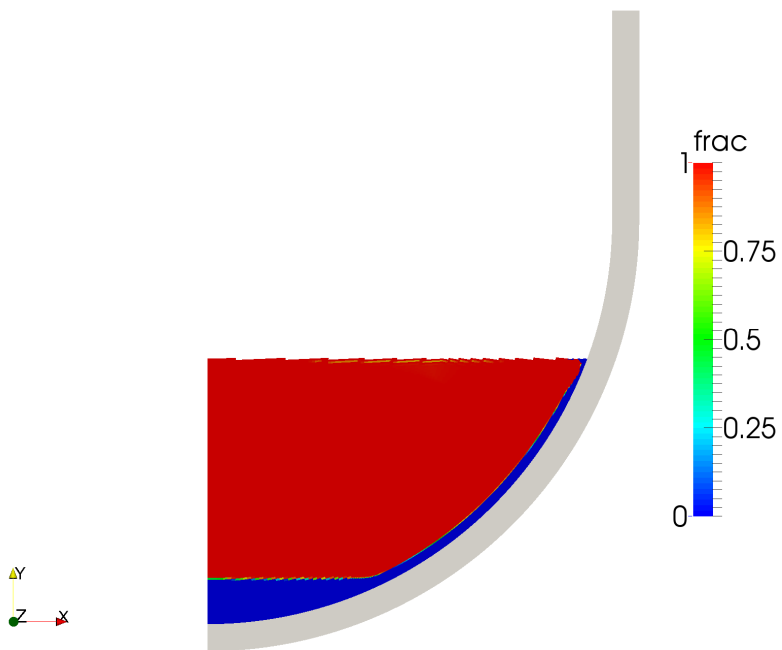Figure 5.14: Schematic image of coupled system

Figure 5.15: Liquid fraction of molten pool at 5000 s after event initiation
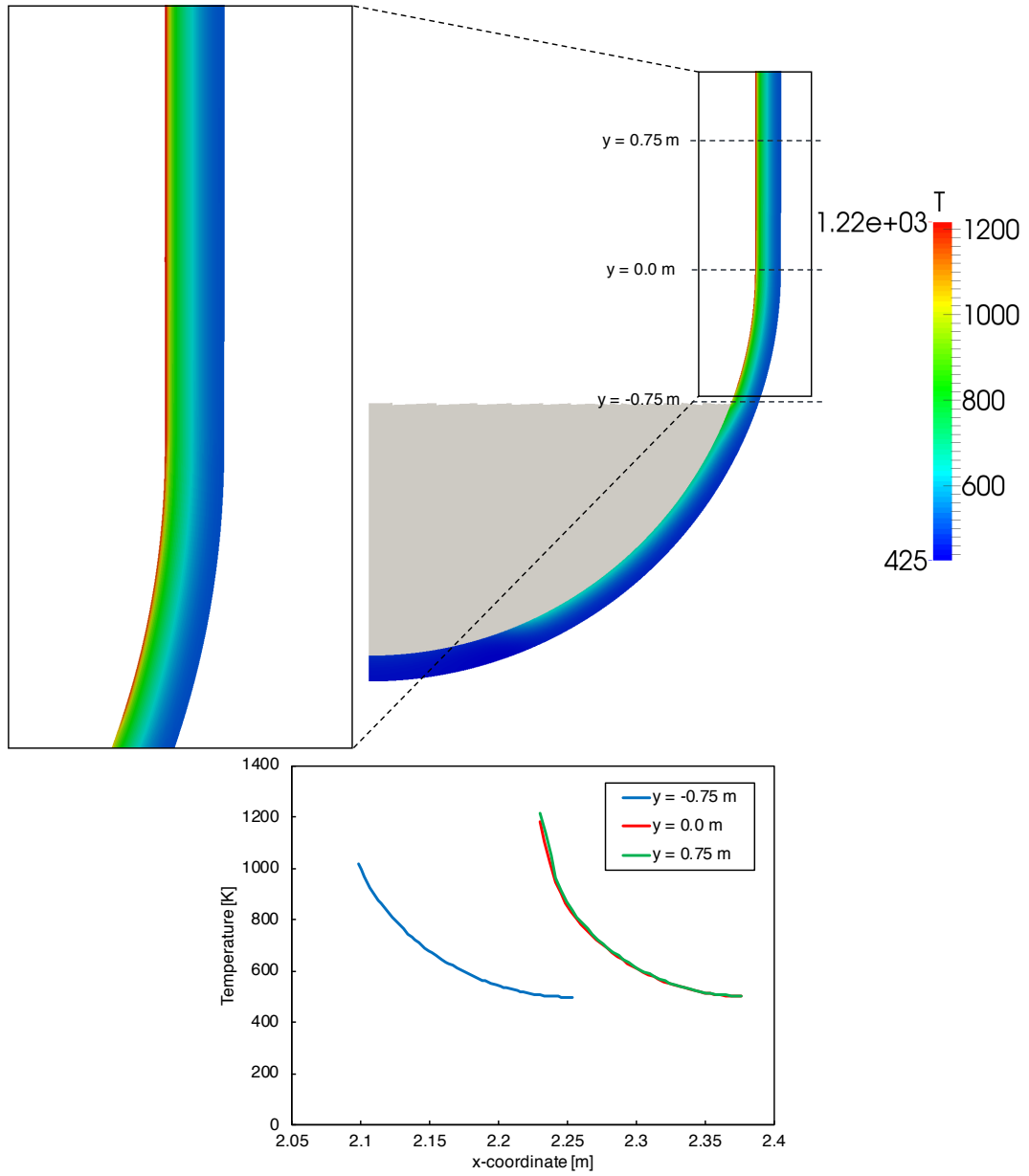
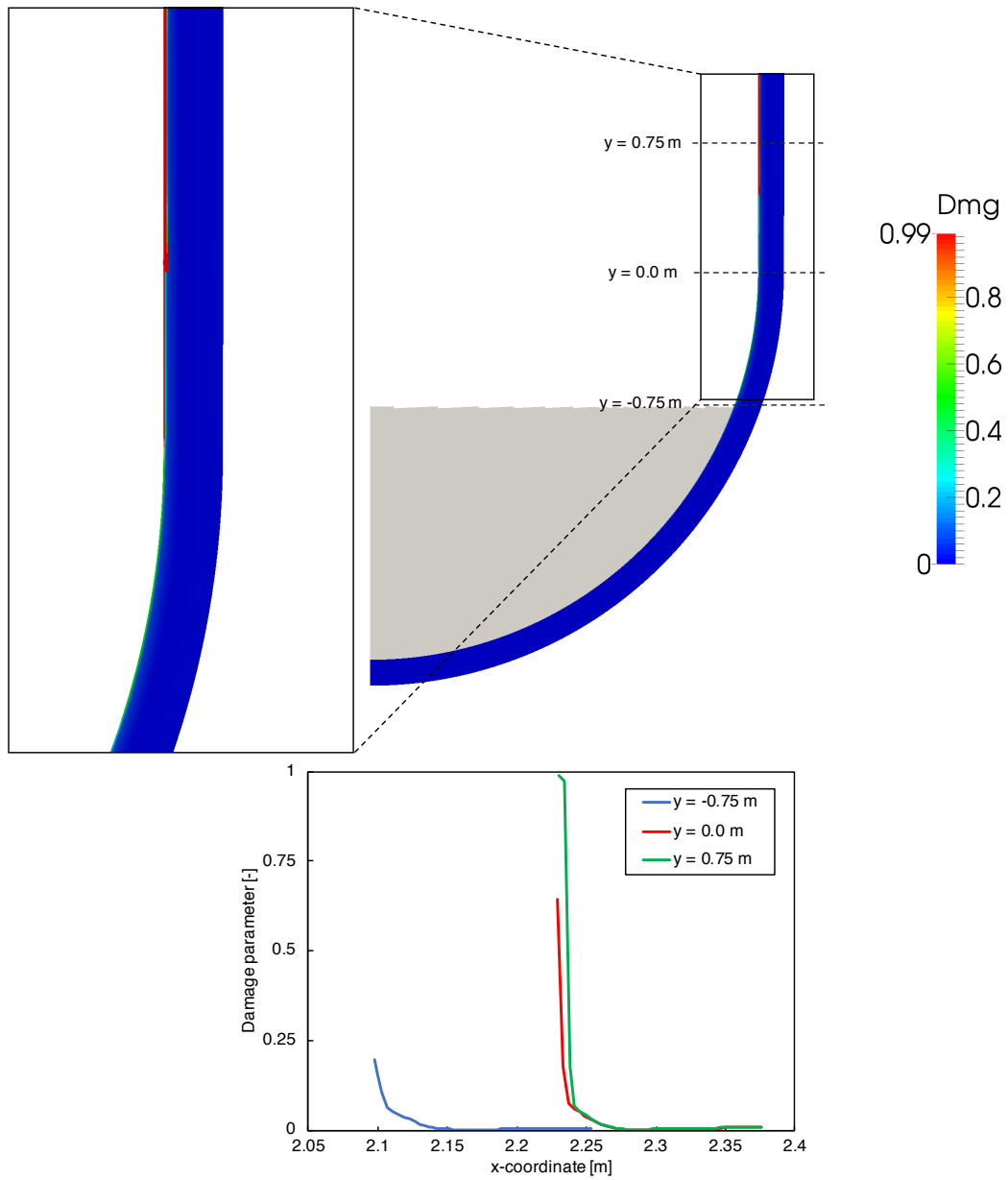Figure 5.16: Vessel temperature at 5256 s after event initiation

Figure 5.17: Damage parameter at 5256 s after event initiation

5.3.2 With external cooling

The external cooling was initiated when the core exit temperature exceeded 920 K at 651 s. The first slumping occurred at 3430 s with the absorber materials. The absorber materials has relocated intermittently until 4046 s and the accumulated mass was 2733 kg. The main slumping with fuel materials has started at 5155 s, which was approximately 400 s later than the case without external cooling. When the external wall was cooled with water, the temperature of the lower head inner volume was 100 K lower compared with the case without external cooling. This might have led to the slight delay of the main slumping event. The slumping has continued till 5233 s with the total mass of 105961 kg. As the case without external cooling, the crust layer was predicted along the inner vessel wall. The liquid fraction of the molten pool at the time of 5500 s is shown in Fig. 5.18. The heat of the molten pool was removed mostly from the melt surface. The volume inside the lower head was heated rapidly, which heated up the inner vessel wall above the melt surface. Due to the large stress caused from the temperature difference in the vessel wall, a part of the inner vessel wall was fully damaged at 5619 s. The vessel temperature and the damage parameter profiles at 5619 s are shown in Fig. 5.19 and Fig. 5.20, respectively. Since the solver does not include models that consider material ablation or erosion, it could not further calculate the case with the vessel damage. A remarkable result is that the position where the vessel fail might occur was not the vessel, where molten pool exists, but the region above the melt surface.
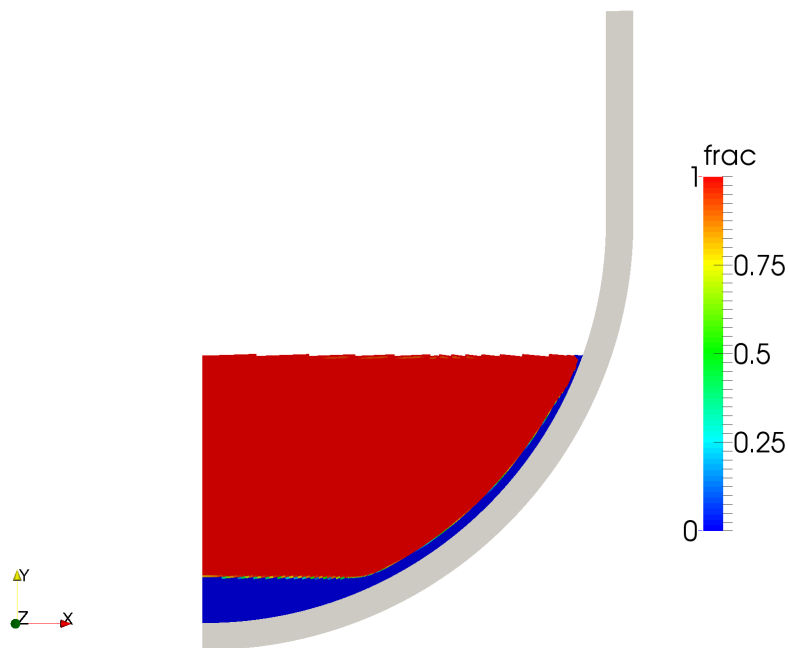

Figure 5.18: Liquid fraction of molten pool at 5500 s after event initiation
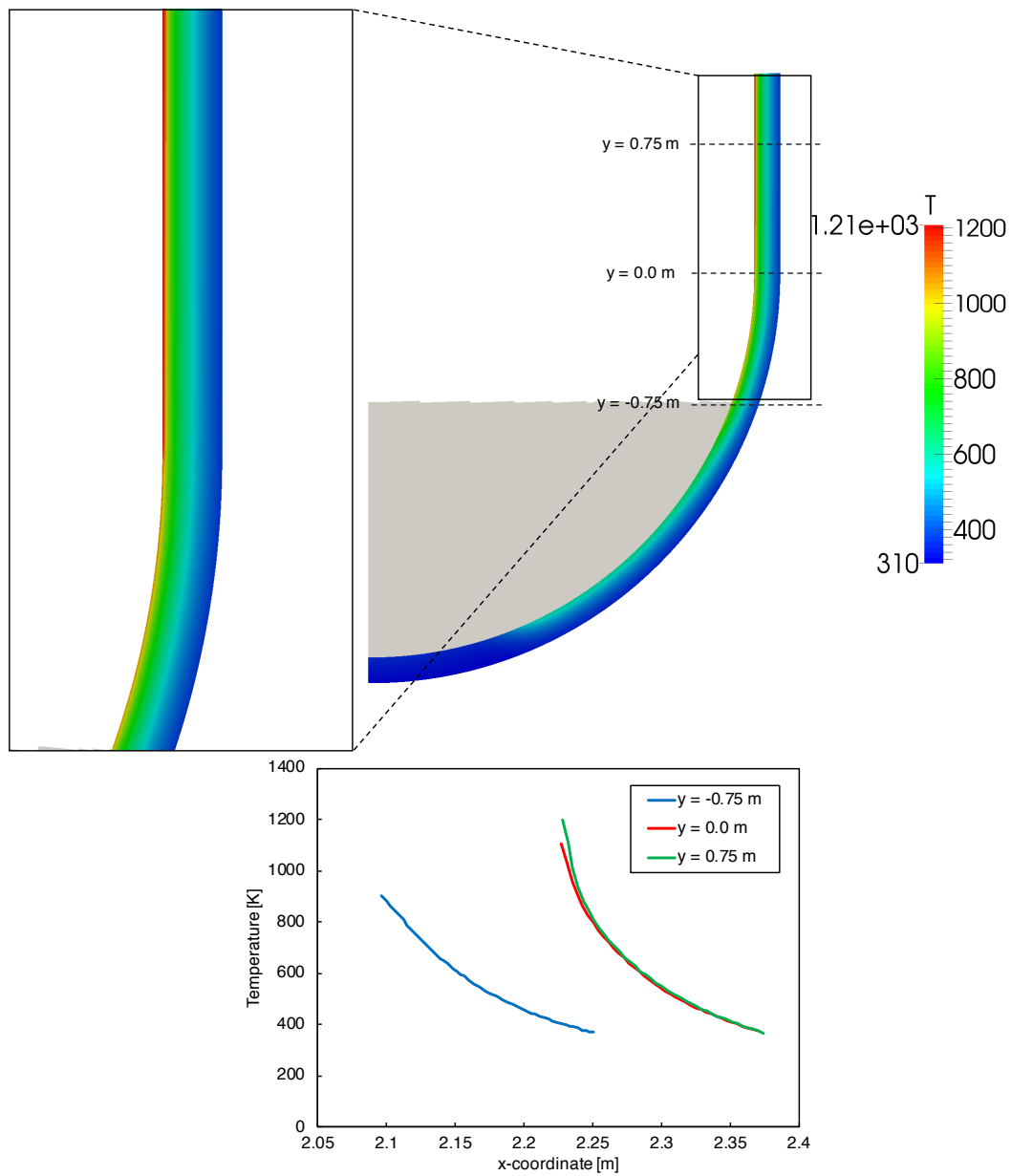
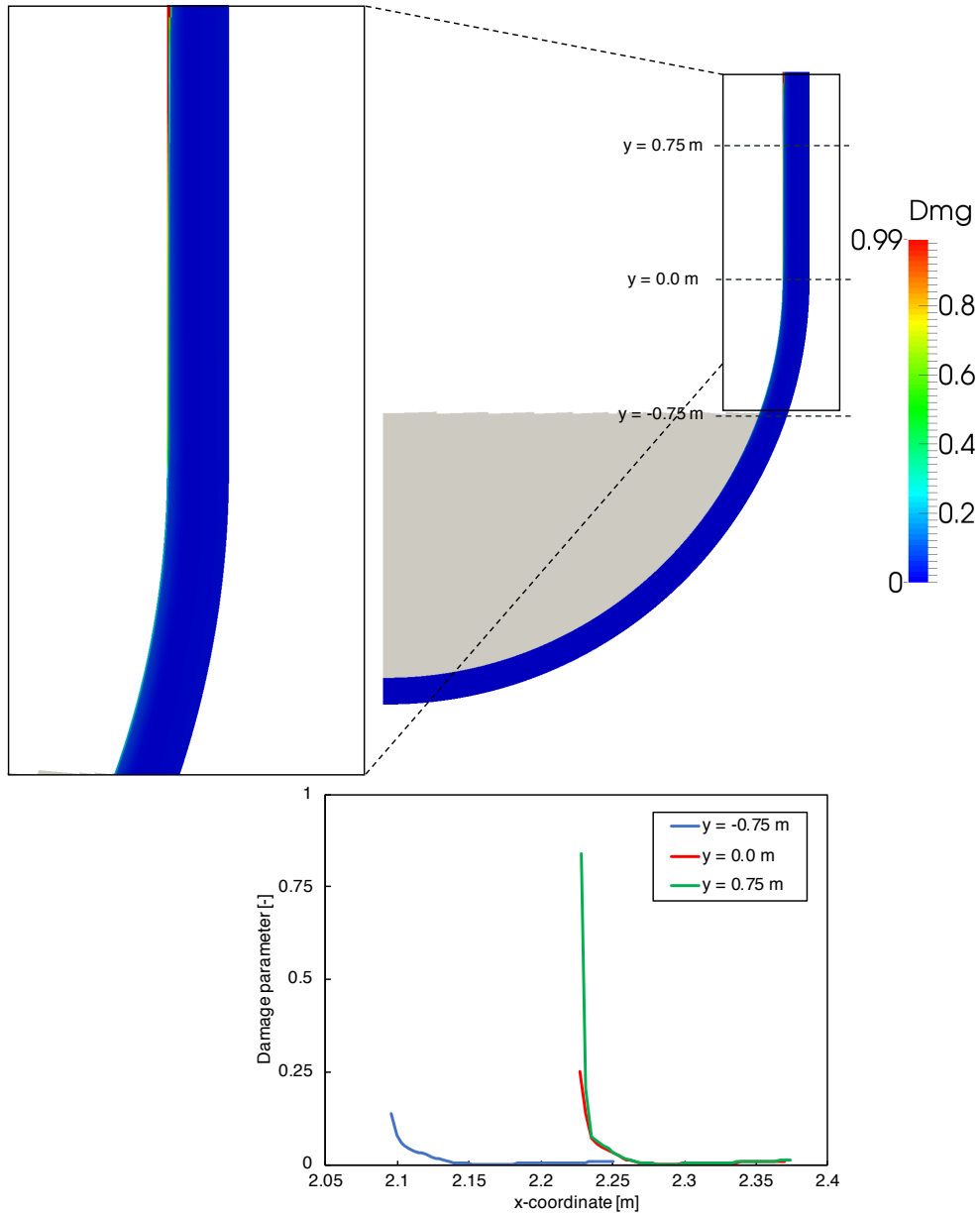Figure 5.19: Vessel temperature at 5619 s after event initiation

Figure 5.20: Damage parameter at 5619 s after event initiation

5.4 Summary

The RELAP/SCDAPSIM stand-alone calculations have been conducted with three cases: one case without external cooling and two cases with external cooling with cooling water temperature of 20 °C and of 95 °C. The case without external cooling showed that the vessel failure occurred at element09, which is the top of the molten pool region, due to the high temperature and corresponding creep damage. The cases with external cooling showed that, in most cases, the highest inner vessel temperature located inside the molten pool region. In both cases, the heat generated in the molten pool was successfully removed by the external cooling water and the vessel integrity was secured. In case with a cooling water temperature of 20 °C, the creep damage parameter increased up to 0.1. This is because the mass flow had large fluctuations until the external cooling water reaches the saturation temperature and the pressure of the external volume had oscillated accordingly. On the contrary, the internal pressure remained stable. Therefore, the pressure difference had a large fluctuation, which led to a creep damage. In case with a cooling water temperature of 95 °C, the mass flow and the pressure were more stable and a remarkable creep damage was not predicted.

As a comparison, the same accident scenario was analyzed using the RELAP/SCDAPSIM-PECM/S coupled system. Remarkably, the initial vessel failure occurred at the inner vessel wall above the melt surface. Since the solver does not include models that consider vessel ablation or erosion, the calculation has been terminated at the moment when the inner wall has been fully damaged. Further model implementation is needed to take into account more detailed mechanical analyses. This difference came from the crust prediction at the melt surface. A crust layer was predicted at the melt surface in the RELAP/SCDAPSIM stand-alone calculation, while it was not formed in the coupled analysis. Without a crust layer, the heat transfer from the melt surface to the lower head inner volume is larger and more heat was transferred consequently to the vessel inner wall.

6   Summary and Conclusion

The focus of the present work is improving and developing numerical simulation tools for IVR strategy. With increased attention on the IVR strategy, applicability of the existing reactor analysis code is of high interest. Few evaluation, however, has been conducted so far using the recent molten pool experiments. In the present study, the COUPLE module, the lower head heat transfer analysis module implemented in RELAP/SCDAPSIM, was assessed and improved. Originally, only one RELAP5 volume could be selected as the external cooling and a saturated temperature was assumed. The modification of the module enabled now multiple volumes and any cooling condition for the external volumes. In addition, the natural convection heat transfer correlations recently obtained in the ACOPO and the UCLA experiments were implemented into the module. The evaluation work was conducted with the LIVE-L1 and -L7V experiments. The numerical analysis showed that the ACOPO correlation gave the better results of heat flux along the vessel wall. The tendency of predicted crust thickness, however, remained similar among the different correlations and the thickness was underestimated especially at the bottom of the vessel. During the air-cooled phase in the LIVE-L1 test, a lower vessel wall temperature was predicted due to the thin crust layer predicted all along the inner vessel wall. It can be concluded that the crust formation model itself affected the calculation and that its further improvement is needed.

The COUPLE module assumes a homogeneous pool and effects of a stratified pool cannot be captured. Moreover, it has a simple damage progression model based on creep damage and a detailed structure analysis was not possible. The PECM, one of the specified model for more detailed lower head molten pool heat transfer analysis, developed based on CFD-investigations, was implemented into OpenFOAM. The solver was evaluated using the LIVE-L7V test. The solver was further extended to include structure analysis model, considering thermal expansion, plasticity, creep and material damage. The material data for two different steels were prepared: French steel 16MND5 and American steel SA533B1. The EC-FOREVER-2 and -4 experiments, in which the vessel was produced with French and American steel, respectively, were numerically analyzed with the extended solver (PECM/S). Although the numerical analysis demonstrated that the emissivity of the melt surface and the mesh type (fixed or updated) affected the results significantly where the primary creep was dominant, the solver generally had a capability of predicting the vessel deformation and failure process.

Since the PECM/S is the specific solver for the lower head analysis and is not able to calculate whole accident scenario with reactor thermal hydraulics, it was coupled with RELAP/SCDAPSIM in order to utilize the strength of each code/solver. The coupling was

performed through OpenMPI, a message passing interface. The coupled system was validated against homogeneous pool experiments of the LIVE-L1, -L7V and -L11 tests and a stratified pool test of the LIVE-L6 test. The numerical results of homogenous pool tests were compared also with the RELAP/SCDAPSIM stand-alone analysis and showed more detailed and better agreement with the experimental data.

A severe accident scenario of SBO with SLB in a prototypical PWR was calculated using the stand-alone RELAP/SCDAPSIM and the coupled system. The RELAP/SCDAPSIM stand-alone calculation showed the vessel failure at the top of the molten pool in case without external cooling. External cooling cases were calculated with two different inlet water temperature: 20 °C and 95 °C. Although the decay heat was successfully removed by the cooling water, the vessel damage was accumulated in case of 20 °C due to the pressure oscillation of external volumes until the water was heated up to the saturated temperature. The RELAP/SCDAPSIM-PECM/S coupled system predicted a thicker crust layer along the inner vessel wall, which prevented heat transfer from the molten pool to the vessel wall. Most of the heat generated in the molten pool was removed from the melt surface and transferred by convection and radiation to the inner vessel wall above the melt surface. The inner vessel wall above the melt surface was heated up and a large temperature difference inside of the vessel wall was predicted. Due to plastic deformation, the inner vessel wall was damaged in both cases with and without external cooling. Through the analyses, it was found out that different crust thickness prediction led to different position of possible vessel failure. Therefore, further investigation is needed in the crust formation and the vessel damage.

Through the present work, two main achievements can be concluded.

- The COUPLE module implemented in RELAP/SCDAPSIM was assessed and improved, which enabled more accurate coupled analyses of the melt pool convection, vessel wall heat conduction, and external boiling heat transfer during a core-melt severe accident.

- The coupled system of RELAP/SCDAPSIM–PECM/S enabled the analysis of structural behavior of the vessel wall as well as more accurate thermal analysis of the molten pool and vessel wall.

Bibliography

[1] IAEA, *Basic safety principles for nuclear power plants, 75-INSAG-3 Rev. 1, INSAG-12*. Vienna, Austria: International Atomic Energy Agency, 1999.

[2] IAEA, *Accident analysis for nuclear power plants – Safety reports series No. 23*. Vienna, Austria: International Atomic Energy Agency, 2002.

[3] IAEA, *Implementation of accident management programmes in nuclear power plants – Safety reports series No. 32*. Vienna, Austria: International Atomic Energy Agency, 2004.

[4] B. R. Sehgal, *Nuclear safety in light water reactors – severe accident phenomenology*. Academic Press, 2012.

[5] W. Ma, Y. Yuan, and B. R. Sehgal, "In-vessel melt retention of pressurized water reactors: Historical review and future research needs," *Engineering*, vol. 2, pp. 103–111, 2016.

[6] M. Fischer, S. Bechta, V. Bezlepkin, R. Hamazaki, and A. Miassoedov, "Core melt stabilization concepts for existing and future LWRs and associated research and development needs," *Nuclear Technology*, vol. 196, no. 3, pp. 524–537, 2016. [Online]. Available: https://doi.org/10.13182/NT16-19

[7] D. Jacquemain, *Nuclear power reactor core melt accidents – Current state of knowledge*. Les Ulis, France: EDP Sciences, 2015.

[8] G. Löwenhielm, A. Engqvist, and R. Espefält, "Accident management strategy in Sweden and verification – implementation and verification," *Nuclear Engineering and Design*, vol. 148, pp. 151–159, 1994.

[9] J. Czech, J. Wirkner, M. Yvon, M. Serret, U. Krugmann, K. E. Schmidt, J. P. Berger, and M. Grenet, "European pressurized water reactor: Safety objectives and principles," *Nuclear Engineering and Design*, vol. 187, no. 1, pp. 25–33, 1999. [Online]. Available: http://dx.doi.org/10.1016/S0029-5493(98)00255-6

[10] M. Fischer, O. Herbst, and H. Schmidt, "Demonstration of the heat removing capabilities of the EPR core catcher," *Nuclear Engineering and Design*, vol. 235, no. 10-12, pp. 1189–1200, 2005.

[11] V. G. Asmolov, I. N. Gusev, V. R. Kazanskiy, V. P. Povarov, and D. B. Statsura, "New generation first-of-the kind unit – VVER-1200 design features," *Nuclear Energy and Technology*, vol. 3, no. 4, pp. 260–269, 2017. [Online]. Available: https://doi.org/10.1016/j.nucet.2017.10.003

[12] T. L. Schulz, "Westinghouse AP1000 advanced passive plant," *Nuclear Engineering and Design*, vol. 236, no. 14-16, pp. 1547–1557, 2006. [Online]. Available: https://doi.org/10.1016/j.nucengdes.2006.03.049

[13] T. N. Dinh, W. Ma, A. Karbojian, P. Kudinov, C. T. Tran, and C. R. Hansson, "Ex-vessel corium coolability and steam explosion energetics in Nordic light water reactors," Royal Institute of Technology, NKS-160, 2008.

[14] P. Kudinov, S. Galushin, S. Yakush, W. Villanueva, V.-A. Phung, D. Grishchenko, and T. N. Dinh, "A framework for assessment of severe accident management effectiveness in Nordic BWR plants," in *12th International Probabilistic Safety Assessment and Management Conference (PSAM 12)*, Honolulu, USA, 2014, pp. 22–27.

[15] IRSN, "Technical guidelines for future pressurized water reactors," IPSN/GRS, 2000.

[16] D. Bittermann, U. Krugmann, and G. Azarian, "EPR accident scenarios and provisions," *Nuclear Engineering and Design*, vol. 207, pp. 49–57, 2001. [Online]. Available: https://doi.org/10.1016/S0029-5493(00)00425-8

[17] D. Bittermann, M. Fischer, and M. Nie, "Main features of the core melt stabilization system of the European Pressurized Water Reactor (EPR)," in *18th International Conference on Structural Mechnics in Reactor Technology (SMiRT 18)*, Beijing, China, 2005, pp. 4336–4344.

[18] O. Kymäläinen, H. Tuomisto, and T. G. Theofanous, "In-vessel retention of corium at the Loviisa plant," *Nuclear Engineering and Design*, vol. 169, no. 1-3, pp. 109–130, 1997. [Online]. Available: https://doi.org/10.1016/S0029-5493(96)01280-0

[19] T. G. Theofanous, C. Liu, S. Additon, S. Angelini, O. Kymäläinen, and T. Salmassi, "In-vessel coolability and retention of a core melt," *Nuclear Engineering and Design*, vol. 169, no. 1-3, pp. 1–48, 1997. [Online]. Available: https://doi.org/10.1016/S0029-5493(97)00009-5

[20] T. N. Dinh, J. P. Tu, T. Salmassi, and T. G. Theofanous, "Limits of coolability in the AP1000 related ULPU-2400 configuration V facility," University of California, Santa Barbara, CRSS-03/06, 2003.

[21] J. L. Rempe, D. L. Knudson, C. M. Allison, G. L. Thinnes, C. L. Atwood, and M. J. Cebull, "Potential for AP600 in-vessel retention through ex-vessel flooding," Idaho National Engineering Laboratory, INEEL/EXT-97-00779, 1997.

[22] T. G. Theofanous, C. Liu, S. Additon, S. Angelini, O. Kymäläinen, and T. Salmassi, "In-vessel coolability and retention of a core melt," DOE/ID-10460, 1996.

[23] V. G. Asmolov, "Latest findings of RASPLAV project," in *Workshop on in-vessel core debris retention and coolability*. Garching bei München, Germany: Nuclear Energy Agency of the OECD (NEA), 1999, pp. 89–110.

[24] V. G. Asmolov and D. Tsurikov, "MASCA project: major activities and results," in *CSNI Workshop, MASCA Seminar*. Aix-en-Provence, France: Nuclear Energy Agency of the OECD (NEA), 2004.

[25] Westinghouse, "Westinghouse AP1000 design control document, Revision 19," 2011.

[26] J. Scobel and T. L. Schulz, "Westinghouse AP1000 PRA maturity," in *2005 International Congress on Advances in Nuclear Power Plants (ICAPP05)*. Seoul, Korea: American Nuclear Society, 2005, pp. 3354–3365.

[27] H. Esmaili and M. Khatib-Rahbar, "Analysis of in-vessel retention and ex-vessel fuel coolant interaction for AP1000," U. S. Nuclear Regulatory Commission, NUREG/CR-6849, ERI/NRC 046201, 2004.

[28] X. Cheng, Y. H. Yang, Y. Ouyang, and H. X. Miao, "Role of passive safety systems in Chinese nuclear power development," *Science and Technology of Nuclear Installations*, vol. 2009, no. 573026, pp. 1–7, 2009. [Online]. Available: http://dx.doi.org/10.1155/2009/573026

[29] Y. B. Li, L. L. Tong, X. W. Cao, and D. Q. Guo, "In-vessel retention coolability evaluation for Chinese improved 1000 MWe PWR," *Annals of Nuclear Energy*, vol. 76, pp. 343–349, 2015. [Online]. Available: https://doi.org/10.1016/j.anucene.2014.09.035

[30] V. G. Asmolov, N. N. Ponomarev-Stepnoy, V. Strizhov, and B. R. Sehgal, "Challenges left in the area of in-vessel melt retention," *Nuclear Engineering and Design*, vol. 209, no. 1-3, pp. 87–96, 2001. [Online]. Available: https://doi.org/10.1016/S0029-5493(01)00391-0

[31] L. L. Humphries, T. Chu, J. Bentz, R. Simpson, C. Hanks, W. Lu, B. Antoun, C. Robino, J. Puskar, and P. Mongabure, "OECD lower head failure project final report," Sandia National Laboratories, NM 87185-1139, 2002.

[32] W. Klein-Heßling, M. Sonnenkalb, D. Jacquemain, B. Clément, E. Raimond, H. Dimmelmeier, G. Azarian, G. Ducros, C. Journeau, L. E. H. Puebla, A. Schumm, A. Miassoedov, I. Kljenak, G. Pascal, S. Bechta, S. Güntay, M. K. Koch, I. Ivanov, A. Auvinen, and I. Lindholm, "Conclusions on severe accident research priorities," *Annals of Nuclear Energy*, vol. 74, pp. 4–11, 2014. [Online]. Available: https://doi.org/10.1016/j.anucene.2014.07.015

[33] O. Kymäläinen, H. Tuomisto, O. Hongisto, and T. G. Theofanous, "Heat flux distribution from a volumetrically heated pool with high Rayleigh number," *Nuclear Engineering and Design*, vol. 149, no. 1-3, pp. 401–408, 1994. [Online]. Available: https://doi.org/10.1016/0029-5493(94)90305-0

[34] U. Steinberner and H. H. Reineke, "Turbulent buoyancy convection heat transfer with internal heat sources," in *6th International Heat Transfer Conference*, Tronto, Canada, 1978.

[35] M. Helle, O. Kymäläinen, and H. Tuomisto, "Experimental data on heat flux distribution from a volumetrically heated pool with frozen boundaries," in *Workshop on in-vessel core*

debris retention and coolability. Garching bei München, Germany: Nuclear Energy Agency of the OECD (NEA), 1998, pp. 173–183.

[36] S. Globe and D. Dropkin, "Natural-convection heat transfer in liquid confined by two horizontal plates and heated from below," *Journal of Heat Transfer*, vol. 81, pp. 22–28, 1959.

[37] S. W. Churchill and H. H. Chu, "Correlating equations for laminar and turbulent free convection from a vertical plate," *International Journal of Heat and Mass Transfer*, vol. 18, no. 11, pp. 1323–1329, 1975. [Online]. Available: https://doi.org/10.1016/0017-9310(75)90243-4

[38] L. Bernaz, J. M. Bonnet, B. Spindler, and C. Villermaux, "Thermalhydraulic phenomena in corium pools: numerical simulation with TOlBIAC and experimental validation with BALI," in *Workshop on in-vessel core debris retention and coolability*. Garching bei München, Germany: Nuclear Energy Agency of the OECD (NEA), 1998, pp. 185–193.

[39] B. R. Sehgal, V. A. Bui, T. N. Dinh, J. A. Green, and G. Kolb, "SIMECO experiments on in-vessel melt pool formation and heat transfer with and without a metallic layer," in *Workshop on in-vessel core debris retention and coolability*. Garching bei München, Germany: Nuclear Energy Agency of the OECD (NEA), 1999, pp. 205–214.

[40] Y. Zhang, L. Zhang, Y. Zhou, W. Tian, S. Qiu, G. Su, B. Zhao, Y. Yuan, and R. Ma, "The COPRA experiments on the in-vessel melt pool behavior in the RPV lower head," *Annals of Nuclear Energy*, vol. 89, pp. 19–27, 2016. [Online]. Available: https://doi.org/10.1016/j.anucene.2015.11.013

[41] T. G. Theofanous, M. Maguire, S. Angelini, and T. Salmassi, "The first results from the ACOPO experiment," *Nuclear Engineering and Design*, vol. 169, pp. 49–57, 1997. [Online]. Available: https://doi.org/10.1016/S0029-5493(97)00023-X

[42] T. G. Theofanous and C. Liu, "Natural convection experiments in a hemisphere with Rayleigh numbers up to 10^{15}," in *National Heat Transfer Conference*. Portland, United States: American Nuclear Society, 1995, pp. 349–365.

[43] F. J. Asfia and V. K. Dhir, "An experimental study of natural convection in a volumetrically heated spherical pool bounded on top with a rigid wall," *Nuclear Engineering and Design*, vol. 163, no. 3, pp. 333–348, 1996. [Online]. Available: https://doi.org/10.1016/0029-5493(96)01215-0

[44] X. Gaus-Liu, A. Miassoedov, T. Cron, and T. Wenz, "In-vessel melt pool coolibility test – Description and results of LIVE experiments," *Nuclear Engineering and Design*, vol. 240, no. 11, pp. 3898–3903, 2010. [Online]. Available: https://doi.org/10.1016/j.nucengdes.2010.09.001

[45] B. Fluhrer, A. Miassoedov, T. Cron, J. Foit, X. Gaus-Liu, S. Schmidt-Stiefel, T. Wenz, I. Ivanov, and D. Popov, "The LIVE-L1 and LIVE-L3 experiments on melt behaviour in RPV lower head," Forschungszentrum Karlsruhe, FZKA-7419, 2008.

[46] L. Zhang, Y. Zhou, Y. Zhang, W. Tian, S. Qiu, and G. Su, "Natural convection heat transfer in corium pools: A review work of experimental studies," *Progress in Nuclear Energy*, vol. 79, pp. 167–181, 2015. [Online]. Available: https://doi.org/10.1016/j.pnuc ene.2014.11.021

[47] F. Kretzschmar and B. Fluhrer, "Behavior of the melt pool in the lower plenum of the reactor pressure vessel -Review of experimental programs and background of the LIVE program," Forschungszentrum Karlsruhe, FZKA-7382, 2008.

[48] A. Palagin, A. Miassoedov, X. Gaus-Liu, M. Buck, C. T. Tran, P. Kudinov, L. Carenini, C. Koellein, W. Luther, and V. Chudanov, "Analysis and interpretation of the LIVE-L6 experiment," in *5th European Review Meeting on Severe Accident Research (ERMSAR-2012)*, Cologne, Germany, 2012.

[49] A. Miassoedov, X. Gaus-Liu, T. Cron, and B. Fluhrer, "LIVE experiments on melt pool heat transfer in the reactor pressure vessel lower head," in *10th International Conference on Heat Transfer, Fluid Mechanics and Thermodynamics (HEFAT 2014)*, Orlando, United States, 2014, pp. 2078–2086.

[50] B. R. Sehgal, A. Karbojian, A. Giri, O. Kymäläinen, J. M. Bonnet, K. Ikkonen, R. Sairanen, S. Bhandari, M. Buerger, J. Dienstbier, Z. Techy, and T. G. Theofanous, "Assessment of reactor vessel integrity (ARVI)," *Nuclear Engineering and Design*, vol. 235, no. 2-4, pp. 213–232, 2005. [Online]. Available: https://doi.org/10.1016/j.nucengdes.2004.08.055

[51] B. R. Sehgal, A. Giri, U. Chikkanagoudar, and A. Karbojian, "Experiments on in-vessel melt coolability in the EC-FOREVER program," *Nuclear Engineering and Design*, vol. 236, no. 19-21, pp. 2199–2210, 2006. [Online]. Available: https://doi.org/10.1016/j.nucengdes.2006.03.056

[52] A. Theerthan, B. R. Sehgal, and A. Karbojian, "FOREVER experiments on thermal and mechanical behavior of a reactor pressure vessel during a severe accident – Technical report: EC-FOREVER-2 test," Royal Institute of Technology, SAM-ARVI-D 008, 1998.

[53] B. R. Sehgal, A. Giri, and A. Karbojian, "EC-FOREVER experiments on thermal and mechanical behavior of a reactor pressure vessel during a severe accident – Technical report: EC-FOREVER-4 test," Royal Institute of Technology, SAM-ARVI-D 021, 2002.

[54] H.-G. Willschütz, "Thermomechanische Modellierung eines Reaktordruckbehälters in der Spätphase eines Kernschmelzunfalls," Ph.D. dissertation, Technischen Universität Dresden, 2005.

[55] T. Chu, M. Pilch, J. Bentz, J. Ludwigsen, and W. Lu, "Lower head failure experiments and analyses," Sandia National Laboratories, NUREG/CR-5582, SAND98-2047, 1999.

[56] E. Altstadt, H.-G. Willschütz, B. R. Sehgal, and F. P. Weiss, "SARNET – Corium – WP10-2 Technical report 'Modelling of in-vessel retention after relocation of corium into the lower plenum'," Forschungszentrum Rossendorf, FZR-437, 2005.

[57] R. O. Gauntt, R. K. Cole, C. M. Erickson, R. G. Gido, R. D. Gasser, S. B. Rodriguez, and M. F. Young, "MELCOR computer code manuals: Reference manuals version 1.8.5," Sandia National Laboratories, NUREG/CR-6119, Vol.2, Rev. 2, 2005.

[58] EPRI, "Modular Accident Analysis Program 5 (MAAP5) applications guidance: Desktop reference for using MAAP5 software – Phase 3 report," Electric Power Research Institute, 3002010658, 2017.

[59] C. M. Allison and J. K. Hohorst, "Role of RELAP/SCDAPSIM in nuclear safety," *Science and Technology of Nuclear Installations*, vol. 2010, no. 425658, pp. 1–17, 2010. [Online]. Available: http://dx.doi.org/10.1155/2010/425658%0A

[60] V. A. Bui and T. N. Dinh, "Modeling of heat transfer in heat-generating liquid pools by an effective diffusivity-convectivity approach," in *2nd European Thermal-Sciences and 14th UIT National Heat Transfer Conference*, Rome, 1996.

[61] F. B. Cheung, S. W. Shiah, D. H. Cho, and M. J. Tan, "Modeling of heat transfer in a horizontal heat-generating layer by an effective diffusivity approach," in *National Heat Transfer Conference*, San Diego, United States, 1992.

[62] M. J. Tan, D. H. Cho, and F. B. Cheung, "Thermal analysis of heat-generating pools bounded from below by curved surfaces," *Journal of Heat Transfer*, vol. 116, no. 1, p. 127, 1994. [Online]. Available: https://doi.org/10.1115/1.2910846

[63] F. A. Kulacki and M. E. Nagle, "Natural convection in a horizontal fluid layer with volumetric energy sources," *Journal of Heat Transfer*, vol. 97, no. 2, p. 204, 1975. [Online]. Available: https://doi.org/10.1115/1.3450342

[64] E. R. G. Eckert and T. W. Jackson, "Analysis of turbulent free-convection boundary layer on flat plate," National Advisory Committee for Aeronautics, NACA-TR-1015, 1950.

[65] H.-G. Willschütz, E. Altstadt, B. R. Sehgal, and F. P. Weiss, "Recursively coupled thermal and mechanical FEM-analysis of lower plenum creep failure experiments," *Annals of Nuclear Energy*, vol. 33, no. 2, pp. 126–148, 2006. [Online]. Available: https://doi.org/10.1016/j.anucene.2005.08.006

[66] H.-G. Willschütz, E. Altstadt, B. R. Sehgal, and F. P. Weiss, "Simulation of creep tests with French or German RPV-steel and investigation of a RPV-support against failure," *Annals of Nuclear Energy*, vol. 30, no. 10, pp. 1033–1063, 2003. [Online]. Available: https://doi.org/10.1016/S0306-4549(03)00036-7

[67] P. Tusheva, E. Altstadt, H.-G. Willschütz, E. Fridman, and F. P. Weiss, "Investigations on in-vessel melt retention by external cooling for a generic VVER-1000 reactor," *Annals of Nuclear Energy*, vol. 75, pp. 249–260, 2015. [Online]. Available: https://doi.org/10.1016/j.anucene.2014.07.044

[68] C. T. Tran and T. N. Dinh, "The effective convectivity model for simulation of melt pool heat transfer in a light water reactor pressure vessel lower head. Part I: Physical processes, modeling and model implementation," *Progress in Nuclear Energy*, vol. 51, no. 8, pp. 849–859, 2009. [Online]. Available: https://doi.org/10.1016/j.pnucene.2009.06.007

[69] C. T. Tran and T. N. Dinh, "The effective convectivity model for simulation of melt pool heat transfer in a light water reactor pressure vessel lower head. Part II: Model assessment and application," *Progress in Nuclear Energy*, vol. 51, no. 8, pp. 860–871, 2009. [Online]. Available: https://doi.org/10.1016/j.pnucene.2009.06.001

[70] T. Chawla and S. Chan, "Heat transfer From vertical/inclined boundaries of heat-generating boiling pools," *Journal of Heat Transfer*, vol. 104, no. 3, pp. 465–473, 1982. [Online]. Available: https://doi.org/10.1115/1.3245116

[71] C. T. Tran and P. Kudinov, "The effective convectivity model for simulation of molten metal layer heat transfer in a boiling water reactor lower head," *Science and Technology of Nuclear Installations*, vol. 2013, no. 231501, pp. 1–14, 2013. [Online]. Available: http://dx.doi.org/10.1155/2013/231501

[72] W. Villanueva, C. T. Tran, and P. Kudinov, "Coupled thermo-mechanical creep analysis for boiling water reactor pressure vessel lower head," *Nuclear Engineering and Design*, vol. 249, pp. 146–153, 2012. [Online]. Available: http://dx.doi.org/10.1016/j.nucengdes.2011.07.048

[73] P. Dietrich, "Expansion of the severe accident code MELCOR by coupling external models," Ph.D. dissertation, Karlsruhe Institute of Technology, 2017.

[74] The SCDAP/RELAP5 Development Team, "SCDAP/RELAP5/MOD3.2 code manual," Idaho National Engineering and Environmental Laboratory, NUREG/CR-6150, INEL-96/0422, Revision 1 NUREG/CR-6150, INEL-96/0422, Revision 1, 1997.

[75] The RELAP5 Development Team, "RELAP5/MOD3.3 code manual," Idaho National Engineering and Environmental Laboratory, NUREG/CR-5535/Rev 1 NUREG/CR-5535/Rev 1, 2001.

[76] S. D. Lee, J. K. Lee, and K. Y. Suh, "Natural convection thermo fluid dynamics in a volumetrically heated rectangular pool," *Nuclear Engineering and Design*, vol. 237, no. 5, pp. 473–483, 2007. [Online]. Available: https://doi.org/10.1016/j.nucengdes.2006.07.012

[77] F. Mayinger, "Untersuchung thermohydraulischer Vorgänge sowie Wärmeaustausch in der Kernschmeltze," Technische Universität Hannover, BMFT-RS48/1, 1975.

[78] F. R. Larson and J. Millar, "A time temperature relationship for rupture and creep stress," *Transactions of the ASME*, vol. 74, pp. 765–775, 1952.

[79] S. S. Manson and A. M. Haferd, "A linear time temperature relation for extrapolation of creep and stress rupture data," Lewis Flight Propulsion Laboratory, NACA-TN-2890, 1953.

[80] J. F. Mao, J. W. Zhu, S. Y. Bao, L. J. Luo, and Z. L. Gao, "Creep deformation and damage behavior of reactor pressure vessel under core meltdown scenario," *International Journal of Pressure Vessels and Piping*, vol. 139-140, pp. 107–116, 2016. [Online]. Available: https://doi.org/10.1016/j.ijpvp.2016.03.009

[81] E. Altstadt and T. Mössner, "Extension of the ANSYS creep and damage simulation capabilities," Forschungszentrum Rossendorf, FZR-296, 2000.

[82] J. Lemaitre, *A course on damage mechanics*, 2nd ed. Springer, Berlin, Heidelberg, 1996.

[83] E. Gabriel, G. E. Fagg, G. Bosilca, T. Angskun, J. J. Dongarra, J. M. Squyres, V. Sahay, P. Kambadur, B. Barrett, A. Lumsdaine, R. H. Castain, D. J. Daniel, R. L. Graham, and T. S. Woodall, "Open MPI: Goals, concept, and design of a next generation MPI implementation," in *11th European PVM/MPI Users' Group Meeting (EuroPVM/MPI 2004)*, Budapest, Hungary, 2004, pp. 97–104. [Online]. Available: https://doi.org/10.1007/978-3-540-30218-6_19

[84] M. Buck, M. Bürger, A. Miassoedov, X. Gaus-Liu, A. Palagin, L. Godin-Jacqmin, C. T. Tran, W. Ma, and V. Chudanov, "The LIVE program – Results of test L1 and joint analyses on transient molten pool thermal hydraulics," *Progress in Nuclear Energy*, vol. 52, no. 1, pp. 46–60, 2010. [Online]. Available: https://doi.org/10.1016/j.pnucene.2009.09.007

[85] C. T. Tran, "The effective convectivity model for simulation and analysis of melt pool heat transfer in a light water reactor pressure vessel lower head," Ph.D. dissertation, Royal Institute of Technology, 2009.

[86] G. Bandini, B. Chatterjee, H. G. Lele, H. Austregesilo, S. Weber, A. Kapustin, K. Dolganov, D. Tomashchik, R. Gencheva, P. Groudev, A. Stefanova, P. Drai, P. Matejovic, M. Barnak, H. Muscher, H. Madokoro, M. Hoffmann, J. Bulle, and L. Sallus, "Ability of current advanced codes to predict in-vessel core melt progression and degraded core coolability – Benchmark exercise on Three Mile Island-2 Plant – Final Report," Nuclear Energy Agency of the OECD (NEA), NEA/CSNI/R(2015)3, 2015.

[87] J. K. Hohorst, S. T. Polkinghorne, L. J. Siefken, C. M. Allison, and C. A. Dobbe, "TMI-2 analysis using SCDAP/RELAP5/MOD3.1," Idaho National Engineering Laboratory, INEL-94/0157, 1994.

[88] G. Janssens-Maenhout, M. Daubner, and J. U. Knebel, "Mixed convection in a two-phase flow cooling loop," Forschungszentrum Karlsruhe, FZKA-6672, 2002.

[89] A. Azka, "Evaluation and validation of RELAP5 for RPV external cooling," Master thesis, Karlsruhe Institute of Technology, 2018.